FAR INFRARED REFLECTION SPECTROSCOPY OF LAYERED SEMICONDUCTORS

BY

AHMED RAMADAN EL-GOHARY

A Thesis submitted for the degree of Doctor of Philosphy in the Faculty of Science, Royal Holloway and Bedford New College University of London

September 1989

TO

MY PARENTS,

MY WIFE,

HAITHAM and HADDY

ABSTRACT

The optical properties of a selection of layered semiconductor samples have been studied in the far-infrared by reflection dispersive Fourier transform spectroscopy (DFTS) and attenuated total reflection (ATR) spectroscopy.

In DFTS the reference mirror in a two-beam Michelson interferometer is replaced with the sample to obtain a dispersive interferogram. This technique allows both the amplitude and phase to be measured directly. The amplitude and phase reflectivities of a variety of epitaxial layers (including a GaAs/AlAs superlattice)on GaAs substrates are presented. The measurements on the epitaxial layers are in good agreement with theoretical results obtained using standard multilayer optical calculations.

ATR spectroscopy, which permits the study of non-radiative transitions, has been used for the first time to study surface phonon-polaritons on a $GaAs/Al_xGa_{1-x}As$ multiple quantum well (MQW) structure, as well as a CdTe epitaxial layer deposited on a GaAs substrate. Both P- and S-polarised measurements have been made with a far infrared FT spectrometer fitted with an ATR stage at the output port.

In the MQW sample, the experimental results are compared with theoretical calculations derived by treating

the MQW structure as an effective uniaxial dielectric medium. The measured and theoretical results are in excellent agreement both qualitatively and quantitatively. Surface phonon-polaritons are observed in P-polarisation but only bulk modes are seen in S-polarisation as predicted by theoretical calculation.

For the CdTe epitaxial sample, surface phonon-polaritons are observed by ATR in P-polarisation in the CdTe reststrahl region. In S-polarisation, a sharp guided wave is observed in the GaAs reststrahl region. The results for both polarisations are in good agreement with calculations.

ACKNOWLEDGEMENTS

I am especially indebted to Dr T J Parker for suggesting the point of research and his valuable guidance and continuous assistance in all aspects and without him this work could not have been performed. Thank you very much Terry.

I wish to express my sincere gratitude to Dr D R Tilley for his valuable help.

I would like to thank my fellow co-workers in the solid state laboratory, namely Drs G A Gledhill, K A Maslin, T Dumelow and J D Collins.

I am very grateful for the technical help I have received during my work, especially Mr M E Thyer for the vacuum system.

Thanks must be given to Dr P J Dobson and the Philips Research Laboratories group for the loan of the samples.

I would like to acknowledge the financial support from the Government of Egypt

Finally, I would like to express my deep appreciation to my wife for the great support she has given. Without her inspiration, encouragement and sacrifice this work was not possible. Thank you Madiha.

September 1989 A R El Gohary

CONTENTS

LIST OF FIGURES

CHAPTER (1)

INTRODUCTION

CHAPTER (1)

INTRODUCTION

The techniques of molecular-beam epitaxy (MBE) and metallo organic chemical vapour-phase deposition (MOCVD) were developed during the 1970's to produce layered semiconductor samples. However, little work has been done on lattice-vibrational properties of layered semiconductors compared to the electronic properties.

Optical propagation in a layered medium was first discussed by Rytov (1956), and detailed discussions have been given by Yeh et al (1977) and Yariv and Yeh (1977).

It is well known that the interaction of electromagnetic radiation with optical phonons leads to a spectral region of high reflectivity known as the reststrahlen band in the far infrared. This type of coupled excitation is known as a bulk phonon-polariton. A surface polariton is a coupled mode of the electromagnetic field and a dipole-active excitation, propagating along an interface between the dipole-active medium and another medium (for example air or vacuum). Detailed accounts are given by Otto (1974), Agranovich and Mills (1982), and Cottam and Tilley (1989). When the excitation involved is a transverse optical (TO) phonon, the mode is called a surface phonon-polariton.

For wavelengths much greater than the periodicity of

the layered structures, the bulk-slab model usually leads to a good description of experiments in the reststrahl frequency region. In this model, the dielectric response of each layer is described by a bulk-type dielectric function. This fact was established by Raj and Tilley (1985), Liu et al (1985) and Agranovich and Kravstov (1985)

In the 1980's, with the fine control available in MBE, it is possible to prepare samples in which each layer is only a few monolayers thick with any desired sequence of components. For these samples, the bulk slab model is inadequate. Many theoretical studies have been performed to yield explicit expressions for the dielectric function of these samples, for example Ren et al (1984). This problem appears not yet to be fully resolved.

In this work far infrared measurements by dispersive Fourier transform spectroscopy (DFTS) and attenuated total reflection (ATR) spectroscopy have been made on a variety of layered semiconductor samples.

DFTS was used to study the bulk modes, by reflecting far infrared radiation at normal incidence near the centre of the sample. The ATR technique was used to study surface phonon-polaritons in the reststrahlen regions by placing the sample near the base of a prism in which radiation is undergoing internal reflection at oblique incidence. The two techniques have enabled all infrared-active bulk and surface phonon modes and guided waves propagating in multi-layer

semiconductor specimens to be investigated.

Fourier transform spectroscopy (FTS) may be defined as a technique whereby a spectrum is determined by the explicit application of Fourier transformation to the output of a two-beam interferometer. In chapter (2) a review of FTS is given, including a detailed discussion of non-dispersive (power) and dispersive techniques. Also, the concept of the complex insertion loss developed by Chamberlain (1972) to relate the complex Fourier transform to the amplitude and phase is discussed.

The instrument used to study the bulk modes, as described in chapter (3), was based on the cube interferometer by Grubb Parsons Ltd, which divides the radiation into two partial beams at 90° to each other. The specimen is placed in the position of the fixed mirror of the interferometer so that it interacts with only one of the partial beams. For the reference measurements the specimen is replaced by the fixed mirror.

The term polariton does not appear in the literature before 1958 and seems to be due to Hopfield et al who also gave the first experimental evidence for phonon polaritons in cubic GaP (1963). Chapter (4) is concerned with polariton modes arising from frequency dispersion in the dielectric function. Also, a review of bulk and surface polariton dispersion curves of a superlattice has been given.

The amplitude r and the phase ϕ of the DFTS reflection spectra of two epi-layer semiconductors and one short period superlattice on doped substrates are discussed in chapter (5). These spectra are compared with theoretical spectra obtained by using a standard multilayer optics technique. The overall agreement between measurements and calculated data is good in all cases. However, the theoretical model to calculate the spectra for the short period superlattice is still being developed.

Recently, the ATR method has become the principal technique to study surface polariton dispersion curves. A detailed discussion of the ATR technique is given in chapter (6).

In this work the surface phonon polariton measurements were made using a far infrared FTS fitted with an ATR stage at the output port. The instrument used is described in chapter (7).

In chapter (8) we report for the first time the observation of surface phonon polaritons on a long period $GaAs/Al_xGa_{1-x}As$ multiple quantum well (MQW) structure. The measurements were made in both p (transverse magnetic, TM) and s (transverse electric, TE) polarisation. The experimental results are compared with theoretical spectra derived by treating the MQW structure as an effective uniaxial dielectric bulk medium. The experimental and theoretical results are in excellent agreement.

ATR measurements were also made on an epitaxial layer of CdTe on a GaAs substrate. These measurements were made in both p and s polarisation. The measurements have revealed a p polarised surface polariton in the CdTe reststrahlen band as predicted by calculations based on standard multilayer optics techniques. In each polarisation the measured results are in good agreement with calculations.

REFERENCES:

V M Agranovich and V E Kravstov, Solid State Commun. 55, 85, 1985.

V M Agranovich and D L Mills, "Surface Polaritons", (Amsterdam: North-Holland), 1982.

J E Chamberlain, Infrared Phys. 11, 145, 1972.

M G Cottam and D R Tilley, "Introduction to Surface and Superlattice Excitations", (Cambridge: Cambridge University Press), 1989.

J J Hopfield, Phys. Rev. 112, 1555, 1958.

J J Hopfield and D G Thomas, Phys. Rev., 132, 583, 1963.

W M Liu, G Eliasson and J J Quinn, Solid State Commun., 55, 533, 1985

A Otto, Festkorperprobleme (Advances in Solid State Physics) vol. XIV, ed. J Treush (Braunschweig: Vieweg) 1974.

N Raj and D R Tilley, Solid State Commun., 55, 373, 1985.

S F Ren, H Chu and Y-C Chang, Phys. Rev., B37, 8899, 1988.

S M Rytov, Zh. 2, 71 (Sov. Phys. Acoust. 2, 68), 1956.

A Yariv and P Yeh, J. Opt. Soc. Am., 67, 438, 1977.

P Yeh, A Yeriv, and C S Hong, J. Opt. Soc. Am., 67, 423, 1977.

CHAPTER 2

FOURIER TRANSFORM SPECTROMETRY

Chapter (2)

FOURIER TRANSFORM SPECTROMETRY

2.1 FOURIER TRANSFORM SPECTROSCOPY :

The method of Fourier transform spectroscopy (FTS) [see, e.g. Bell 1972, Chamberlain 1977] may be defined as the technique whereby a spectrum is determined by the application of a Fourier transformation to the output of a two beam interferometer. The output data obtained after scanning is the Fourier transform of all the spectral components known as the interferogram. Now, because of the progress made in recent times in the development of small, dedicated computers and microprocessors as integral components of laboratory equipment, the advantages of "Fourier spectroscopy" are being widely realized.

2.2 FOURIER TRANSFORM PAIR :

The arrangement used in some types of modern Fourier transform spectrometer is shown in fig(2-1). In this arrangement the light from the source is collimated by a mirror c before being amplitude-divided by the beam splitter B. With an extended source, of wavelength λ, rays can enter the system over a wide angle and concentric bright rings are seen, figure (2-2). That condition is given by

$$x \cos\theta = m\lambda$$

where m is an integer or zero and x/2 is the mirror separation. The collimation has the effect of making the whole cross-section of the illumination field through the instrument correspond to the axial (θ = 0) direction. Circular fringes are therefore absent and the whole field has uniform intensity. The changes in this intensity as a function of distance travelled by the moving mirror M_1 are measured with the mirror and the detector arrangement shown in the figure. The intensity D(x) measured by the detector as a function of the optical path difference is expressed as

(Bell 1972)

$$D(x) = \int_{-\infty}^{+\infty} B(\nu) \, [\, 1 + \cos(2\pi\nu x) \,] \, d\nu \qquad (2.1)$$

$$D(x) = \int_{-\infty}^{+\infty} B(\nu) \, d\nu + B(\nu) \cos(2\pi\nu x) \, d\nu \qquad (2.2)$$

When the two mirrors are exactly equidistant, optically, from the beam-splitter,

$$x = 0 \quad \text{and} \quad D(x) = D(0)$$

$$D(0) = 2 \int_{-\infty}^{+\infty} B(\nu) \, d\nu \qquad (2.3)$$

therefore we have

$$D(x) - 1/2\ D(0) = \int_{-\infty}^{+\infty} B(\nu)\ \cos\ (2\pi\nu x)\ d\nu \qquad (2.4)$$

We may write

$$I(x) = \int_{-\infty}^{+\infty} B(\nu)\ \cos\ (2\pi\nu x)\ d\nu \qquad (2.5)$$

which shows that the interferogram depends on the spectrum according to a cosine Fourier integral.

The spectrum, with the variable ν given in wavenumbers cm^{-1}, can be obtained by applying an inverse cosine transformation to I(x),

$$B(\nu) = \int_{-\infty}^{+\infty} I(x)\ \cos\ (2\pi\nu x)\ dx \qquad (2.6)$$

equations (2.5) and (2.6) are called a Fourier transform pair.

If the interferogram is not symmetric, a complex Fourier transform is used instead of a cosine transform (Bell 1972, Chamberlain 1979 and Chantry 1984). The complex form of the interferogram function I(x) is given as;

$$I(x) = \int_{-\infty}^{+\infty} B(\nu)\ \exp\ (\ i2\pi\nu x)\ d\nu \qquad (2.7)$$

and the spectrum is given as;

$$B(\nu) = \int_{-\infty}^{+\infty} I(x) \exp(-i2\pi\nu x)\, dx \qquad (2.8)$$

The Fourier transform pair relates the two functions I(x) and B(ν) so that if one is known, the other can be determined.

2.3 POWER FTS :

In power FTS (e.g Bell 1972, Chamberlain 1979 and Chantry 1984), the specimen is usually placed in the output beam before the detector window and after the two beams from the arms have recombined. The experimental configuration for non-dispersive Fourier transform spectrometry is shown schematically in figure (2-3). This shows both reflection and transmission modes for a standard Michelson interferometer. From these arrangements either the power reflectivity or power transmissivity can be obtained.

Internal reflection spectroscopy, also known as attenuated total reflection (ATR) spectroscopy is a non-dispersive method to study the surface properties of suitable specimens. This technique will be discussed in detail in chapter (6).

2.4 DISPERSIVE FOURIER TRANSFORM SPECTROSCOPY (DFTS) :

Dispersive Fourier spectrometry (DFTS) is a powerful technique for measurements of both optical constants of suitable materials from direct measurements of their amplitude and phase response functions, either in reflection or transmission. The method has been reviewed by Birch and Parker (1979). In DFTS the sample is placed in one arm of the interferometer, fig (2-4). One partial beam is interacting with a dispersive medium and the other is not, so the symmetry of the interferometer is disturbed. The difference between the phase shifts of the partial beams will then show significant variations and the interferogram will be markedly asymmetric, figure (2-5), for reflection DFTS.

The experimental configurations for dispersive Fourier transform spectrometry are shown in figure (2-6). In fig (2-6.a) the specimen is placed in the fixed mirror arm of the interferometer and the radiation in that arm passes through it twice. This technique is known as a **double-pass transmission measurement**. If the specimens are highly absorbing, a **single- pass transmission** measurement is taken. The configuration for this technique is shown in figure (2-6,b). The optics of this interferometer are arranged so that the radiation in the fixed mirror arm only passes through the specimen once. If the specimen is opaque, a

reflection measurement is required, and the fixed mirror of the interferometer is replaced by the sample as shown in figure (2-6,c).

2.5 DFTS AND THE COMPLEX INSERTION LOSS :

For completeness, we now give a brief summary of some aspects of the theory of DFTS (see Birch and Parker 1979). To derive an expression relating the interferogram to the optical constants, it is useful to define the complex insertion loss. Following the approach of Chamberlain (1972), we can define the complex insertion loss;

$$\tilde{L}(\nu) = L(\nu) \exp i\Phi_L(\nu) \qquad (2.9)$$

as the complex factor which describes the changes which occur in the amplitude and phase of an electromagnetic wave propag- ating in the fixed arm of the interferometer when a reference material, such as a vacuum or perfect mirror, is replaced by the specimen.

The electric field vector of a wave propagating in the fixed arm of the interferometer in free space can be written as a Fourier integral

$$\underline{\tilde{E}} = \int_{-\infty}^{+\infty} \underline{\tilde{E}}_0(\nu) \exp [i2\pi\nu(z-ct)] \, d\nu \qquad (2.10)$$

where;

$\tilde{E}_o$ is the amplitude

z is a coordinate in the direction of propagation.

t is the time

Similarly, the electric field propagating in the moving mirror arm can be written as;

$$\tilde{E}_2 = \int_{-\infty}^{+\infty} \tilde{E}_o(\nu) \exp [i2\pi\nu(z+x-ct)] \, d\nu \qquad (2.11)$$

where x/2 is the displacement of the moving mirror from the position of zero optical path difference.

Now if we place a sample in the fixed mirror arm, the output from the fixed arm can similarly be written as;

$$\tilde{E}_1 = \int_{-\infty}^{+\infty} \tilde{E}_o(\nu) L(\nu) \exp i[2\pi\nu(z-ct)+\Phi_1(\nu)+\Phi_o(\nu)] \, d\nu \qquad (2.12)$$

where $\Phi_o(\nu)$ is a small residual phase difference denoting lack of perfect symmetry in the interferometer due to imperfect alignment, or some other asymmetry between the optical paths. The resultant electric field amplitude in the recombined beam propagating toward the output port is;

$$\tilde{E}_r = \tilde{E}_1 + \tilde{E}_2$$

$$= \int_{-\infty}^{+\infty} \tilde{g}(\nu,x) \exp [i2\pi\nu(z-ct)] \, d\nu \qquad (2.13)$$

where

$$\tilde{g}(\nu,x) = \tilde{E}_o(\nu)\ [L(\nu)\ \exp\ i\Phi(\nu) + \exp\ (i2\pi\nu x)] \quad (2.14)$$

and

$$\Phi(\nu) = \Phi_1(\nu) + \Phi_o(\nu) \quad (2.15)$$

The output intensity

$$I_s(x) = \tilde{E}_r\ \tilde{E}_r^*$$

reaching the detector is proportional to $g(\nu,x)$ $g^*(\nu,x)$,where * indicates the complex conjugate. Therefore, the output intensity $I_s(x)$ can be expressed as

$$I_s(x) = \int_{-\infty}^{+\infty} \tilde{g}(\nu,x)\ \tilde{g}^*(\nu,x)\ d\nu \quad (2.16)$$

$$= \int_{-\infty}^{+\infty} \tilde{E}_o(\nu)\ \tilde{E}_o^*(\nu)\ [\ 1 + L^2(\nu)\ ]d\nu$$

$$+2\int_{-\infty}^{+\infty} \tilde{E}_o(\nu)\ \tilde{E}_o^*(\nu)\ L(\nu)\ \cos[\Phi(\nu)-2\pi\nu x]d\nu \quad (2.17)$$

Since the first term is independent of x, it is of no further interest. The second term is the interference function which is usually recorded as the interferogram. This function can be written as a sum of even and odd

components:

$$\underline{I}_S(x) = \int_{-\infty}^{+\infty} \rho(\nu) \cos \Phi(\nu) \cos (2\pi\nu x)\, d\nu$$

$$+ \int_{-\infty}^{+\infty} \rho(\nu) \sin \Phi(\nu) \sin (2\pi\nu x)\, d\nu \qquad (2.18)$$

where

$$\rho(\nu) = 2\, \underline{\tilde{E}}_O(\nu)\, \underline{\tilde{E}}_O^*(\nu)\, L(\nu) \qquad (2.19)$$

is the recorded power spectrum, while $\Phi(\nu)$ contains the phase response of the sample. Now, if we take the cosine and sine transforms of equation (10), the resulting functions are given by

$$p(\nu) = \int_{-\infty}^{+\infty} I_S(x) \cos (2\pi\nu x)\, dx$$

$$= \rho(\nu) \cos \Phi(\nu) \qquad (2.20)$$

$$q(\nu) = \int_{-\infty}^{+\infty} I_S(x) \sin (2\pi\nu x)\, dx$$

$$= \rho(\nu) \sin \Phi(\nu) \qquad (2.21)$$

The computed spectrum will be given by

$$\tilde{S}(\nu) = p(\nu) + iq(\nu)$$

$$= \rho(\nu) \exp i\Phi(\nu) \qquad (2.22)$$

with a modulus of

$$\rho(\nu) = [\, p^2(\nu) + q^2(\nu) \,]^{1/2} \qquad (2.23)$$

and a phase

$$\Phi(\nu) = \tan^{-1} [\, q(\nu)/p(\nu) \,] \qquad (2.24)$$

From equations (2.8),(2.15) and (2.18)-(2.21) it follows that the complex insertion loss is related to the complex Fourier transform of the interferogram by

$$2\, \tilde{\underline{E}}_o(\nu)\, \tilde{\underline{E}}_o^*(\nu)\, \tilde{L}(\nu) \exp [\, i\Phi_o(\nu) \,]$$

$$= \int_{-\infty}^{+\infty} I_s(x) \exp (2\pi i\nu x) \, d\nu \qquad (2.25)$$

If we remove the sample from the fixed arm of the interferometer, the interferometer returns to the symmetrical configuration and a background interferogram $I_o(x)$ may be recorded. It can easily be shown that

$$I_o(x) = \int_{-\infty}^{+\infty} \rho_o(\nu) \cos [\, \Phi_o(\nu) - 2\pi\nu x \,] \, d\nu \qquad (2.26)$$

which is similar to the interference part of equation

(2.17), with

$$\rho_o(\nu) = 2\underline{\tilde{E}}_o(\nu)\,\underline{\tilde{E}}_o^{*}(\nu) \qquad (2.27)$$

The cosine and sine transforms of equation (18) can be computed to give

$$p_o(\nu) = \int_{-\infty}^{+\infty} I_0(x)\cos 2\pi\nu x\,dx$$

$$= \rho_o(\nu)\cos\Phi_o(\nu) \qquad (2.28)$$

and

$$q_o(\nu) = \int_{-\infty}^{+\infty} I_0(x)\sin 2\pi\nu x\,dx$$

$$= \rho_o(\nu)\sin\Phi_o(\nu) \qquad (2.29)$$

Then, the computed background spectrum of the interferometer is given by

$$S_o(\nu) = p_o(\nu) + iq_o(\nu)$$

$$= \rho_o(\nu)\exp[\,i\Phi_o(\nu)\,] \qquad (2.30)$$

which is a complex quantity and has a modulus

$$\rho_o(\nu) = [\,p_o^2(\nu) + q_o^2(\nu)\,]^{1/2} \qquad (2.31)$$

and a phase of

$$\Phi_o(\nu) = \tan^{-1} [\, q_o(\nu) / p_o(\nu) \,] \qquad (2.32)$$

Hence from equations (2.27)-(22.30) it follows that

$$2\, \tilde{\underline{E}}_o(\nu)\, \tilde{\underline{E}}_o^*(\nu) \exp [\, i\Phi_o(\nu) \,]$$

$$= \int_{-\infty}^{+\infty} I_0(x) \exp (2\pi i\nu x) \, dx \qquad (2.33)$$

To obtain the complex insertion loss, we take the ratio of the two complex Fourier transforms as shown below

$$L(\nu) = \frac{\int_{-\infty}^{+\infty} I_s(x) \exp (i2\pi\nu x) \, dx}{\int_{-\infty}^{+\infty} I_o(x) \exp (i2\pi\nu x) \, dx}$$

$$= \frac{FT\ [I_s(x)]}{FT\ [I_o(x)]} \qquad (2.34)$$

The function FT in equation (34) is the Fourier transform as a mathematical operation performed in the computer. By using the equation (34), the complex insertion loss can be calculated directly if complex numbers are used.

Since the Fourier transform programs are written in Pascal, and standard Pascal does not support the complex

notation, the complex insertion loss $L(\nu)$ and the phase $\Phi_l(\nu)$ are calculated separately from the sine and cosine Fourier transforms of $I_s(x)$ and $I_o(x)$. Using equations (2.20)-(2.21) for $I_s(x)$ and equations (2.28)-(2.29) for $I_o(x)$ gives

$$L(\nu) = \frac{[\, p^2(\nu) + q^2(\nu) \,]^{1/2}}{[p_o^2(\nu) + q_o^2(\nu)]^{1/2}} \qquad (2.35)$$

and

$$\Phi_l(\nu) = \tan^{-1}\left[\frac{q(\nu)}{p(\nu)}\right] - \tan^{-1}\left[\frac{q_o(\nu)}{p_o(\nu)}\right] \qquad (2.36)$$

2.6 THE AMPLITUDE REFLECTIVITY OF AN OPAQUE SOLID:

Since all the materials studied in this thesis are opaque and highly absorbing, their optical constants could be determined by measuring their front surface complex amplitude reflection coefficients.

The method described below applied to all data to obtain the complex insertion loss. The principle of this method is that; firstly the background interferogram $I_o(x)$ is recorded using a perfect mirror. Second, we replace the fixed mirror with the sample, then the specimen interferogram $I_s(x)$ is recorded. As the phase spectra of all samples used in this work are well-determined above their reststrahlen bands on physical grounds, the specimen

phase can be set by applying a linear phase correction. This simplifies the experimental work, particularly when a small samples (≈5mm × 5μm) are used. Because the materials are highly absorbing, only the first reflected partial wave can be observed and there are no higher order terms due to transmission and subsequent reflections. The amplitude reflectivity of the fixed mirror is given by

$$\bar{r}_o(\nu) = r_o(\nu) \exp [\, i\Phi_o(\nu) \,] \qquad (2.37)$$

For a perfect mirror, the amplitude would be equal to 1.0 and the phase equal to π . The amplitude reflection coefficient of the reference mirror would therefore be given by

$$\bar{r}_o(\nu) = \exp (i\pi) \qquad (2.38)$$

The amplitude reflection coefficient of the specimen is given by

$$\bar{r}_s(\nu) = r_s(\nu) \exp [i\Phi_s(\nu)] \qquad (2.39)$$

By using equation (26), the complex insertion loss is given by

$$\bar{L}(\nu) = \frac{\bar{r}_s(\nu)}{\bar{r}_o(\nu)}$$

$$= \frac{r_s(\nu)\ \exp\ [\ i\Phi_s(\nu)\ ]}{r_o(\nu)\ \exp\ [\ i\pi\ ]}$$

$$= r_s(\nu)\ \exp\ i[\ \Phi_s(\nu) - \pi\ ] \qquad (2.40)$$

$$= \frac{FT\ [\ I_s(x)\ ]}{FT\ [\ I_o(x)\ ]}$$

So the insertion loss $L(\nu)$ and the phase $\phi_s(\nu)$ can be calculated from equations (2.35) and (2.36), apart from the linear correction mentioned above. Then by using equation (2.40) the amplitude $\tilde{r}_s(\nu)$ can be determined.

2.7 THE RESPONSE FUNCTIONS:

Consider a plane parallel specimen of complex refractive index $N_1(\nu)$ immersed in a medium of complex refractive index $N_2(\nu)$ as shown in fig(2-7). Using the Fresnel equations at normal incidence, given by Birch and Parker (1979), the amplitude reflectivity of the surface of the sample is given by

$$\tilde{r}(\nu) = \frac{\tilde{N}_1(\nu) - \tilde{N}_2(\nu)}{\tilde{N}_1(\nu) + \tilde{N}_2(\nu)} \qquad (2.41)$$

If medium (1) is a vacuum, since the instrument is evacuated while scanning, the refractive index N_1 is equal to 1.0 and equation (2.41) reduces to

$$\tilde{r}(\nu) = \frac{1 - \tilde{N}_2(\nu)}{1 + \tilde{N}_2(\nu)} \qquad (2.42)$$

Rearranging equation (2.42), the complex refractive index $\tilde{N}_2(\nu)$ is given by

$$\tilde{N}_2(\nu) = \frac{1 - \tilde{r}(\nu)}{1 + \tilde{r}(\nu)} \qquad (2.43)$$

From Maxwell's equations (Chantry 1984), the complex refractive index is given by

$$\tilde{N}(\nu) = n(\nu) + ik(\nu) \qquad (2.44)$$

where real $\tilde{N}(\nu) = n(\nu)$ **Refractive index**

Imag $\tilde{N}(\nu) = k(\nu)$ **Absorption index**

Using equation (2.44) the refractive and absorption indices can be calculated. Also the complex dielectric permittivity is related to the complex refractive index by

$$\tilde{\epsilon}(\nu) = \tilde{N}^2(\nu) = [\, n(\nu) + ik(\nu) \,]^2$$

$$= n^2(\nu) - k^2(\nu) + i2n(\nu)k(\nu) \qquad (2.45)$$

and

$$\tilde{\epsilon}(\nu) = \epsilon'(\nu) + i\epsilon''(\nu) \qquad (2.46)$$

From equations (2.45) and (2.46) the real and imaginary components of the dielectric permittivity can be expressed in terms of the refractive and absorption indices as

$$\epsilon'(\nu) = n^2(\nu) - k^2(\nu) \qquad (2.47)$$

$$\epsilon''(\nu) = 2n(\nu)k(\nu) \qquad (2.48)$$

Since the electric susceptibility χ is related to the dielectric permittivity by

$$\tilde{\epsilon}(\nu) = 1 + \tilde{\chi}(\nu) \qquad (2.49)$$

where;

$$\tilde{\chi}(\nu) = \chi'(\nu) + i\chi''(\nu) \qquad (2.50)$$

it can be determined from the above equations. From equations (2.49) and (2.50), the real and imaginary parts of the dielectric permittivity are given by

$$\epsilon' = 1 + \chi' \qquad (2.51)$$

$$\epsilon'' = \chi'' \qquad (2.52)$$

The electric susceptibility will be of use later to determine the optical characteristics of solids.

As has been shown, all of the response functions can be obtained from the Fourier transform pair using the complex insertion loss .

2.8 REFERENCES

R.J. Bell ; "Introductory Fourier Transform Spectroscopy" Academic Press, New York (1972)

J.R. Birch and T.J. Parker, Infrared and Millimeter Waves, vol. 2, 137, Edited by K.J. Button, Academic Press, New York (1979).

J.E. Chamberlain, Infrared Phys., 12, 145, 1972

J.E. Chamberlain, The Principles of Interferometric Spectroscopy, completed, collated and edited by G.W Chantry and N.W. Stone, A Wiley-Interscience Publication (1979)

G.W. Chantry, "Submillimetre Spectroscopy", Academic Press, New York (1971)

G.W. Chantry, "Long Wave Optics", Academic Press, New York (1984)

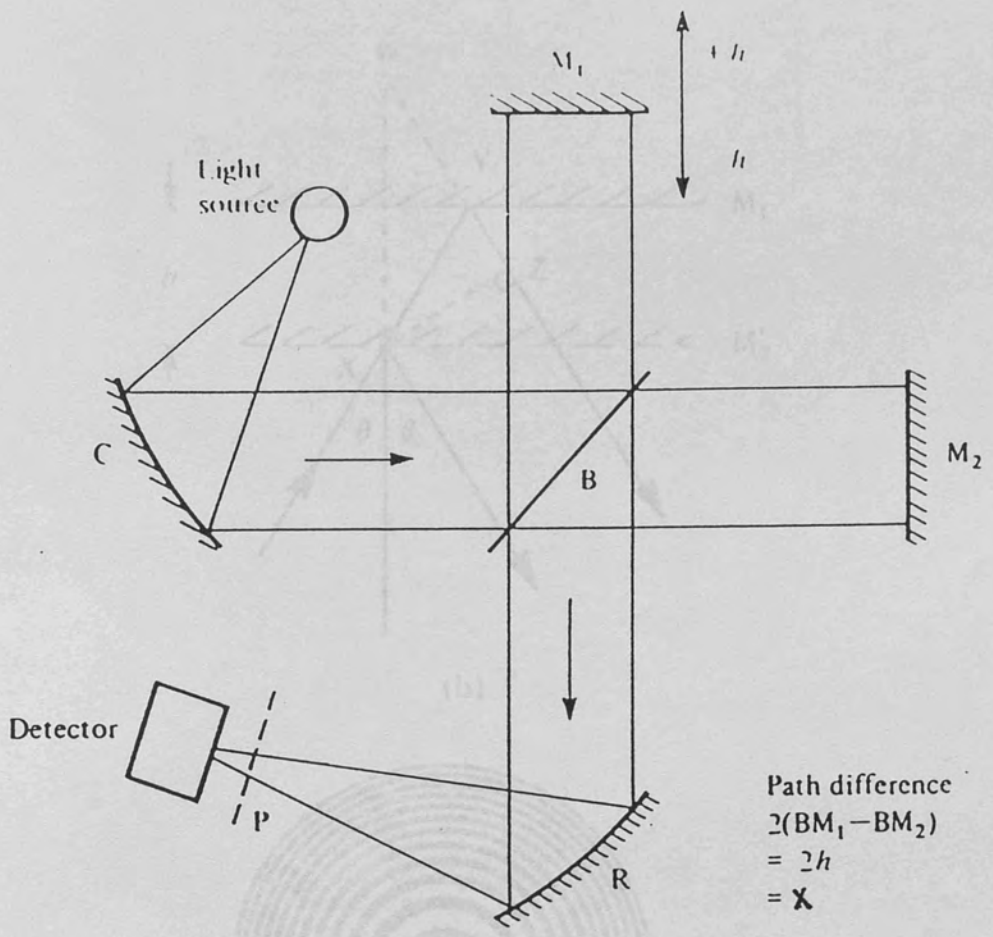

Fig (2.1) Diagram of Fourier transform spectrometry

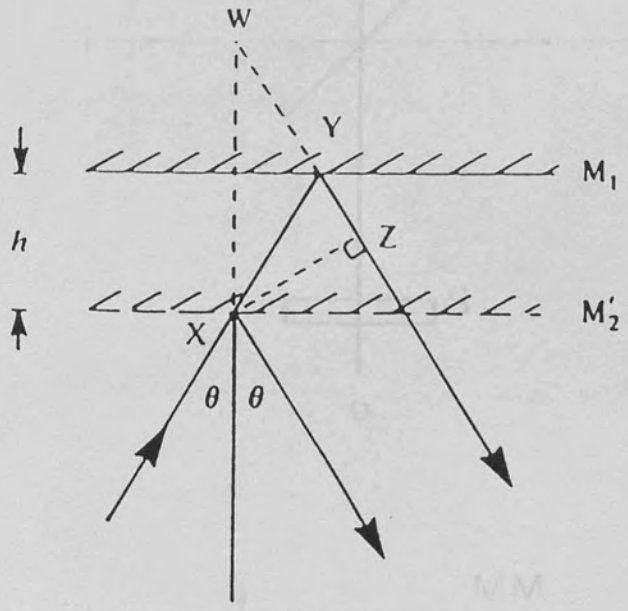

(b)

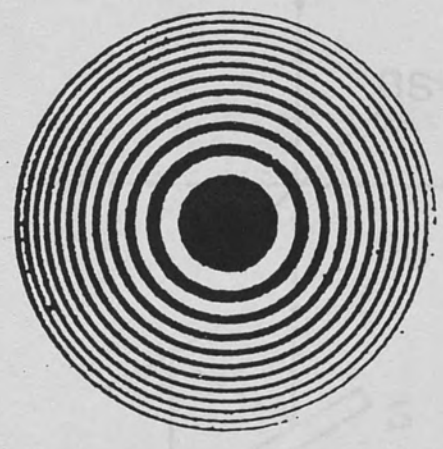

Fig (2.2) Appearance of the fringes with quasimonochromatic light

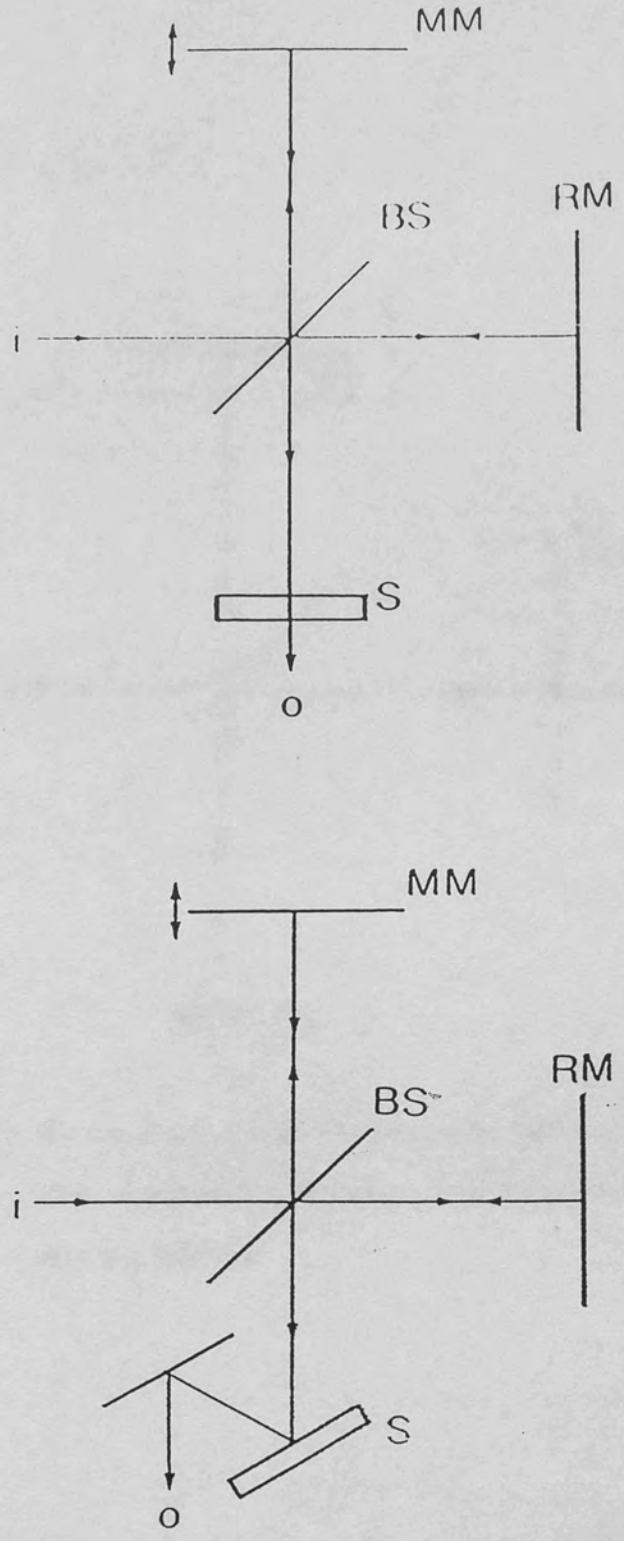

Fig (2.3) Schematic diagram of a non-dispersive Fourier transform spectrometer (a) transmission, (b) reflection

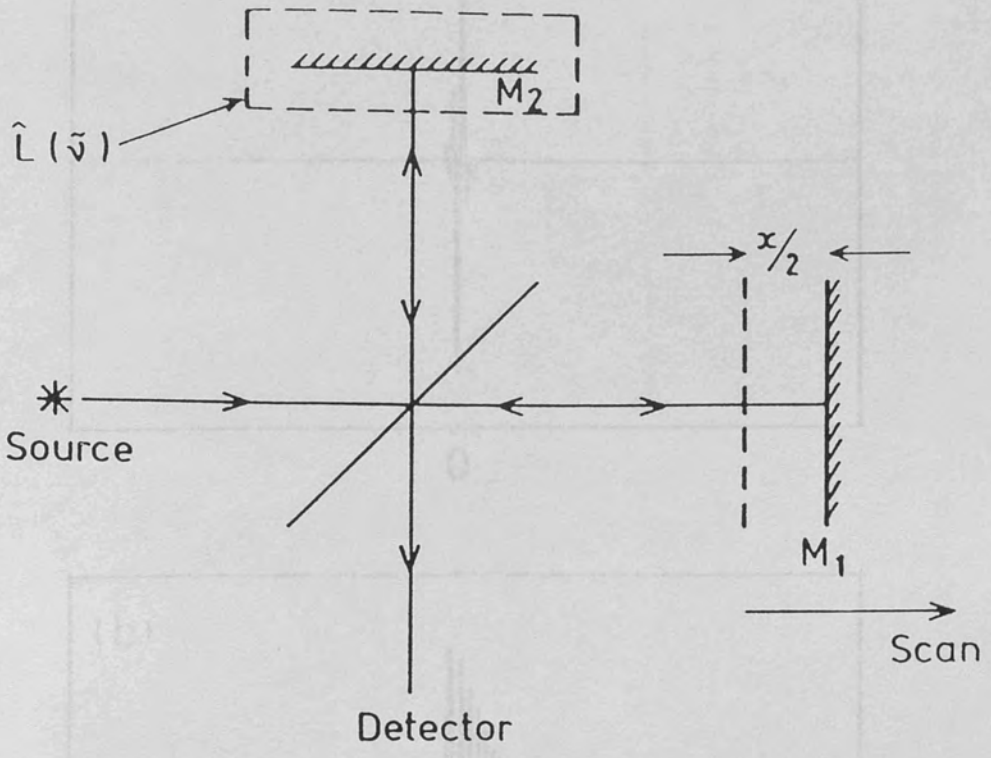

Fig (2.4) Schematic diagram showing the position of the sample in dispersive Fourier transform spectrometry

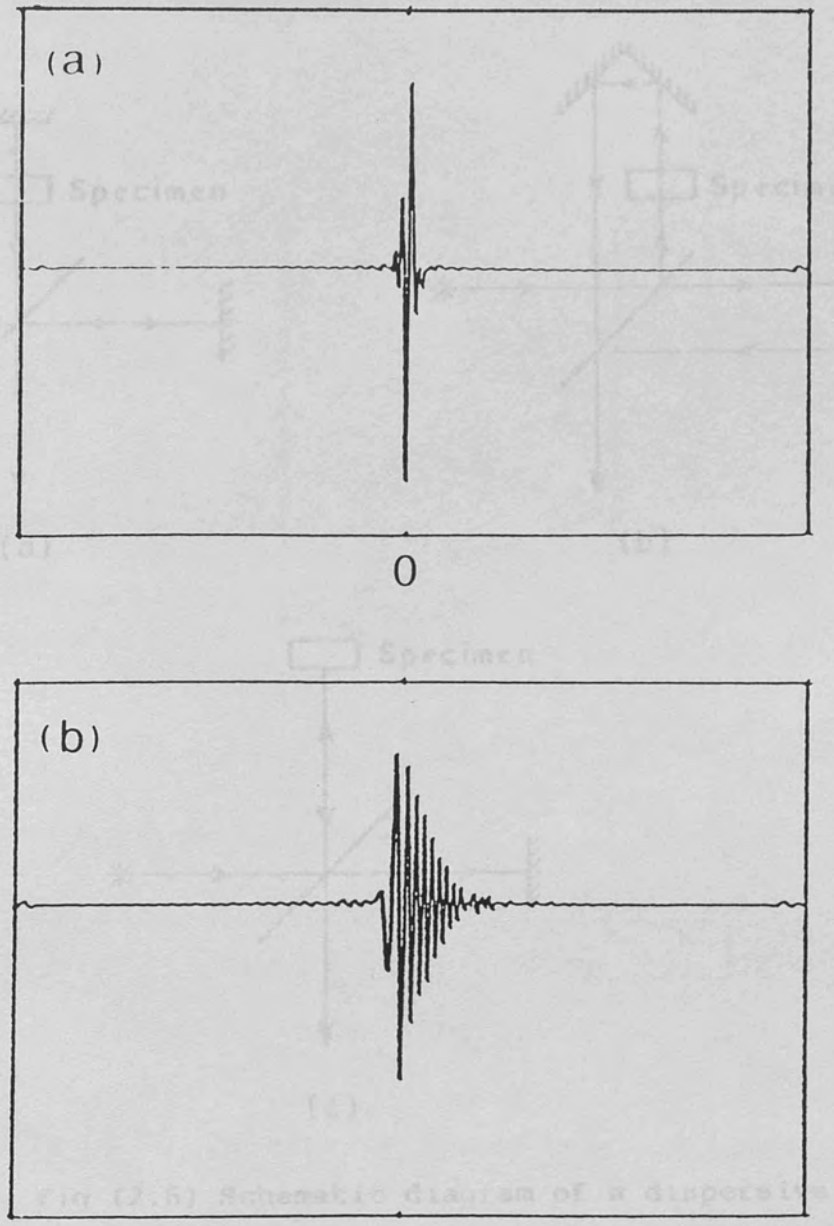

Fig (2.5) Comparison of a symmetrical background interferogram and an asymmetric sample interferogram in reflection DFTS

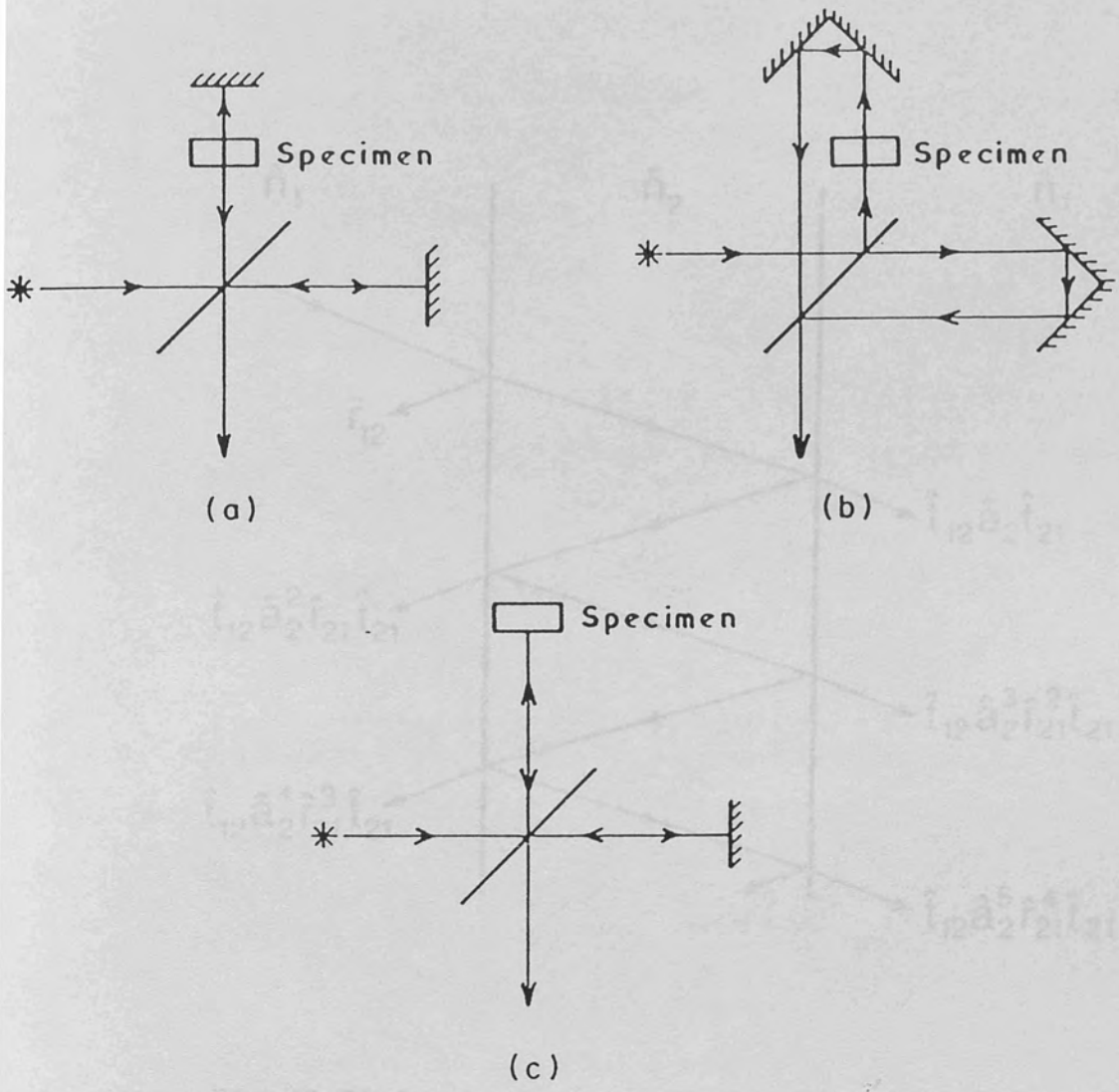

Fig (2.6) Schematic diagram of a dispersive Fourier transform spectrometer

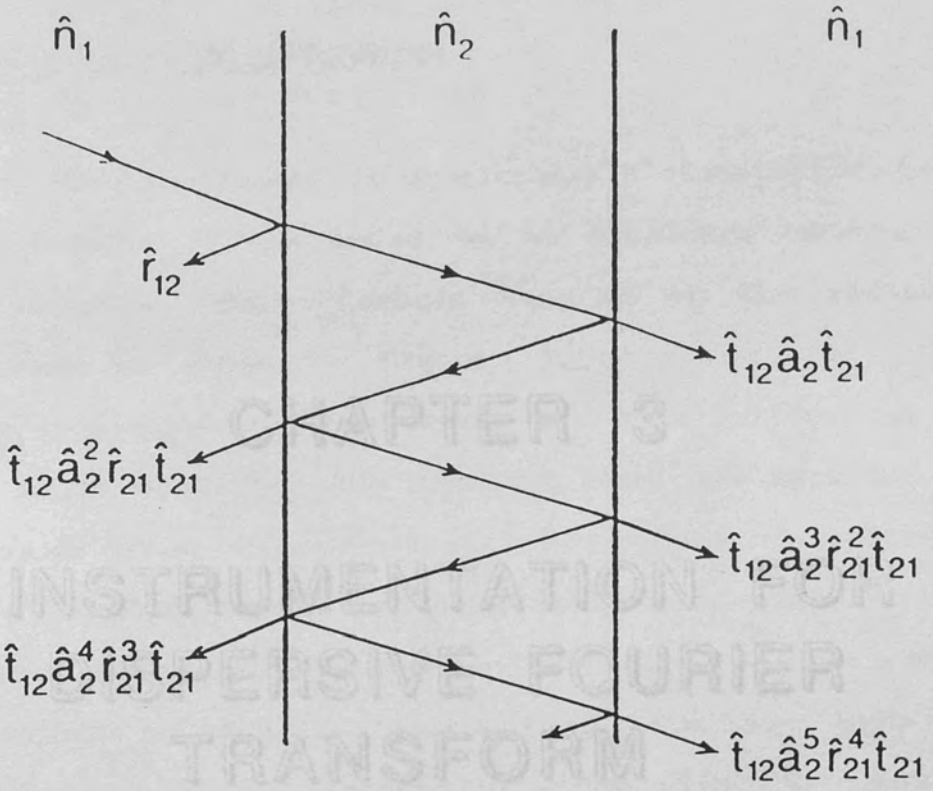

Fig (2.7) The rays reflected from and transmitted through a sample immersed in a medium

CHAPTER 3

INSTRUMENTATION FOR DISPERSIVE FOURIER TRANSFORM SPECTROSCOPY

CHAPTER (3)

INSTRUMENTATION FOR DISPERSIVE FOURIER TRANSFORM SPECTROSCOPY

3.1 THE OPTICAL INTERFEROMETER :

The instrument is essentially a classical Michelson interferometer. It is based on an NPL/Grubb Parsons cube interferometer. The schematic diagram of the reflection instrument is shown in figure (3.1). The basis of this system is the central cube where the beam splitter is kept at an angle of 45^{o} to the incoming beam. The beam splitter is made of Mylar which is used for a number of reasons. It can be supplied as large industrial rolls which are not expensive. It is transparent in both the far infrared and the visible, so that it allows the use of a laser beam which is coincident to the optical axis for alignment. Also, if the plastic is broken, a new piece can be stretched in place in a few minutes. The equation relating the thickness of the beam splitter to the interference maxima and minima, given by (Bell 1972) is

$$m\lambda = 2d \left[n^2 - 1/2 \right]^{1/2}$$

where;

d is the thickness of the Mylar

n is the refractive index

The condition for an interference maximum (constructive interference) is that;

$$m = 1/2 , 3/2 , 5/2 , \ldots\ldots\ldots$$

and for an interference minimum (destructive interference) is that ;

$$m = 0 , 1 , 2 , \ldots\ldots\ldots\ldots\ldots$$

As a numerical example for a 6.25 μm thick beam splitter, the peak efficiency (constructive interference) for m = 1/2 occurs at 250 cm^{-1} then it falls to zero at 500 cm^{-1} (m = 1). Because all of the optical Reststrahlen responses of semiconductors are in the range 100 cm^{-1} to 500 cm^{-1}, Mylar film of thickness 6.25 μm was used in this work.

3.2- THE COLLIMATOR:

The radiation source used is a fused quartz encapsulated Mercury lamp (Philips 125-HPK). The lamp is inside a copper heat shield, into which is drilled the exit aperture. The size of the aperture is normally between 5 and 10 mm. The shield is coupled to a water cooled jacket. The excess heat generated by the lamp is transfered to the water, which is connected to a water circulator and temperature stabiliser.

A parabolic mirror is used to collimate the beam leaving the aperture and reflects it through 45^{o} to a plane

mirror. The plane mirror has a small circle of Aluminium removed to allow the laser beam to pass down the optical axis of the interferometer. The collimated beam then travels towards the beam splitter, where it is divided into the two arms.

3.3- REFERENCE MIRROR ARM :

The reference mirror is fixed in position but adjustable in orientation for optical alignment of the interferometer. Because the interferometer has been designed for dispersive or asymmetrical reflection, the sample may replace the reference mirror. The shape of the sample holder depends on the temperature of the measurements ;

1- Room temperature measurements are performed using a sample plate, held in position by two micrometers. This allows the sample to be adjusted for optical alignment of the interferometer using a laser.

2- For low temperature measurements, a cryostat can be used as a sample holder. This consists of an inner can onto which a block of copper is attached. On one end of this the sample or reference mirror is fixed. We usually use silver paint to fix the sample or the mirror. Outside the can is a vacuum jacket which needs to be pumped to at least 10^{-5} torr to prevent the sample icing up. The cryostat can either be used with liquid nitrogen at 77 k or liquid helium at 4.2 k when

boiling.

3.4- MOVING MIRROR ARM :

The moving mirror is an optical flat mounted on a high precision linear translation unit and is driven by a hydraulic piston (Burton and Parker 1984). The linear translation unit consists of a high precision cross roller bearing made by E.S.E. Ltd, model no NK3 - 180. The parallelism tolerance is less than 7μm over the complete 10 cm travel. Onto this is mounted a 50 mm diameter optically flat mirror. Springs were attached to the linear bearing to return the mirror. The bearing is coupled to the piston via a 1/4 inch silver steel rod, which passes through a Wilson vacuum seal. A stainless steel ball was soldered to both the linear bearing and the piston to give a better contact. Also the ends of the rod had a machined cone which improved contact. This was necessary to stop the contact point with the rod from varying when scanning. The piston was connected via two nylon pipes to the hydraulic reservoirs and control.

3.5- HYDRAULIC SYSTEM :

A schematic diagram of the hydraulic piston circuit is shown in figure (3.2) (Burton and Parker 1984). Hydaulic pressure is derived from a cylinder of Nitrogen, A, and a

system of solenoid operated valves in the spool valve unit, B, is used to control the gas pressure over a pair of oil reservoirs, D_1 and D_2. Pressure from the reservoirs is transmitted to the ends of a cylinder, G, containing a piston, H, which is mechanically coupled to the moving mirror drive unit. All the components were obtained from Active-Air Automation Ltd. There are two hydraulic needle valves which allow the scan speed to be varied from $1\mu ms^{-1}$ to $10mms^{-1}$. Faster speed could be obtained by increasing the bore diameter of the piston or by removing the hydraulic fluid. Full details of the hydraulic set-up have been given by Burton and Parker (1984).

3.6- HYDRAULIC CONTROL:

There are two relays to control the hydraulic movement of the piston. By switching 12v across one of the two relays it will open, and so allow the compressed nitrogen to push the hydraulic fluid, and so push the piston in one direction. If we apply 12v to the other relay, the piston will reverse direction. We use pulses which can be generated from the computer, via an IEEE interface unit, to switch states of the relays. These pulses switch the hydraulic direction, via the switching box, through a three stage system as shown in figure (3.3). This allows the piston to scan forward, stop and change direction, etc.

Because of this, multiple scanning and averaging of the data runs, to improve the signal to noise ratio, is possible.

3.7- OUTPUT OPTICS:

A reflecting arrangement has been used as the output optics. On this system, an optically flat mirror has been used to reflect the beam, after interfering at the beam splitter, to a spherical mirror. The spherical mirror condenses the beam to a focus some 10 to 15 cm away where the detector is located. Just in front of the focus there is room to place various filters. Black polyethylene has been used as a filter to cut off any high wavenumber components ($>550\ cm^{-1}$).

3.8- DETECTOR:

A Golay cell detector has been used in this work. It is a thermal detector which offers spectral coverage from 250 nm to the millimeter region with high sensitivity. Its operating principle is thermal expansion of a gas upon heating. A chamber containing a gas of low thermal conductivity is sealed at one end with a diamond or quartz window (chosen according to the spectral region required) through which radiation reaches a thin absorbing film which responds readily to infrared radiation, the film in turn

warming the gas with which it is in contact. A rise in temperature of the gas in the chamber produces a corresponding rise in pressure and therefore a distortion of the flexible mirror membrane with which the other end of the gas chamber is sealed. With the aid of a suitable optical system and a photocell the deformation in the flexible mirror membrane is transfered into changes in voltage. The change in the voltage is then recorded as a measure of the infrared absorption. The disadvantages of this detector are that the device is very fragile and is fairly slow in response. Also, this detector is very sensitive to radiation overload.

3.9- LASER FRINGES:

A helium-neon laser, supplied by Scientifica-Cook Ltd, has been used for sampling the interferogram (Burton et al 1982). The laser beam is directed down the optic axis of the system through the etched hole in the collimator mirror. Because the laser is a monochromatic source the associated interferogram will be a cosine wave. A small photo-diode (RS 305-462) has been used to detect the variation in laser beam intensity and converts it to a voltage. Because the wavelength of the laser is 632.8nm the interference fringes will be 316.4nm apart. Since the laser shares the same path as the optic axis, if there is any change in the path length

of one of the arms due to thermal effects, the laser fringes will automatically compensate. Also the laser fringe intensity can be used as a sensitive method of alignment. When the largest signal is obtained from the photo-diode, the IR signal is also the largest.

3.10- LASER CONTROL CHANNEL ELECTRONICS:

The photo-diode is placed inside the output optics chamber. The radiation excites electrons across the band-gap to produce a voltage. A low noise amplifier (Brookdeal type 435) has been used to amplify the input fringes, which are of the order 100mv to 700mv. The unit also has low and high pass filters. Since the scan speed produces fringes from 100Hz to 1kHz, the high pass filter is set to 100Hz, while the low pass is set to 1 kHz. After the amplifier the signal is sent to a fringe counting unit, see figure (3.4).

The signal will pass through two 741 op-amps, which can amplify the fringes to 10v. The gain, as well as the D.C offset, can be varied as required. After amplification the signal passes to a Schmidt trigger (TTL 7414) which generates a very sharp rising edge to 5v when the input signal is greater than 2v. This will convert the cosine wave into a square wave. Also it can be seen that, by changing the D.C offset, the trigger point of the Schmidt can be varied. After the signal has been squared, it can either

pass directly to the monostable (TTL 74221) or pass into the counting chain. The chain is constructed from two reversible binary counters (TTL 74193) which are triggered by rising edges. The counters can divide the fringes into blocks of 2 to 256, depending on the counter switch. Since the fringe spacing is 316.4nm this gives control of the spatial separation of the ADC pulses from 316.4nm to 80.998μm. A signal corresponding to the start of each block passes to the monostable (TTL 74221) to generate a narrow 5v trigger pulse. The width of the pulse can be varied by the RC pair to suit the ADC in use. Typically the values of 4.7k and 47nf are used to give a pulse width of 50μs.

3.11- ANALOGUE SIGNAL:

The output from the IR detector was sent to a simple op-amp as shown in figure (3.5). The circuit works as follows. Using a resistor chain, the input from the detector is divided by 10 and then coupled to the first amplifier. The overall chain amplifies the signal and adds an offset. This residual offset could be varied by the 5k potentiometer so that the final output D.C. voltage was between 0 and 10v. The signal was amplified by a factor of about 8 by the first op-amp, whose gain was controlled by the 39k resistor. After this, the signal was fed into the second op-amp, which controlled the final output size of the

signal by the use of the 100k potentiometer. A 47nf capacitor was coupled to the output line to filter any high frequency noise propagating up the connecting line from the computer.

3.12- ADC INTERFACE CIRCUIT:

The IEEE interface unit is a modular system called Microlink, built by Biodata Ltd. It consists of a mainframe with a power supply which can accomodate 7,12 or 18 modules depending on the specification required. For our instrument only 3 are needed. They are a high speed clock (HSC), an analogue signal conditioning module (AN-1) and an analogue to digital convertor (A-12D).

HSC:

This is used to trigger the ADC unit from the electronic trigger. It can also be used to multiplex more than one input signal if needed. This gives a maximum data rate of 20 kilobytes/second.

AN-1:

This has a switch to select the input analogue signal from 0.1v to 10v. Also there is a Gain Trimmer to set full scale input, and an offset trimmer to alter the D.C. base level.

A-12D:

This converts the analogue signal to a 12 bit digit to be read by HSC.

3.13- THE MICROCOMPUTING SYSTEM:

The computer used to control the system is a Sirius computer (now traded under the name Victor). It has two 5.25 inch floppy disc drives, each capable of storing about 600 kilobytes of data, as well as having 512 kilobytes of memory. All the programs are written in Pascal.

3.14- ANCILLARY EQUIPMENT:

In the far-infrared water vapour is a problem due to its high absorption. To eliminate most of the water vapour absorption, the system is vacuum pumped.

The instrument is mounted on an optical table, supported by four gas controlled pneumatic isolation legs, made by Ealing Optics Ltd. The pneumatic legs reduce the effect of floor bound vibrations being transmitted to the instrument.

The Mercury lamp has a water jacket to control the thermal response of the IR output, as mentioned before.

3.15- SPECTRAL RESPONSE VERSUS SCAN SPEED:

The relation between the modulation frequency of a given spectral component and scan speed can be given by the formula below

$$S = \frac{f_m}{2} \times \frac{1}{\nu_a} \qquad (1)$$

where;

f_m = modulation frequency (H_z)

ν_a = spectral component (cm^{-1})

S = scan speed (cms^{-1})

In this work the scan speed is selected by setting the corresponding modulation frequency for the laser fringes. To enable this to be done conveniently equation (1) can be rewritten as

$$L_f = \frac{f_m}{6.328 \times 10^{-5}} \times \frac{1}{\nu_a} \qquad (2)$$

where;

L_f = laser fringe frequency (H_z)

6.328×10^{-5} = laser wavelength (cm)

This function has been plotted for various modulation frequencies, and is shown in figure(3.6). The axes were chosen to be logarithimic so as to show the various modulation frequencies as straight lines.

It can be seen from figure (3.6) that by varying

the scan speed, a given spectral component will be modulated at a different frequency. Figure (3.7) shows the response of a Golay against modulation frequency, it can be seen that the best response is around 1 to 2 Hz.

3.16- INSTRUMENTATION TEST:

1- WATER VAPOUR:

The ideal choice for testing the instrumental system is that of using water vapour as a test material because of thousands of absorption bands in the IR. These have been measured and catalogued by various groups, but the results of Rao et al (1966) have been used in this work.

The ratio spectrum of water vapour is shown in figure (3.8). We found that the spectral components are in excellent agreement with the data of Rao et al (1966).

2- GaAs OPTICAL CONSTANTS:

GaAs is the substrate of all the samples used in this work, as well as one of the sample components. Because of this we found it is useful to calculate the optical constants of GaAs and compare the measured values with the values calculated from a classical model of a damped simple harmonic oscillator. Also this could be used as a second test of the instrument.

The amplitude r and the phase ϕ of the complex reflectivity of GaAs at room temperature are shown in figure (3.9). These data have been used to calculate the refractive index n and absorption index k, figure (3.10), using

equation (2.41).

The theoretical calculation of the amplitude r and the phase ϕ of bulk GaAs at room temperature using the data of Kim and Spitzer (1979) are shown in figure (3.11). Figure (3.12) shows the calculated refractive index n, and absorption index k. The overall agreement between measurements and calculation is good in all cases.

3.17- REFERENCES;

Active Automation Ltd, 30 Station Road, Belmont, Sutton, Surrey.

Biodata Ltd, 6 Lower Ormond Street, Manchester.

Brookdeal Electronics Ltd, Market Street, Bracknell, Berkshire.

N J Burton, C.L. Mok and T.J. Parker; Int. J. Infrared and Millimetre Waves, 3, 331, (1982).

N J Burton and T.J. Parker; Int. J. Infrared and Millimetre Waves, 5, 803, (1984).

O K Kim and W G Spitzer, J. Appl. Phys. 50, 4362 (1979).

K N Rao, C J Humphreys and D H Rank; "Wavelength standards in the infrared" Academic Press, New York (1966).

Ealing
WARNING

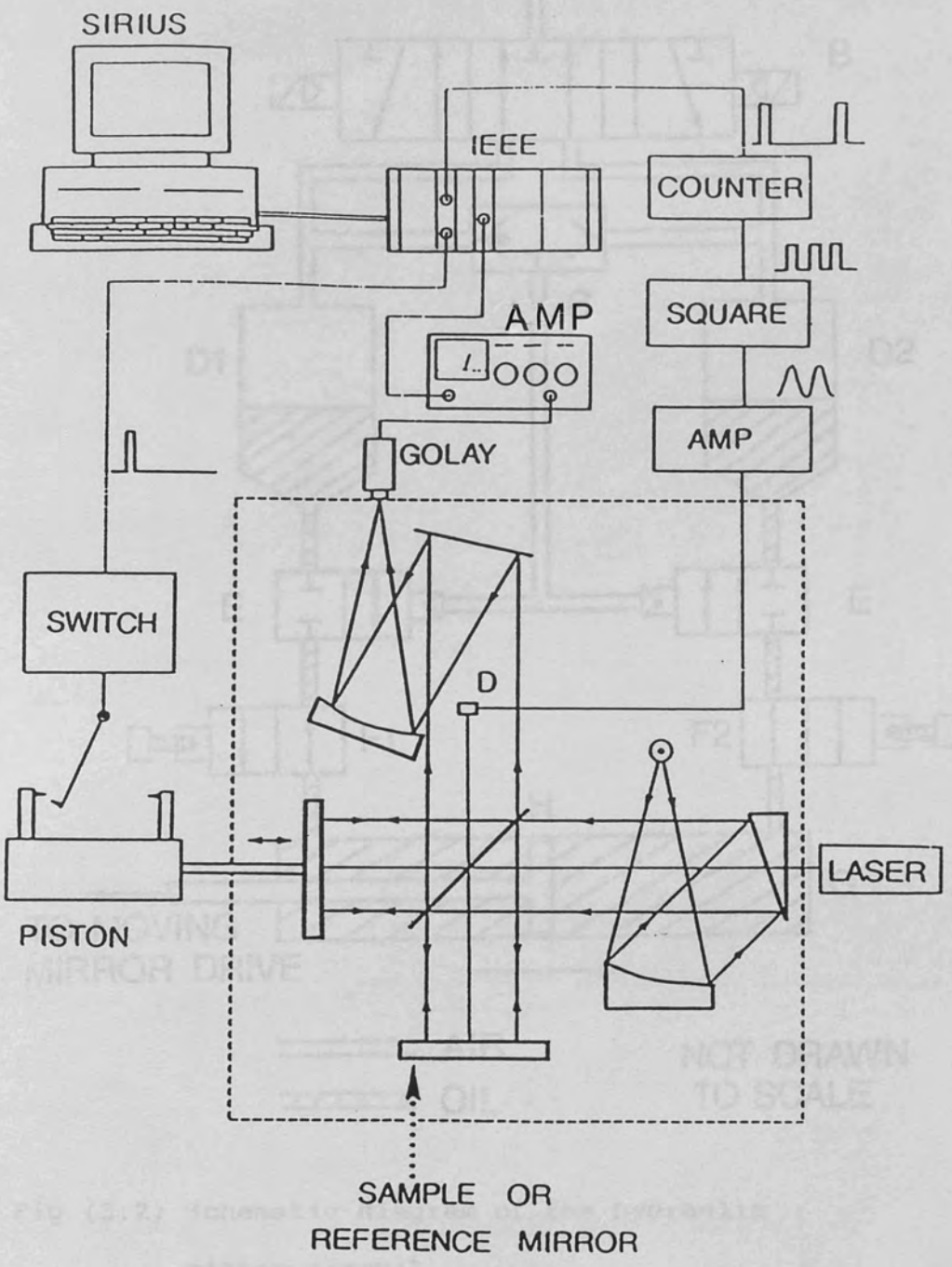

Fig (3.1) Schematic diagram of the reflection DFTS instrument

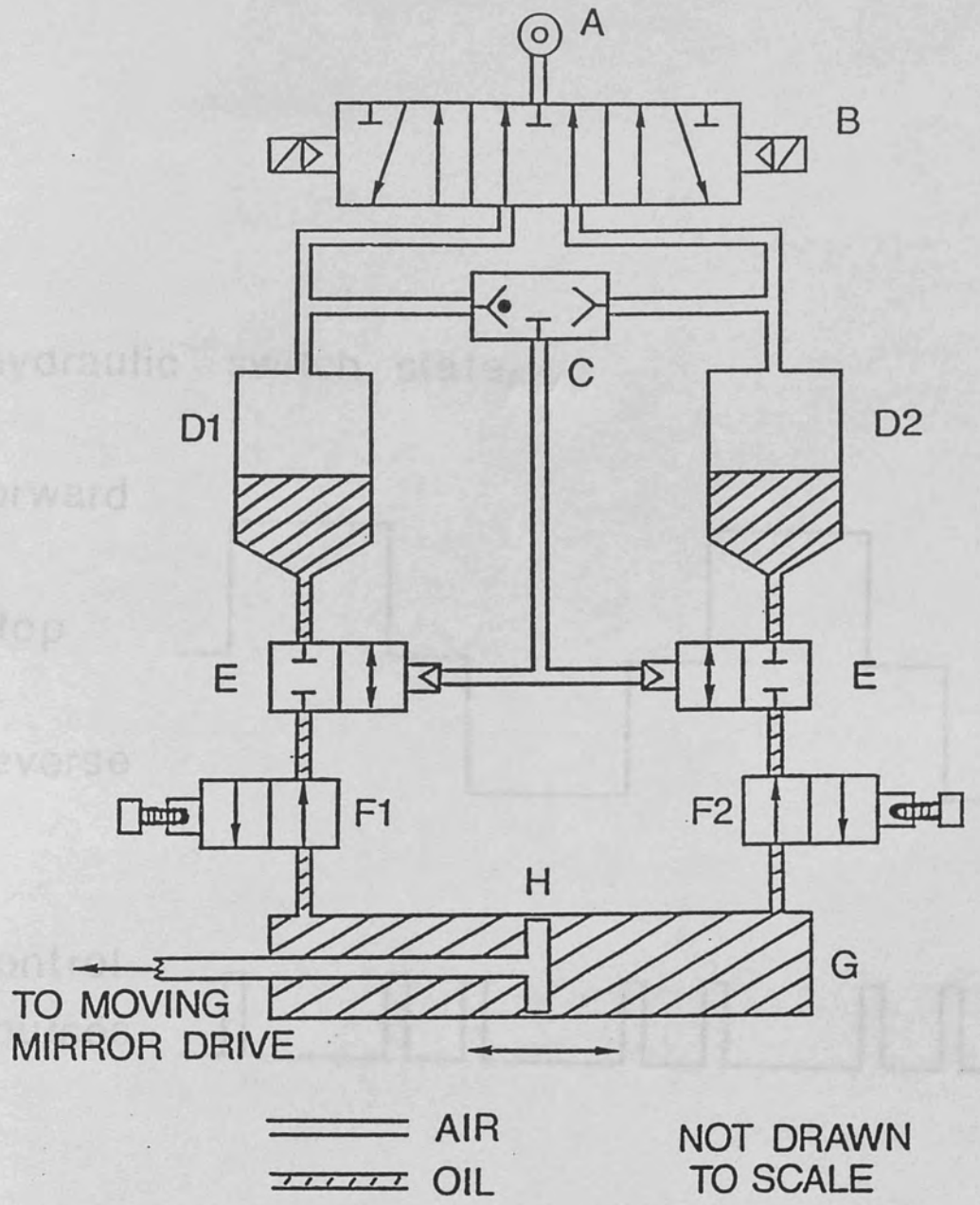

Fig (3.2) Schematic diagram of the hydraulic piston circuit

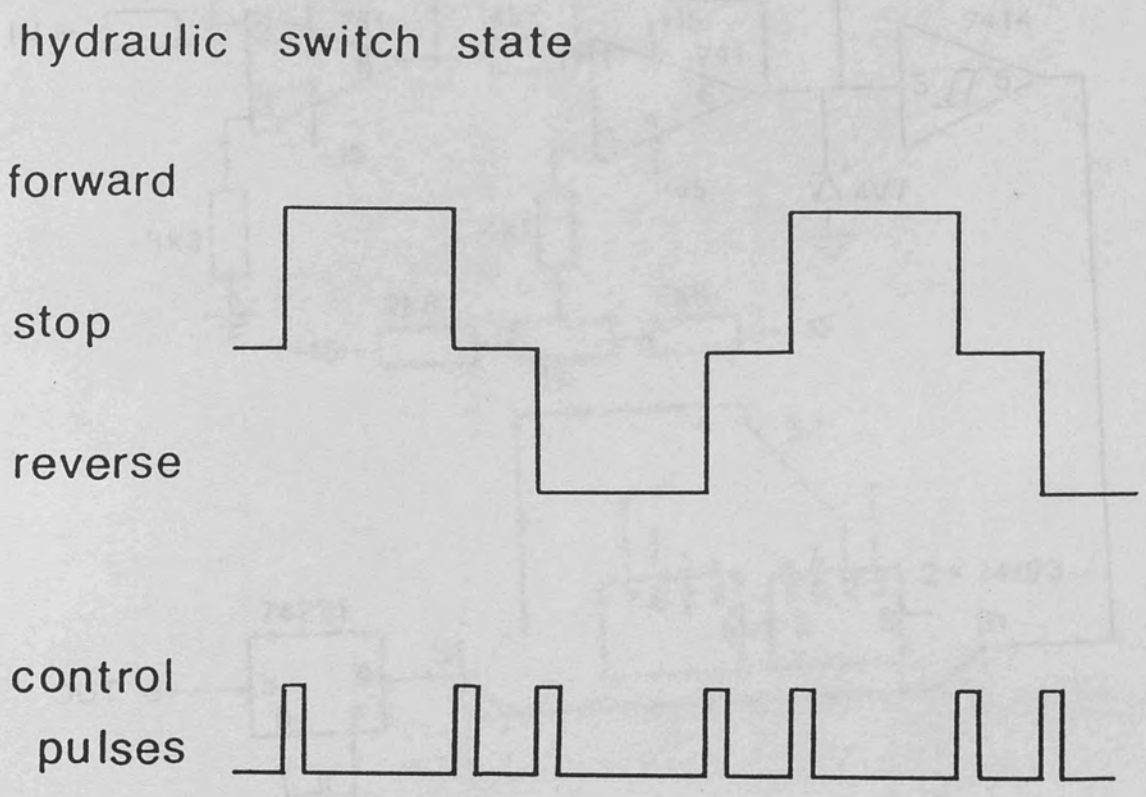

Fig (3.3) Schematic diagram showing the control of the hydraulic piston direction

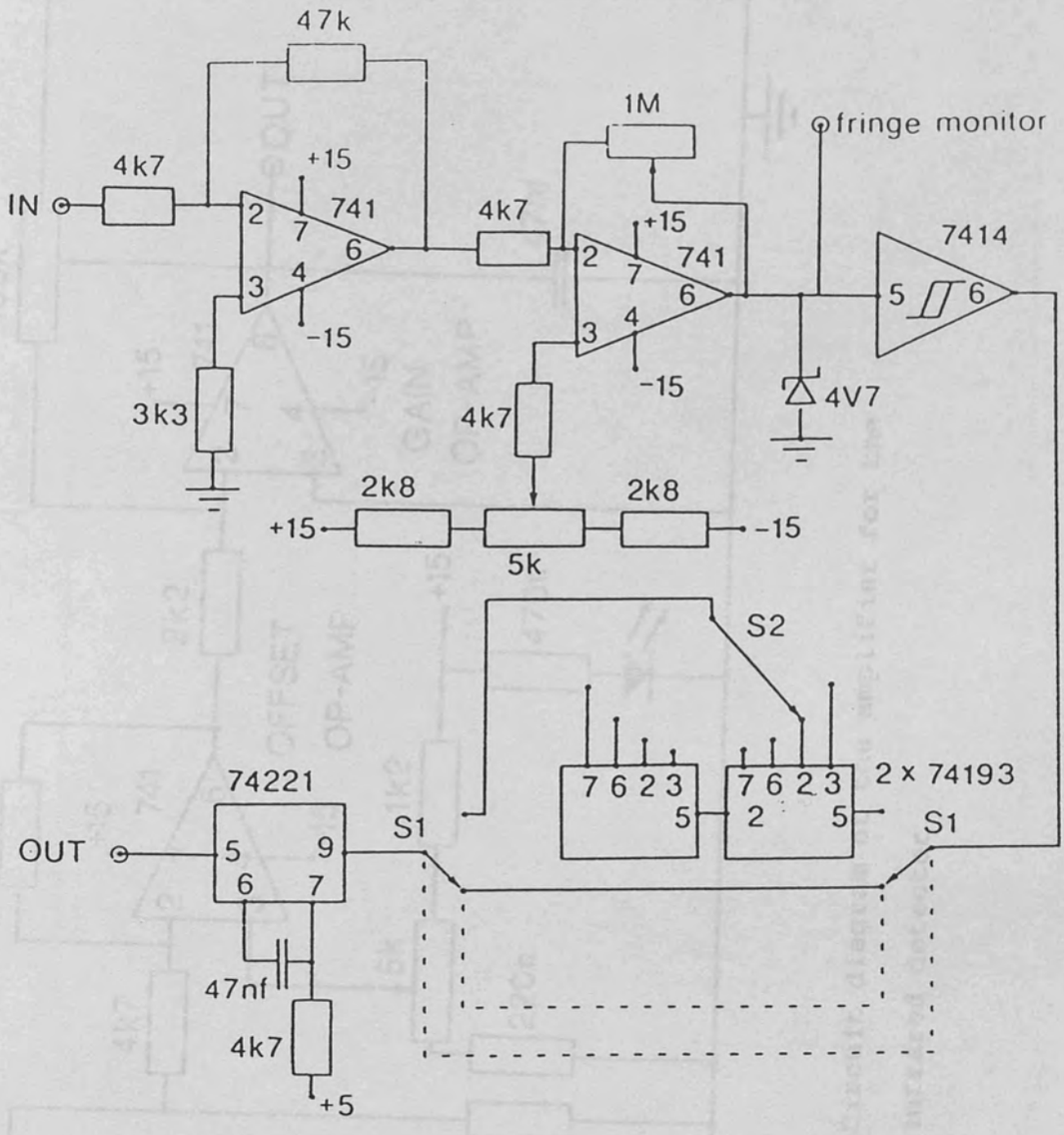

Fig (3.4) Laser fringe amplifier and counting circuit diagram

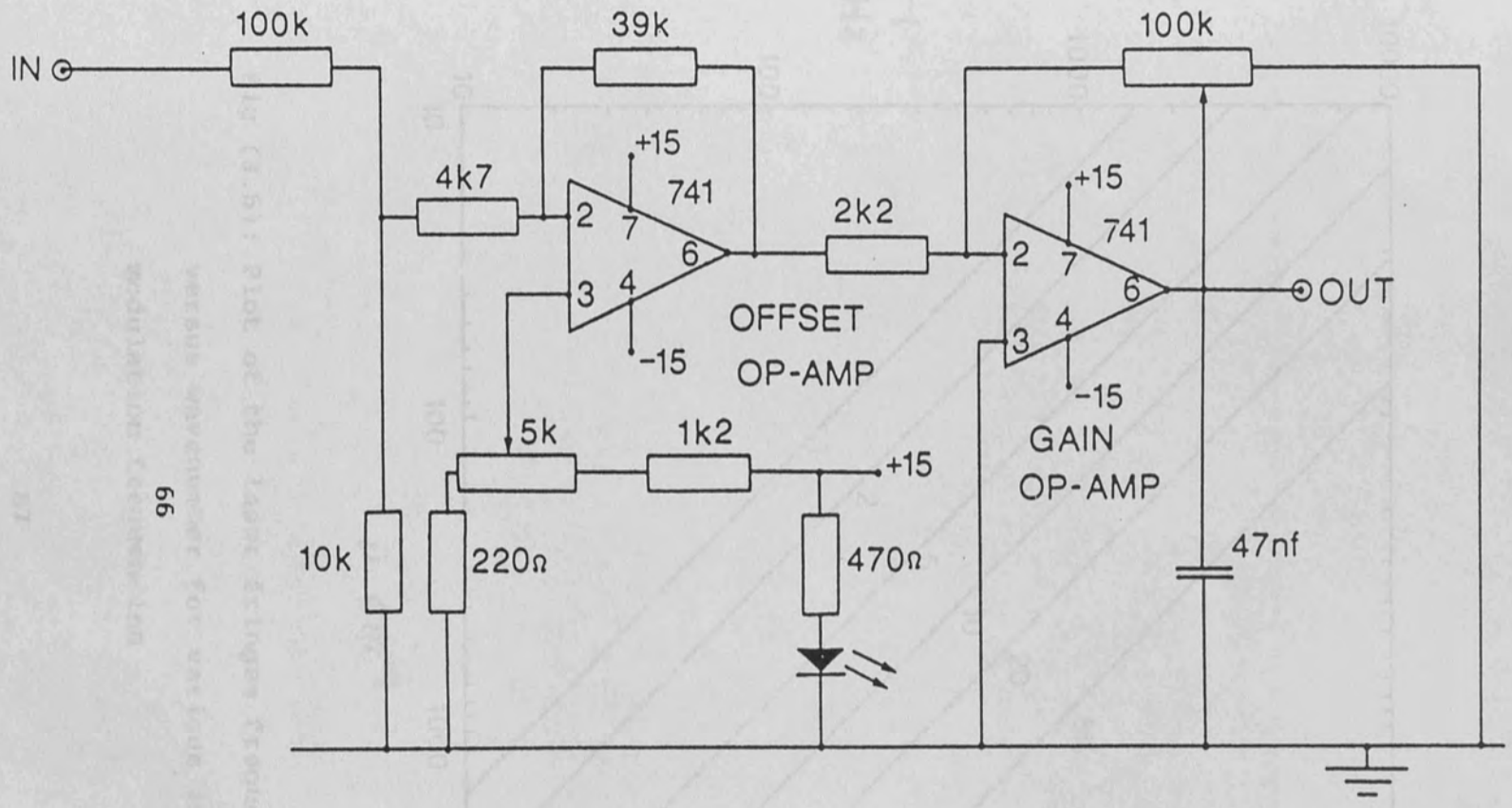

Fig (3.5) Circuit diagram of the amplifier for the infrared detector

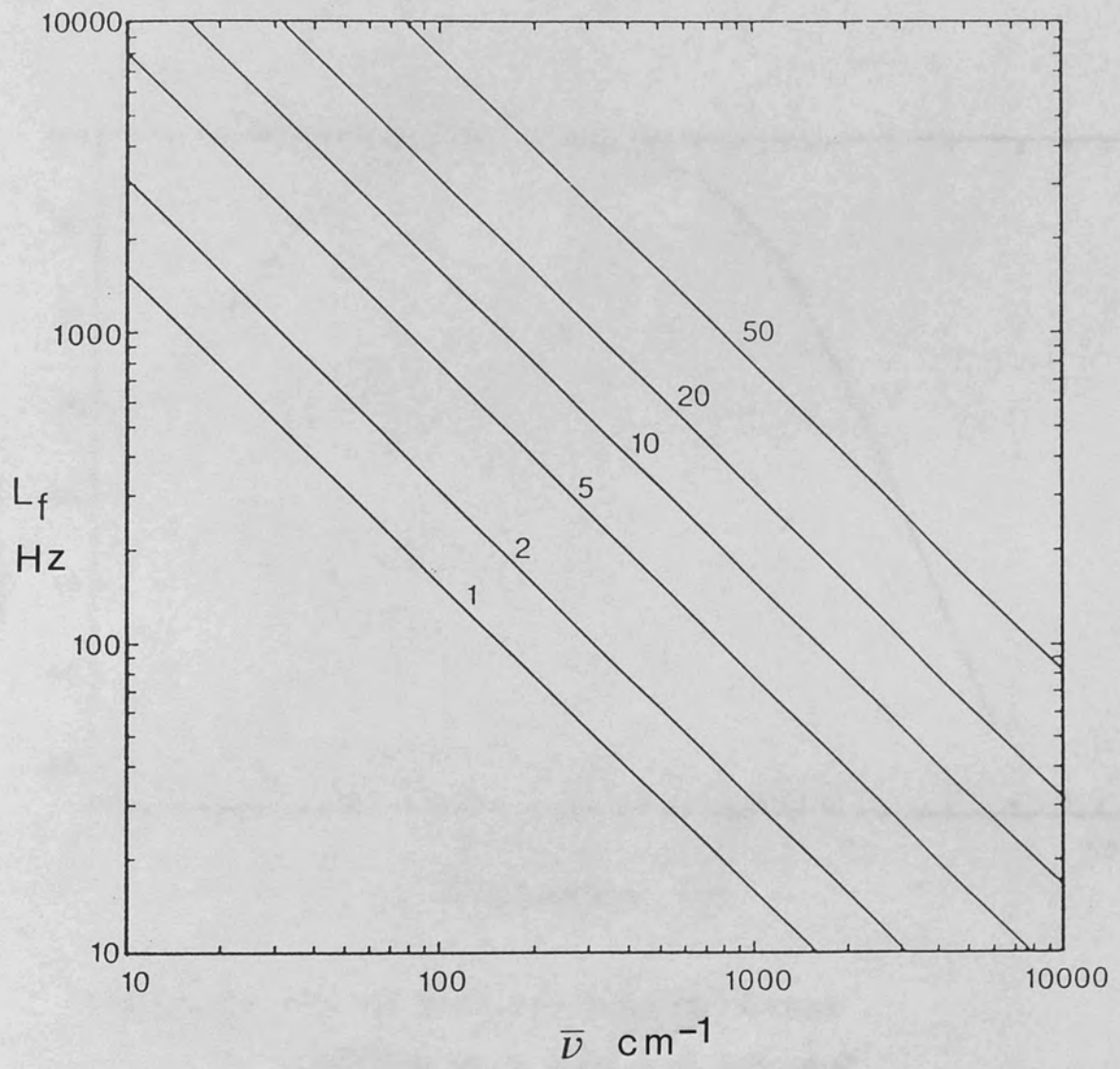

Fig (3.6): Plot of the laser fringes frequency versus wavenumber for various infrared modulation frequencies

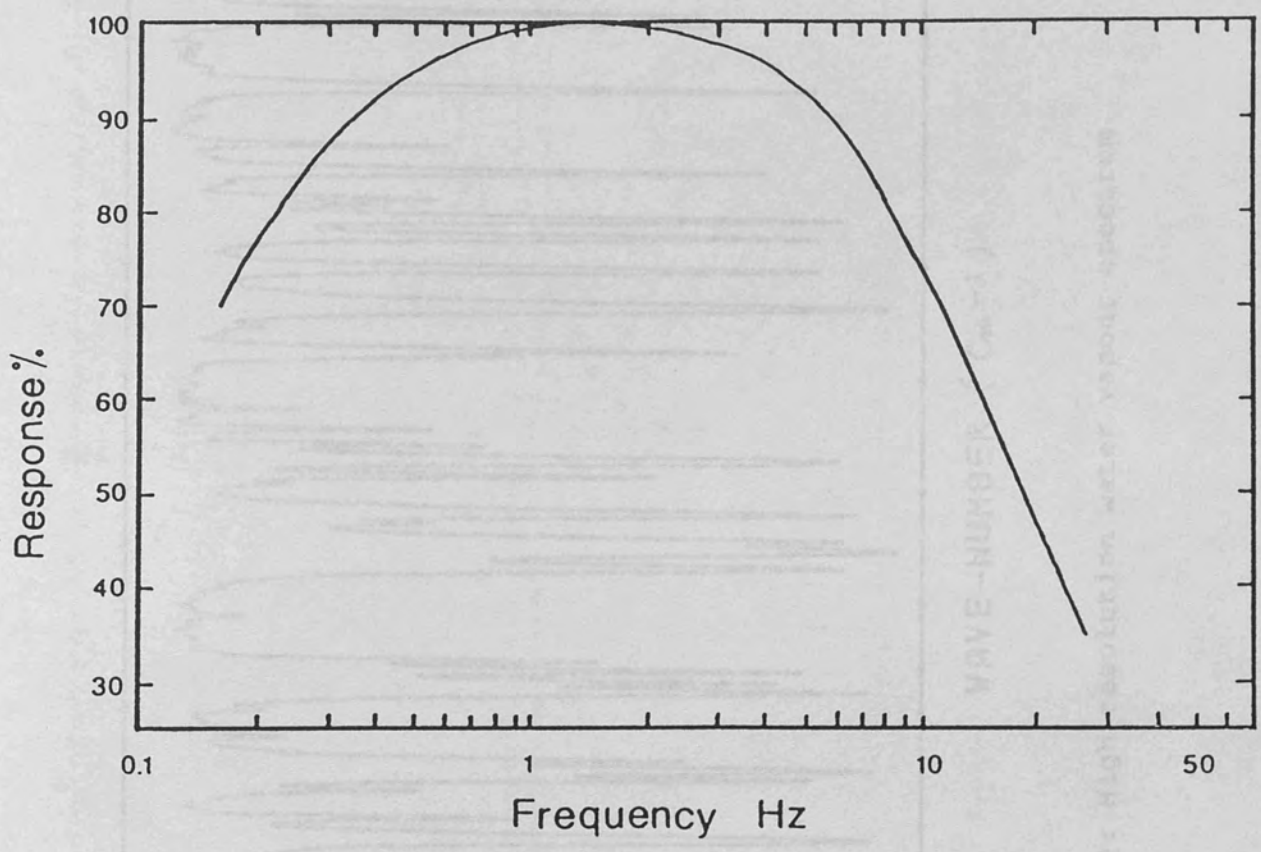

Fig (3.7): Plot of absolute response versus frequency of a modulated infrared signal for a Golay detector

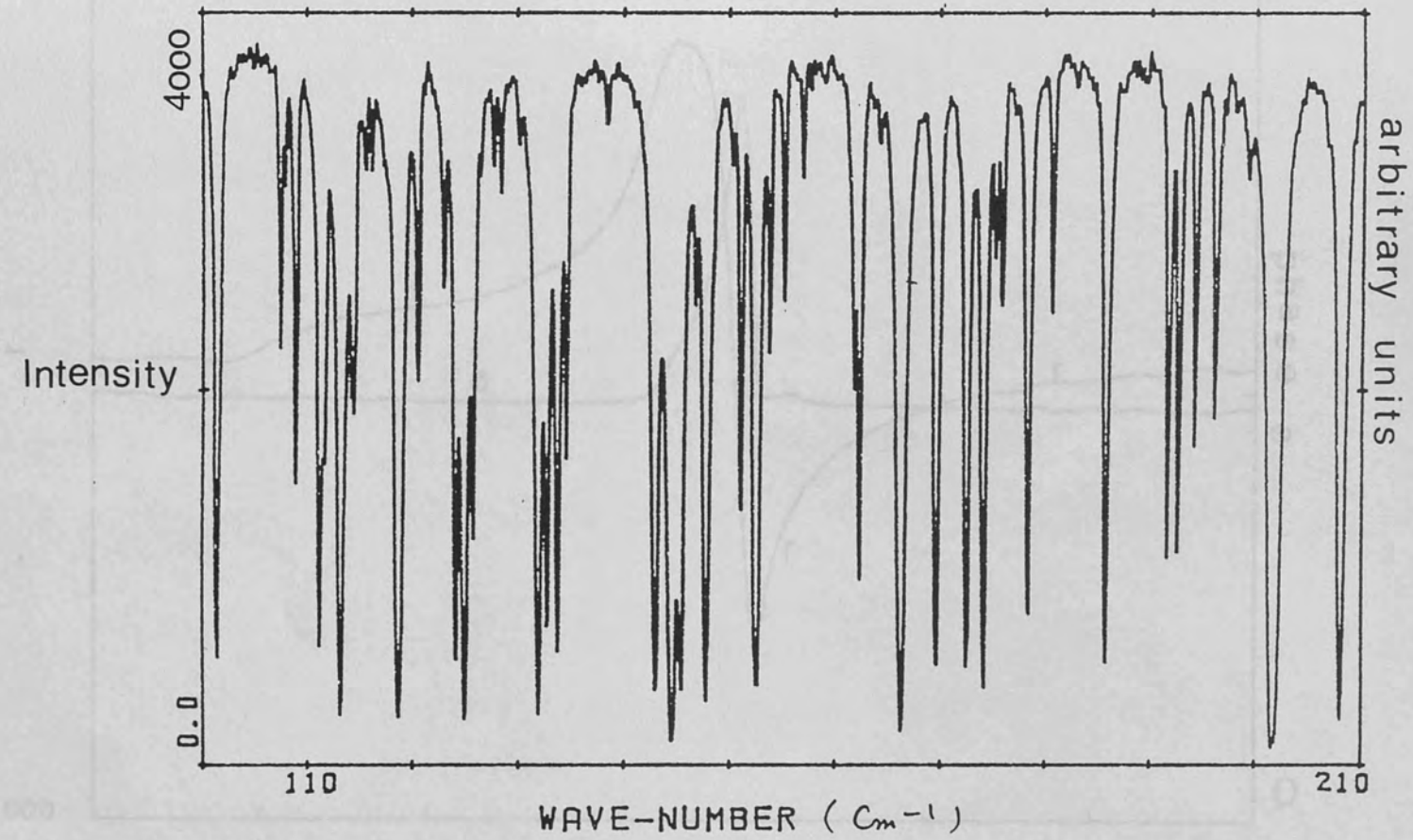

Fig (3.8): High resolution water vapour spectrum

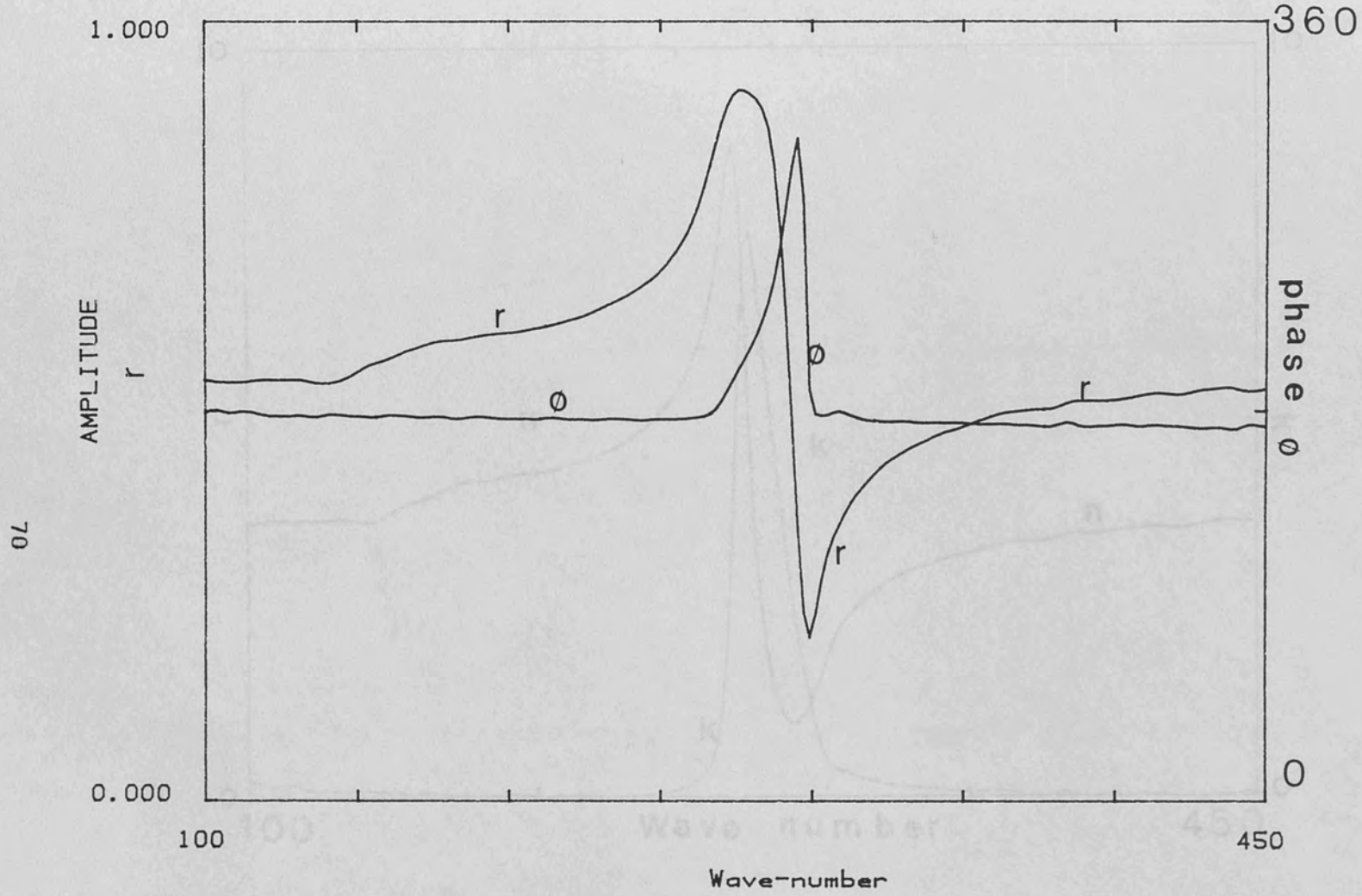

Fig (3.9): The measured reflectivity r and phase ϕ for GaAs at room temp.

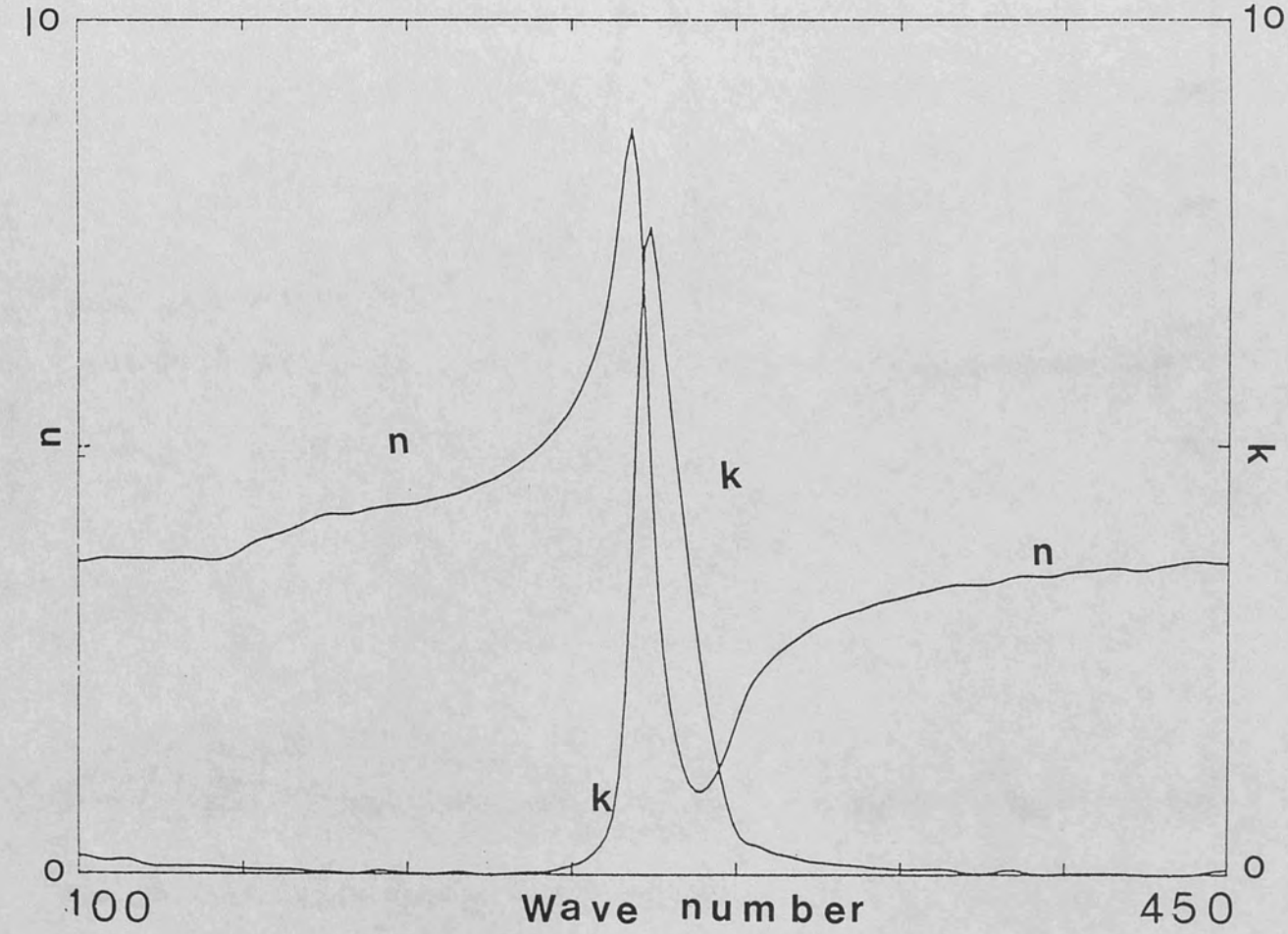

Fig (3.10): Refractive index n and absorption index k for GaAs at room temperature

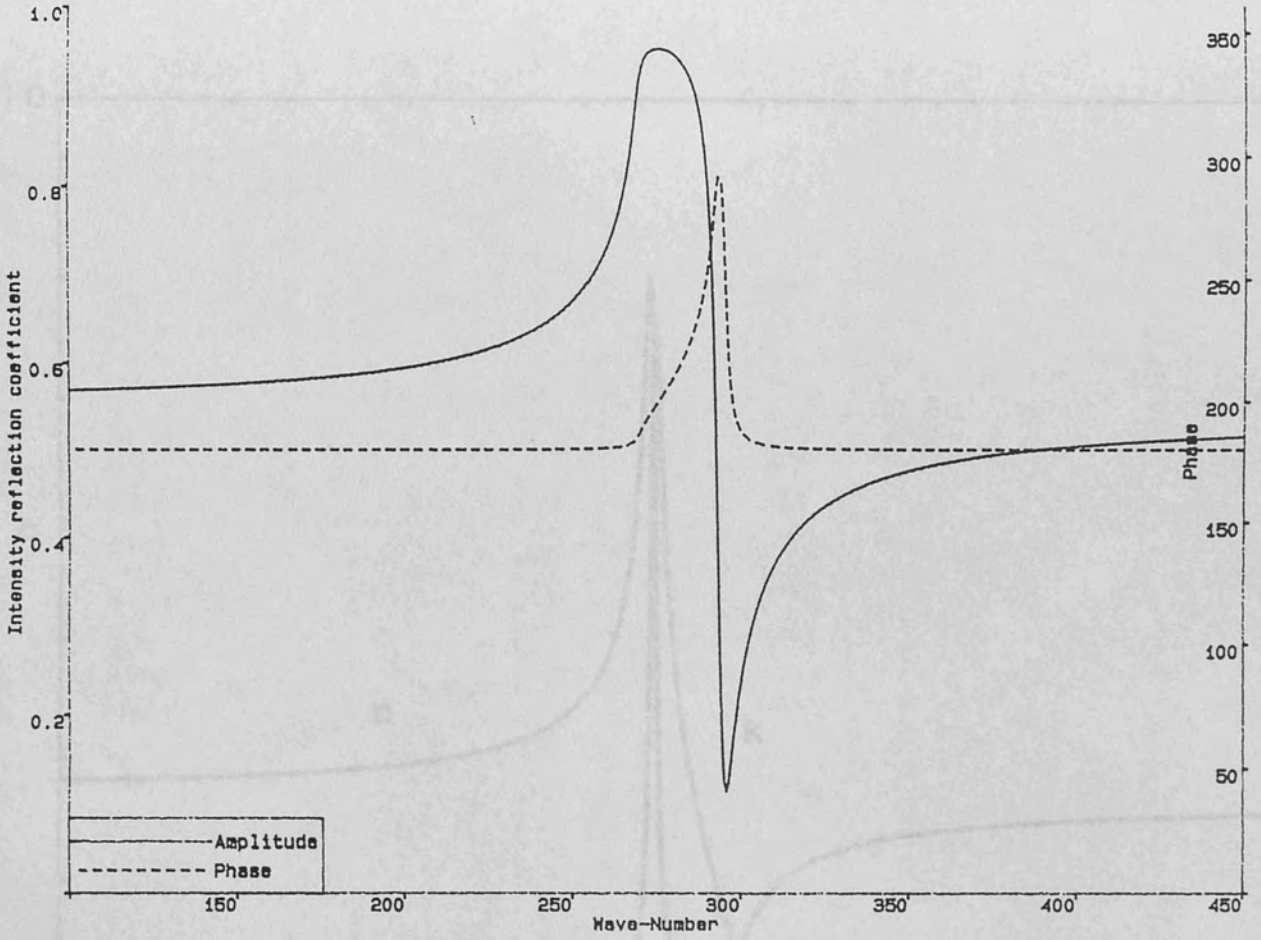

Fig (3.11): Calculated r and ϕ for GaAs

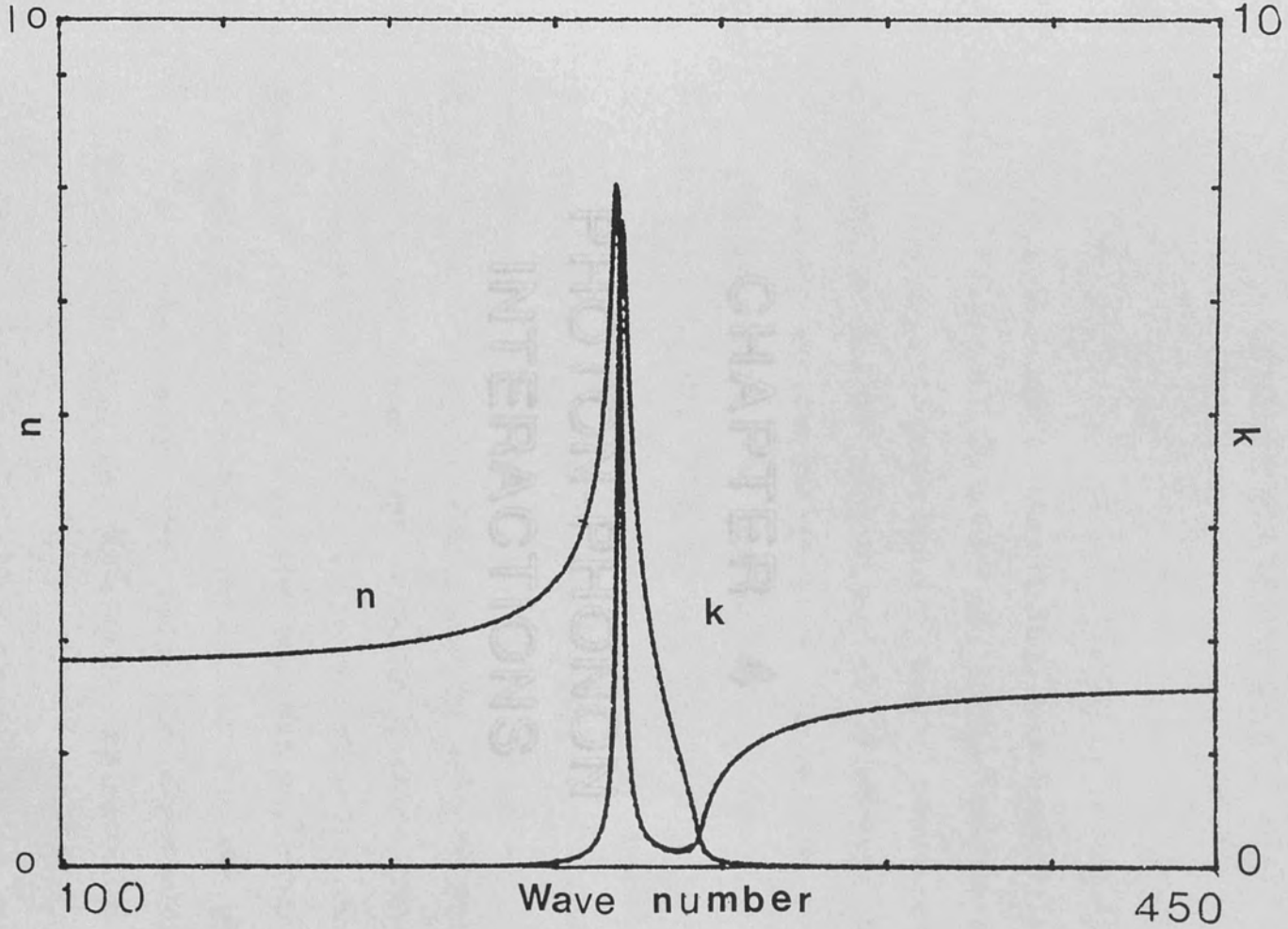

Fig (3.12): Calculated r and ϕ for GaAs

CHAPTER 4

PHOTON-PHONON INTERACTIONS

CHAPTER (4)

PHOTON-PHONON INTERACTIONS

4-1 INTRODUCTION :

Many years ago (Kittel 1976), the word polariton was used to describe a mode of mixed phonon-photon character. Nowadays polaritons are regarded as quasi-particles in solids consisting of a photon coupled with an elementary excitation (e.g, a phonon, exciton, or magnon) which polarizes the medium. Otherwise the word polariton is used to describe any mixed mode involving a photon. The existence of such coupled mechanical-electromagnetic excitations in solids was first predicted in 1951 by Huang for cubic ionic crystals of the NaCl type. The theory of polaritons was summarized in 1954 by Born and Huang in their well-known text book on lattice dynamics. Experimental evidence for the existence of polaritons was given first by Henry and Hopfield in 1965 on cubic GaP. Further important experimental investigations of phonon-polaritons in those early days were the experiments of Porto et al on ZnO in 1966 and on α-quartz by Scott et al in 1967.

Although there has been a steady growth of interest in bulk polaritons, the latter half of the 1970s saw the

development of a strong interest in surface polaritons. A surface polariton is an electromagnetic wave travelling along an interface with an amplitude decaying exponentially with distance from the interface. The first study of surface waves, which was based on lattice dynamics, was due to Lifschitz and Rosenzweig in 1948. These authors recognized that in diatomic crystals like NaCl, in addition to the acoustic surface waves which become the usual Rayleigh waves in the continuum limit, $k_{\parallel} \rightarrow 0$, optical surface modes may occur. Recently, the attenuated total reflection (ATR) method has been applied to the study of surface polaritons for the first time by Bryksin et al on NaCl (1971).

The dispersion of the dielectric function of a semiconductor multilayered structure is determined by a number of resonances at different frequencies. For a doped semiconductor multilayer, the lowest frequency response (50-150 cm^{-1}) arises from the collective, or plasma, oscillations of the gas of free carriers (Boardman, 1982 and Cottam and Tilley, 1989). In polar lattices the second response is due to coupling of the electromagnetic field with TO phonons. This leads to a reststrahl frequency region (100-500 cm^{-1}) which might be discussed within the bulk-slab model by means of the effective-medium approximation to that model. The basic assumption which is made is that each component layer of the multilayer samples is sufficiently thick to be described by the corresponding bulk dielectric

function. Otherwise, when each layer is many monolayers thick, then it is possible that the local and distant fields should be related in the same way as in the bulk, and we may employ the bulk slab-model with some confidence. Reviews of the bulk-slab model have been given by Yariv and Yeh (1977) and Raj and Tilley (1985).

A theoretical study of ATR on semiconductor superlattices in the reststrahl frequency region has been done by Raj and Tilley in 1987.

4.2 THE DISPERSION RELATION OF INTERFACE POLARITONS:

To investigate phonon polaritons, the following procedure is given in Boardman (1982) and Raj and Tilley (1985). We consider the plane interface between two semi-infinite dielectric media as shown in figure (4.1). Suppose we have an electric field with components both perpendicular and parallel to the Z=0 boundary of fig (4.1). We take the Z axis normal to the interface and the X-axis as the direction of propagation of the mode. For a plane wave with all fields proportional to $\exp(ik_x x - i\omega t)$, since there is no surface mode with E- field in the Y-direction, we take $\underline{E}$ in the X-Z plane;

$$E = (E_{1x}, 0, E_{1z})\exp(ik_x - i\omega t)\exp(ik_{1z}) \qquad (4.1)$$

in medium (1), with a similar form in medium (2). We take a

single frequency ω, and since the boundary conditions will be applied in the whole plane Z=0, the wave vector q_x must be the same in both media. For the mode to be localised, E must decrease with the distance from the interface $I_m(k_{1z}) > 0$ and $I_m(k_{2z}) < 0$. In order for equation (4.1) to satisfy Maxwell's equations in both media, the wave vectors must satisfy;

$$k^2_x + k^2_{iz} = \epsilon_i \omega^2/c^2 \qquad (4.2)$$

$$i = 1,2$$

The equation $\nabla.D = 0$ gives the ratios of the field amplitudes in equation (4.1)

$$k_x E_{ix} + k_{iz} E_{iz} = 0 \qquad (4.3)$$

The amplitudes in the two media are related by the continuity of the tangential component of $\underline{E}$ and the normal component of $\underline{D}$

$$E_{1x} = E_{2x} \qquad (4.4)$$

$$\epsilon_1 E_{1z} = \epsilon_2 E_{2z}. \qquad (4.5)$$

From equation (4.1)

$$k_x E_{1x} + k_{1z} E_{1z} = 0 \qquad (4.6)$$

$$k_x E_{2x} + k_{2z} E_{2z} = 0. \qquad (4.7)$$

Substracting equation (4.7) from equation (4.6) gives;

$$k_x(E_{1x} - E_{2x}) + k_{1z} E_{1z} - k_{2z} E_{2z} = 0. \qquad (4.8)$$

Since $E_{1x} = E_{2x}$

it leads to

$$k_{1z} E_{1z} = k_{2z} E_{2z}$$

$$\epsilon_1 k_{1z} E_{1z} / \epsilon_1 = \epsilon_2 k_{2z} E_{2z} / \epsilon_2$$

$$k_{1z} / \epsilon_1 = k_{2z} / \epsilon_2. \qquad (4.9)$$

Substitution from equation (4.2) leads to the explicit result

$$k^2_x = (\omega^2/c^2)\epsilon_1 \epsilon_2 / \epsilon_1 + \epsilon_2 \qquad (4.10)$$

Equation (4.10) represents the dispersion relation of the excitation. By neglecting the damping, ϵ_1 and ϵ_2 are both real. Equation (4.9) shows that for surface polaritons to exist, ϵ_1 and ϵ_2 must have opposite signs, ie

$$\epsilon_1 \epsilon_2 < 0 \qquad (4.11)$$

Since the right hand side of equation (4.10) must be positive, we have

$$\epsilon_1 + \epsilon_2 < 0 \qquad (4.12)$$

Equations (4.11) and (4.12) determine the frequency intervals in which the surface polaritons occur. As an example of surface phonon polaritons on cubic crystals, the dispersion curves of the surface wave on semi-infinite GaP (Marschall et al, 1972) are shown in fig (4.2).

4-BULK POLARITON DISPERSION CURVES FOR SUPERLATTICES :

We take the Z-axis normal to the layers of the superlattice which have thicknesses a,b and isotropic frequency -dependent dielectric functions $\epsilon_1(\omega)$ and $\epsilon_2(\omega)$. The dispersion relation for a mode of wave number (k_x, k_z) is given by Yeh et al (1977), Yariv and Yeh (1977,1984) and Raj and Tilley (1985) as,

$$\cos(k_z\Lambda) = \cos(q_1a)\cos(q_2b) - g_{s,p}\sin(q_2b) \qquad (4.13)$$

where;

$$q^2_i = (\epsilon_i\,\omega^2/c^2 - k^2_x), \qquad i=1,2 \qquad (4.14)$$

$$g_s = 1/2\,(q_2/q_1 + q_1/q_2) \qquad (4.15)$$

which applies for S-polarisation (E in the Y direction)

$$g_p = 1/2(\epsilon_2q_1/\epsilon_1q_2 + \epsilon_1q_2/\epsilon_2q_1) \qquad (4.16)$$

which applies for P-polarisation (E in the X_Z plane)
and $\Lambda = a + b$ is the spatial period of the superlattice.
In the long-wavelength limit, if

$$k_z\Lambda \ll 1 \quad , \quad k_x\Lambda \ll 1,$$

$$q_1\Lambda \ll 1 \quad \text{and} \quad q_2\Lambda \ll 1,$$

for S-waves equation (4.13) reduces to

$$k^2_x + k^2_z = (\omega^2/c^2)(\epsilon_1a + \epsilon_2b)/(a+b) \qquad (4.17)$$

and for P-waves to

$$k^2_z(a+b) + k^2_x(\epsilon_1 a + \epsilon_2 b)(\epsilon_2 a + \epsilon_1 b)/\epsilon_1\epsilon_2 =$$

$$(\omega^2/c^2)(\epsilon_1 a + \epsilon_2 b)(a+b). \qquad (4.18)$$

Equation (4.18) has the following solutions;

$$k_z = 0 \qquad (4.19)$$

$$\epsilon_1 a + \epsilon_2 b = 0 \qquad (4.20)$$

$$\epsilon^{-1}_{xx} k^2_z + \epsilon^{-1}_{zz} k^2_x = \omega^2/c^2 \qquad (4.21)$$

with

$$\epsilon_{xx} = (\epsilon_1 a + \epsilon_2 b) / (a+b) \qquad (4.22)$$

$$\epsilon^{-1}_{zz} = (\epsilon^{-1}_1 a + \epsilon^{-1}_2 b) / (a+b) \qquad (4.23)$$

Using equations (4.17) and (4.21), Raj, Camley and Tilley (1987) have obtained the theoretical dispersion curves for bulk modes of a GaAs/$Al_xGa_{1-x}As$ superlattice, using the parameters obtained by Maslin et al (1986), where ϵ_1 and ϵ_2 are the frequency dependent dielectric functions of GaAs/ $Al_xGa_{1-x}As$ respectively. Both dielectric functions are described by the usual reststrahl region expression

$$\epsilon = \epsilon_\infty + \rho_1\omega^2_1/(\omega^2_1-\omega^2-i\omega\gamma_1) + (\omega^2_2-\omega^2-i\omega\gamma_2) \qquad (4.24)$$

where ϵ_∞ is the background dielectric constant, ω_1 and ω_2 are frequencies of the TO phonon resonances with γ_1 and γ_2

corresponding damping parameters, and ρ_1 and ρ_2 are the dipole strengths of the resonance. These bulk dispersion curves are shown in figure(4.3)

5-SURFACE POLARITON DISPERSION CURVES FOR A SUPERLATTICE :

In the effective-medium description, a semi-infinite superlattice is a uniaxial medium with a principal axis normal to the surface. The dispersion equation for the surface polariton is then (Hartstein et al 1973 and Borstel and Falge 1977)

$$k_x = \frac{\omega^2}{c^2} \epsilon_m \frac{\epsilon_z(\epsilon_{xx} - \epsilon_m)}{\epsilon_{xx}\epsilon_{zz} - \epsilon^2_m}$$

where ϵ_m is the dielectric constant of the bounding medium. The localisation requirement $\epsilon_{xx} < 0$ must be satisfied. Modes with $\epsilon_{zz} < 0$ are called real excitation surface polaritons, while modes with $\epsilon_{zz} > 1$ are called virtual-excitation or photon-induced surface polaritons. In fig (4.3) we show the surface-polariton dispersion curves (Raj, Camley and Tilley 1987) together with the ATR scan line. The crossing of the frequency scan line with the branches of the surface-polariton dispersion curves gives the dips in the ATR spectrum which will be discussed later. Figure (4.4) shows two distinct types of surface-polariton. The full-line curves represent the case when both ϵ_{xx} and ϵ_{zz} are negative, the real surface modes. The dashed curves

represent the case when ϵ_{xx} is negative but simultaneously ϵ_{zz} is positive, the virtual surface modes. The dispersion curve shows that there are four surface-mode branches. The first and the fourth branches (we refer to the branch starting at the lowest frequency as the first and so on) are a mixture of a real and virtual surface mode. However for the first branch the virtual-excitation part exists over a very small frequency range and can not be seen on the scale. The second branch is a real surface excitation throughout, and the third branch is a virtual surface excitation throughout.

REFERENCES :

A D Boardman, "Electromagnetic Surface Modes", ed. A D Boardman (Wiley, Chichester) 1982.

M Born and K Huang, Dynamical Theory of Crystal Lattices (Clarendon press,Oxford,1954)

M G Cottam and D R Tilley "Introduction to Surface and Superlattice Excitations", (CUP Cambridge), 1989.

M Born and K Huang, Dynamical Theory of Crystal Lattices (Clarendon press,Oxford,1954)

G Borstel and H J Flage, 1977, Phys. Stat. Sol. (b) 83, 11, (1978)

U V Bryksin, Yu M Gerbshtein and D N Mirlin, Flz, Tverd. Tela, 13, 2125(1971)[English transl.:Soviet phys. solid state, 13, 1779 (1972)]

A Hartstein, E Burstein, A A Maradudin, R Brewster, and R F Wallis, J. Phys. C 6, 1266, 1973

C H Henry and J J Hopfield, Phys. Rev. Lett. 15, 664 (1965)

K Huang,Proc.Roy.Soc.London, A208,352 (1951)

C Kittel, "Introduction to solid state physics", Willey & Sons Inc, New York (1976)

I M Lifschitz and L N Rosenzweig, Zh. Eksp. Teor. Fiz., 18, 1612 (1948)

N Marschall and B Fisher, Phys. Rev. Lett., 28, 811, 1972.

K A Maslin, T J Parker, N Raj, D R Tilley, P J Dobson, D

Hilton and C T B Foxon, Sol. State comms 60, 461, 1986

S P S Porto, B Tell and T C Damen, Phys. Rev. Lett., 16, 450 (1966)

N Raj, R E Camley, and D R Tilley J. Phys. C 20, 5203, 1987

N Raj and D R Tilley, Sol. State Comms, 55, 373, 1985

N Raj and D R Tilley, Phys. Rev. B 36, 7003, 1987.

J F Scott, L E Cheesman and S P S Porto, Phys. Rev., 162, 834 (1967).

A Yariv and P Yeh J. Opt. Soc. Am. 67, 423, 1977.

A Yariv and P Yeh, "Optical Waves in Crystals", Wiley & Sons Inc, New York (1984)

P Yeh, A Yariv and C S Hong, J. Opt. Soc. Am 67, 423, 1977

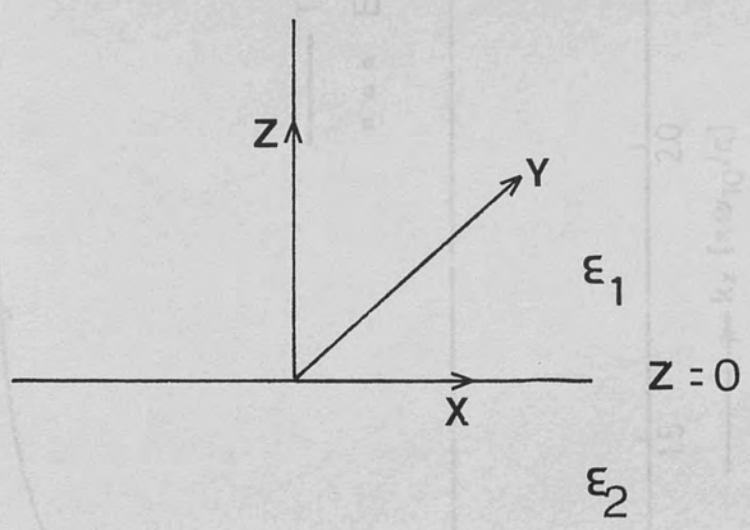

Fig (4.1): Schematic diagram of a plane interface between two semi-infinite dielectric media

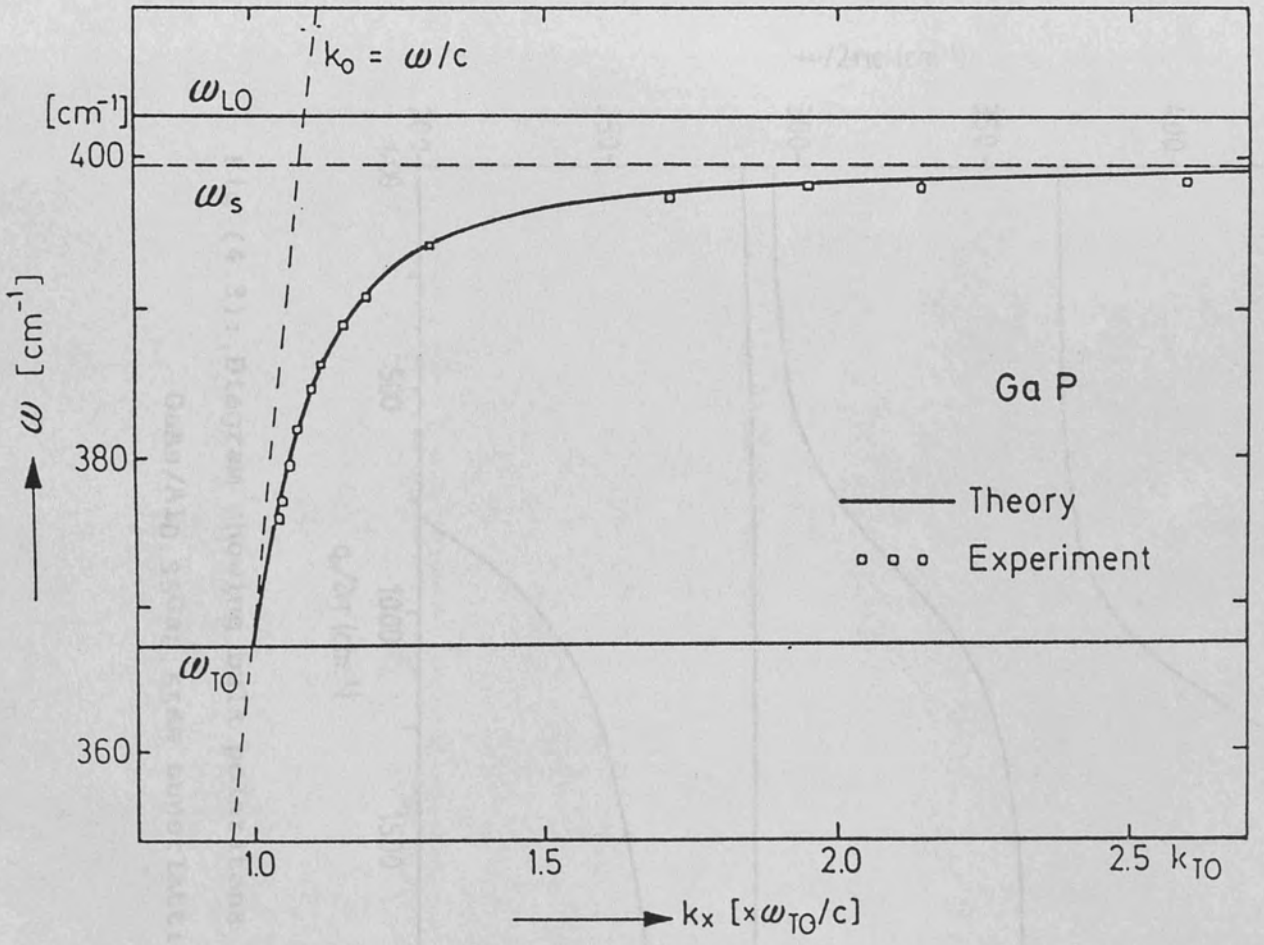

Fig (4.2): The dispersion curves of the surface wave on semi-infinite GaP

(Marschall et al, 1972)

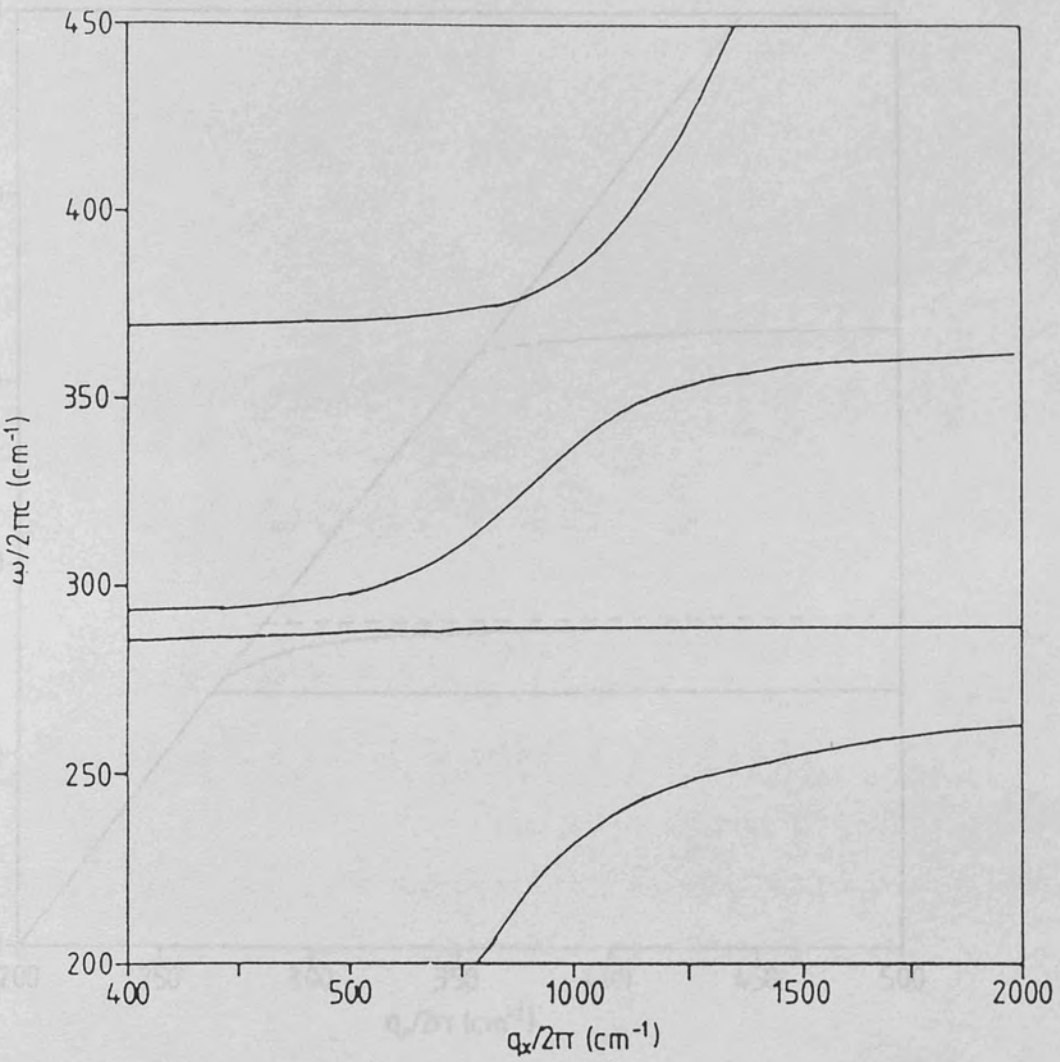

Fig (4.3): Diagram showing bulk polaritons for a $GaAs/Al_{0.35}Ga_{0.65}As$ superlattice

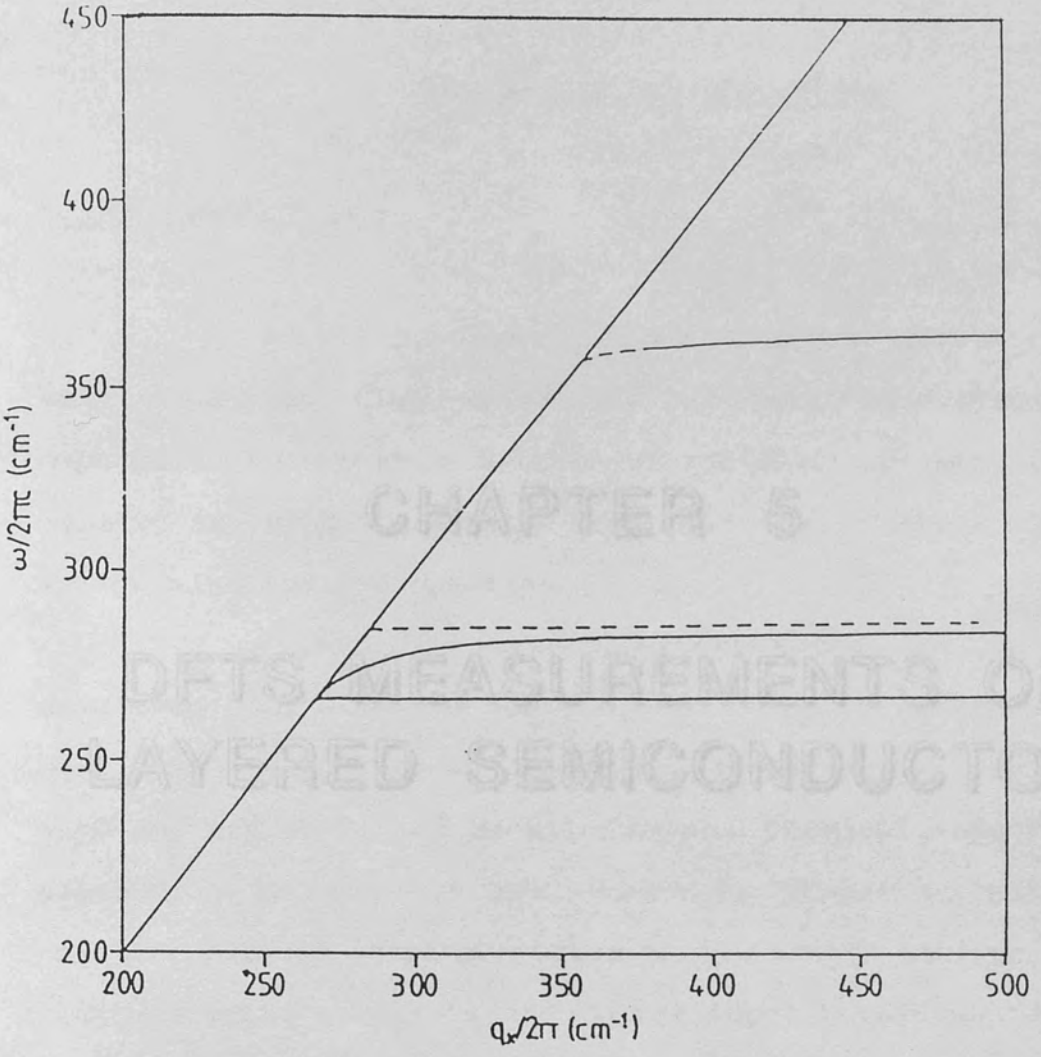

Fig (4.4): Diagram showing the surface polariton for a $GaAs/Al_{0.35}Ga_{0.65}As$ superlattice

CHAPTER 5

DFTS MEASUREMENTS ON LAYERED SEMICONDUCTOR

CHAPTER (5)

DFTS MEASUREMENTS

ON LAYERED SEMICONDUCTORS

5.1- INTRODUCTION :

Recently, layered semiconductors have attracted much attention from scientists in both theoretical and experimental areas. Lattice-vibrational properties of layered semiconductors have been much less studied compared to the electronic properties.

A number of crystal growth techniques have been developed for the production of layered semiconductor specimens. Among these, the main techniques are molecular beam epitaxy (MBE) and metallo-organic chemical vapour-phase deposition (MOCVD). In MBE, beams of atomic or molecular species passing through ultra-high vacuum impinge on a single crystal substrate and in the right conditions crystal growth occurs epitaxially. Because of the fine control available in MBE, it is possible to grow specimens with any desired sequence of layer thicknesses and compositions. Also it is quite possible to prepare specimens in which each component is only a few monolayers thick. A review of MBE is given by Joyce (1985). Also Parker (1985) and Chang and

Ploog (1985) both include detailed chapters on MBE as well as on the physics of the resulting specimens. In MOCVD, growth occurs by deposition from a flowing vapour. Both MBE and MOCVD were used to produce specimens which were used in this work.

During the past twenty years it has been established that dispersive Fourier transform spectroscopy is a powerful technique for determining absolute values of the far infrared dielectric response functions of solids from simultaneous measurements of their amplitude and phase reflection spectra (Birch and Parker 1979).

In this work DFTS has been used to measure the far infrared amplitude and phase reflection spectra of a variety of epitaxial layers (including a GaAs/AlAs superlattice). The measurements are given along with the theoretically calculated spectra for these many layered structures. Calculated spectra were obtained by standard multilayer optics techniques.

The measurements have been done using Golay detectors having two different window materials (Diamond which has a flat response across the whole of the far infrared and Quartz which does not transmit above 250 cm^{-1}). Mylar was used as the beam splitter material with the thickness chosen to suit the spectral range of the window material. A black polyethylene filter was used to cut off any high frequency components above about 600 cm^{-1}.

The values plotted for the amplitude lie between zero and one, with the value of the amplitude reflectivity of one being equivalent to a perfect mirror. The experimentally measured phase ϕ is the difference between the phase response of the sample ϕ_s and the phase response of a perfect mirror π,

i.e $$\phi = \phi_s - \pi$$

is the function plotted in all the figures.

Figure (5.1) shows the interferogram obtained using a diamond window Golay detector with two identical mirrors in the arms of the interferometer, while figure (5.2) shows the interferogram obtained when one of the mirrors has been replaced with a superlattice sample. As can be seen in the wings of the interferogram, subsidiary interferograms (signatures) are present. These are due to multiple interference effects caused by the Golay cell window. This limits the resolution obtainable with this detector as the interference signatures do not ratio out between the reference and sample interferograms.

It has been found that a scan speed of around 400 Hz for the laser fringes gives the best signal to noise ratio when operating with a peak of around 250 cm^{-1}. The speed was reduced when the higher wavenumber regions were needed.

5.2- DFTS MEASUREMENTS OF BULK MODES ON AN EPITAXIAL LAYER OF CdTe :

An epitaxial layer of CdTe on a GaAs substrate was studied by reflection DFTS. The specimen consisted of an epitaxial layer of CdTe (of thickness ≈ 3μm) deposited by plasma MOCVD on a GaAs substrate of dimensions 15x5x0.5 mm^3. Theoretical curves were obtained by standard multilayer optics techniques. The calculation was performed on a 3 layer system, layer 1 being a vacuum. The calculated amplitude r and phase ϕ spectra are shown in figure(5.3).

The measurements have been done using a Golay detector fitted with a diamond window. A Mylar film of thickness 6.25 μm was used as a beam splitter. The amplitude and phase reflection spectra measured by DFTS are shown in figure(5.4).

The measured spectra are compared with the calculated spectra in figures (5.5) and (5.6). It can be seen that the measurements are in good agreement with the calculation, and they reveal both the CdTe and GaAs reststrahlen bands, which lie in well separated spectral regions. The measured response of the composite system is described very well by bulk values of the dielectric response functions of the two components.

It can be seen from figure (5.4) that at frequencies ($<140\ cm^{-1}$) below the reststrahlen band of CdTe,

both the film and the GaAs substrate are transparent. At higher frequencies also, above the CdTe reststrahlen region, the CdTe layer is transparent and behaves as a dielectric film.

The complex reflectivity of the specimen is not determined solely by the optical constants of the CdTe epitaxial layer. This can be understood by considering the interference between the beam reflected from the top of the CdTe layer and the infinite series of multiply reflected beams passing through the film, as shown in figure (5.7). We denote the complex amplitude of the externally reflected beam by r(e), and the resultant complex amplitude of the series of internally reflected beams by r(i), with the modulus and phase given by expressions of the form

$$\underline{r}(e) = r_o(e) \exp i\phi(e) \qquad (1)$$

It is sufficient to consider only the external reflection and the first internally reflected partial wave. The amplitude and phase reflection coefficient for a single surface bounded by media i and j are given by (Birch and Parker, 1979);

$$r_{ij}^2 = [(n_i^2-n_j^2+k_i^2-k_j^2)^2 + 4(n_jk_i-n_ik_j)^2]$$
$$[(n_i+n_j)^2 + (k_i+k_j)^2]^{-2} \qquad (2)$$

$$\tan\phi_{ij} = 2(n_jk_i-n_ik_j)\ (n_i^2-n_j^2+k_i^2-k_j^2)^{-1} \qquad (3)$$

and the complex factor for propagation through a dielectric medium is

$$a_i = \exp(-\alpha_i L/2) \exp(i\omega n_i L/c) \qquad (4)$$

where L is the layer thickness. The above equations allow estimates to be made of the amplitudes and phases of r(e) and r(i). The first order approximation of the overall reflectivity of the specimen may be taken as their sum;

$$r = r(e) + r(i) \qquad (5)$$

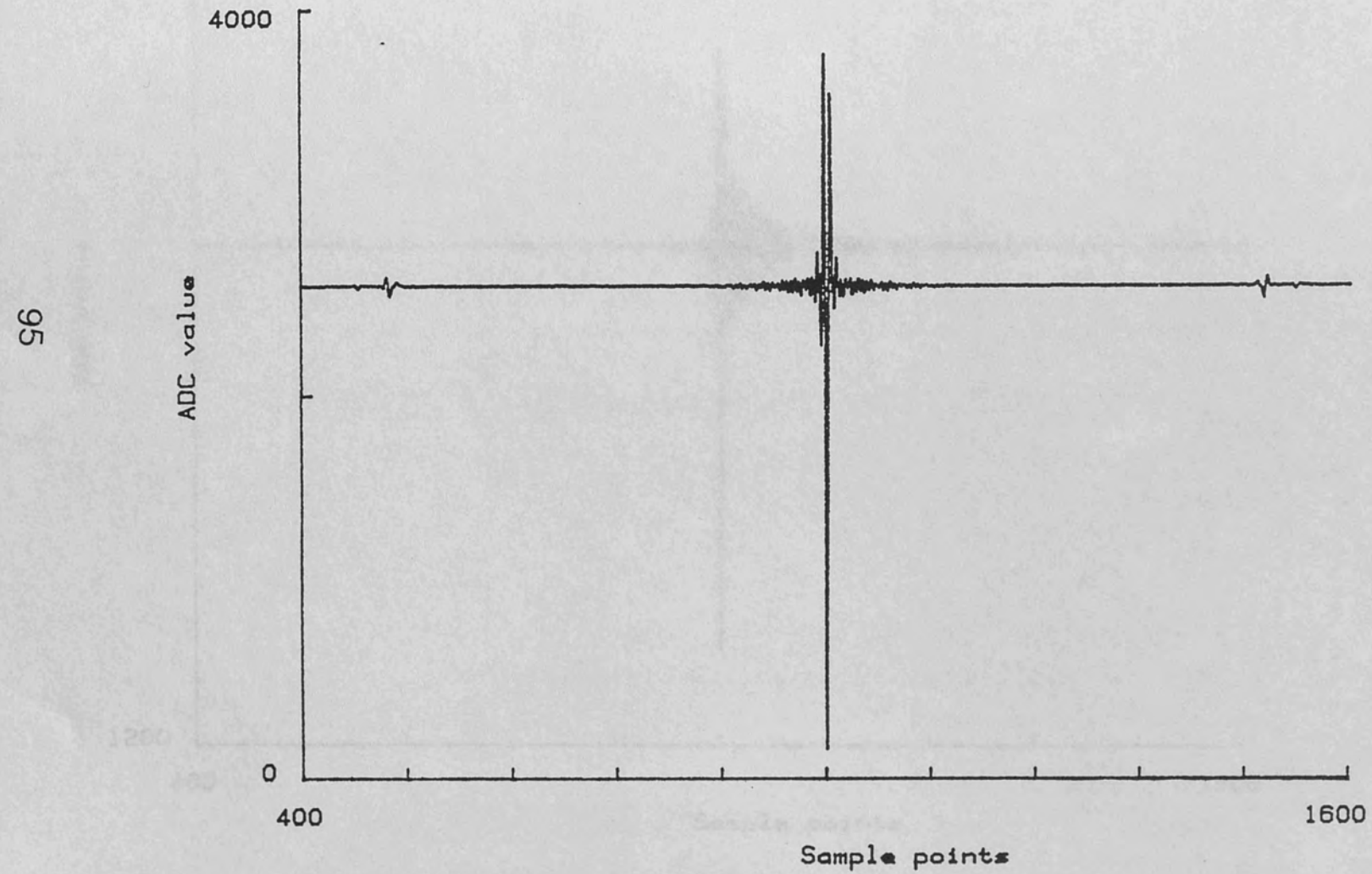

Fig(5.1): Reference interferogram obtained with two identical mirrors

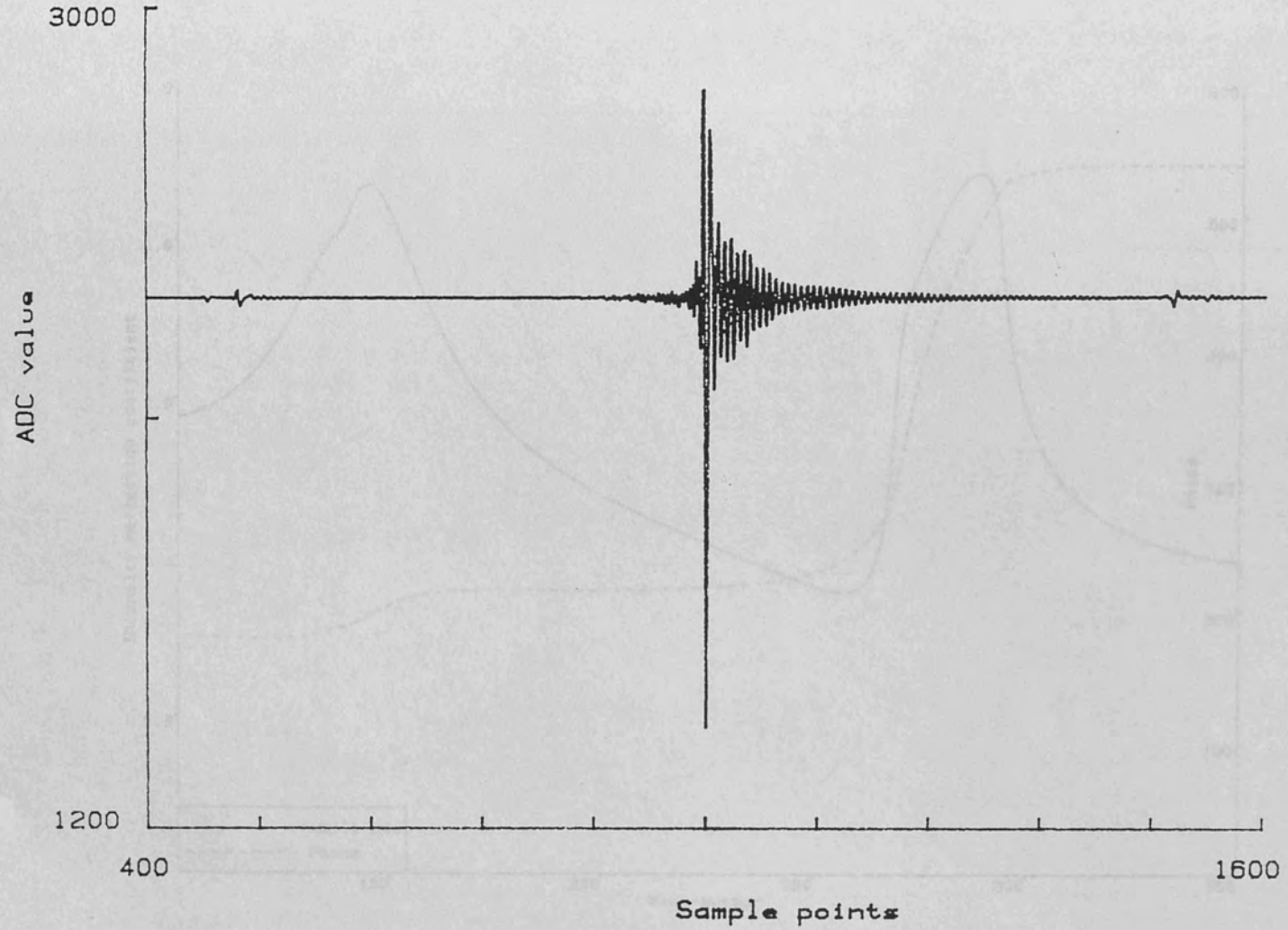

Fig. (5.2): Sample interferogram obtained with one of the mirrors replaced with a superlattice sample

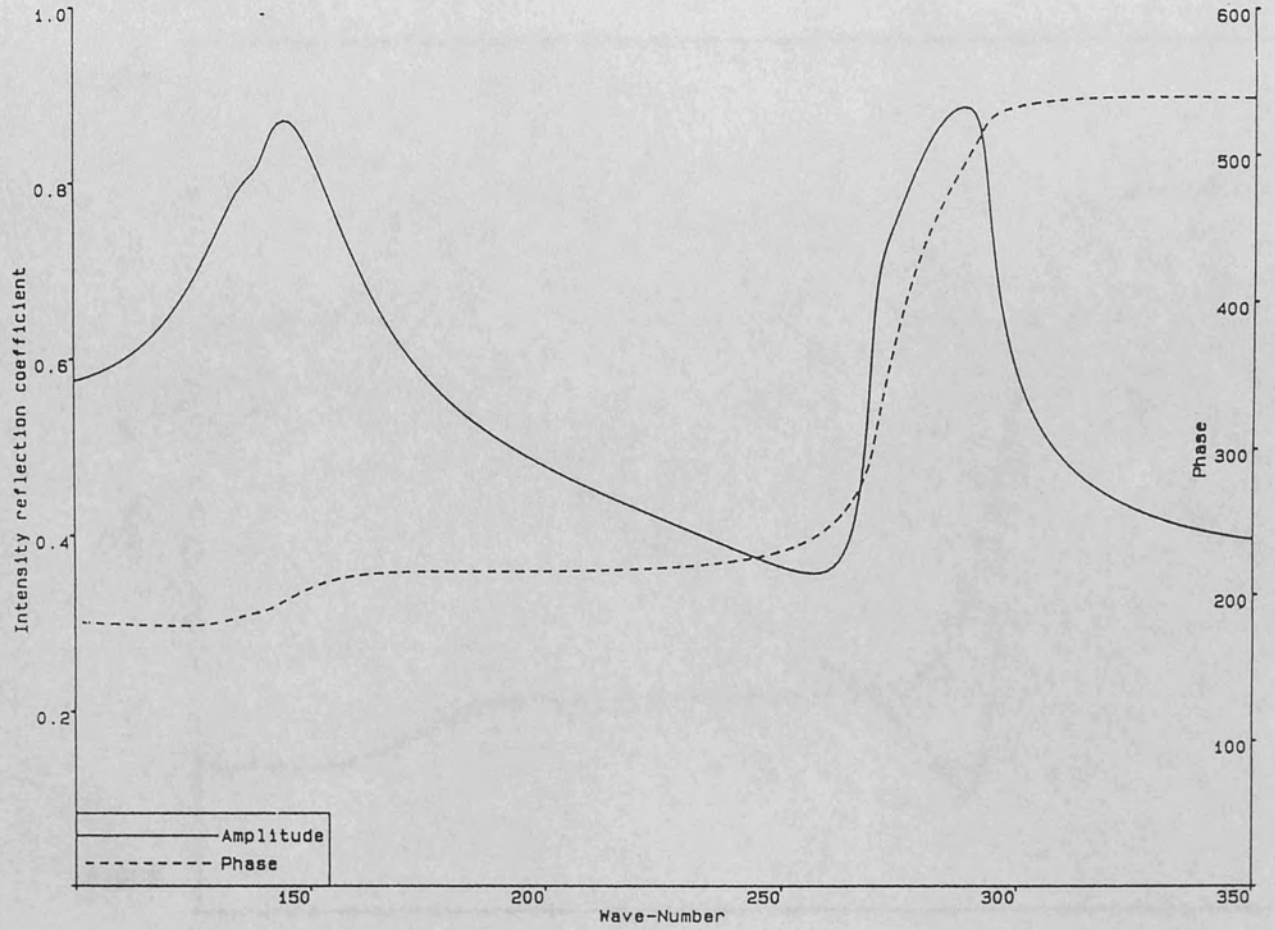

Fig. (5.3): The calculated amplitude and Phase for the CdTe epi-layer specimen

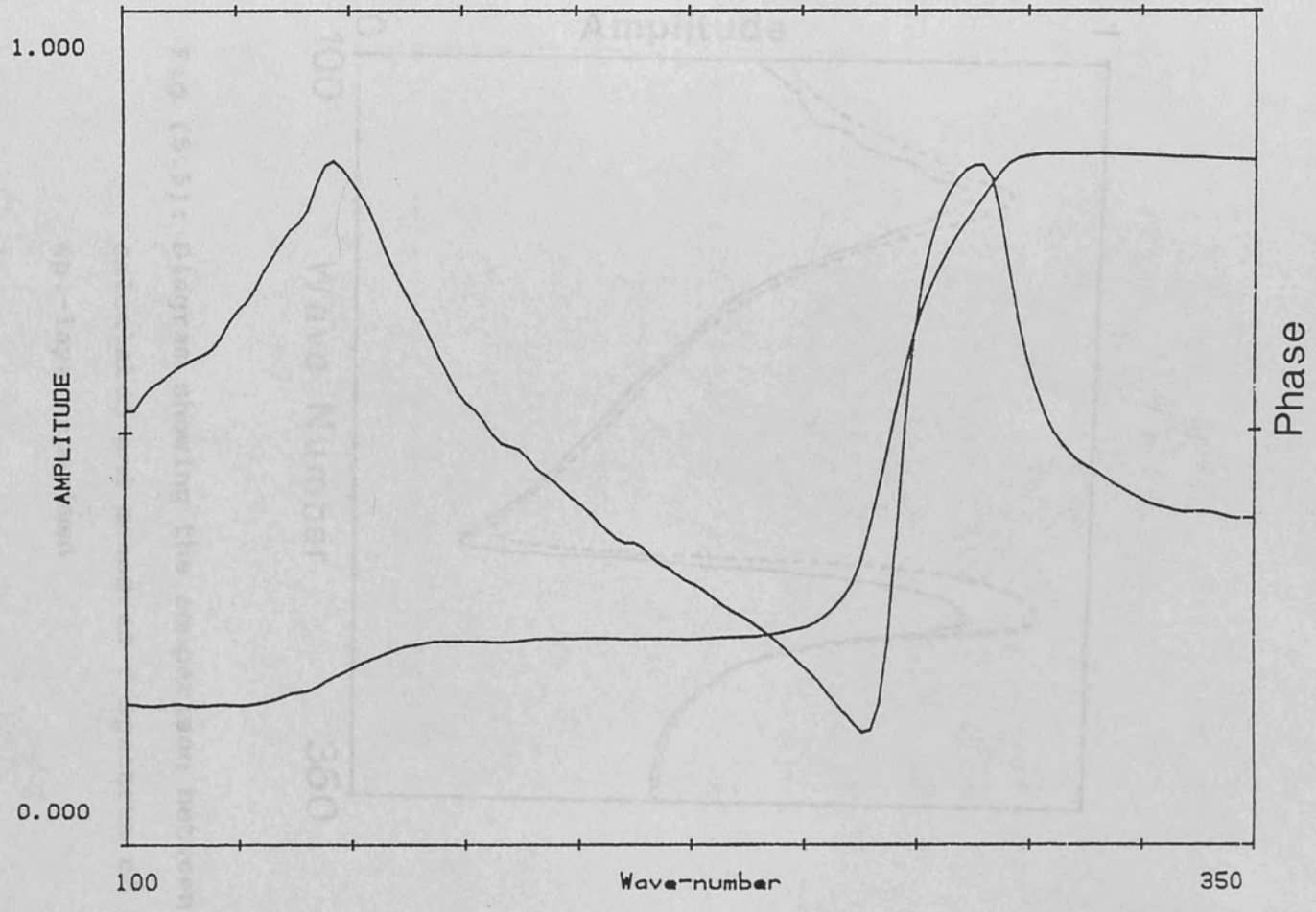

Fig(5.4): Complex amplitude r and phase ϕ of CdTe epi-layer specimen

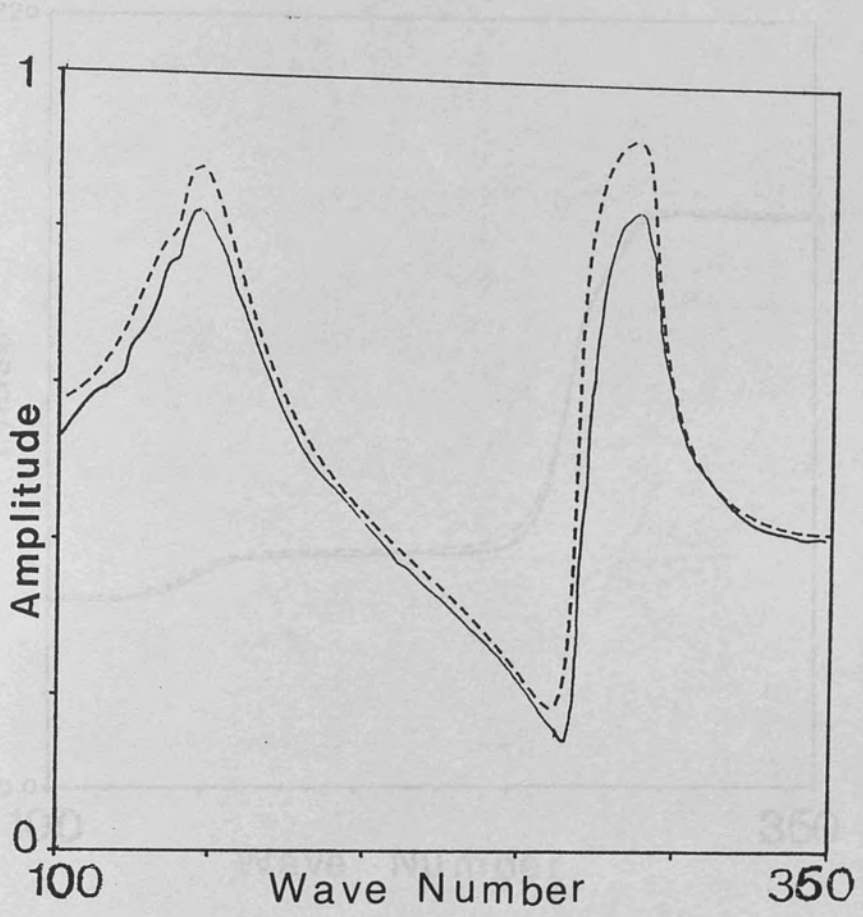

Fig (5.5): Diagram showing the comparison between the calculated and measured r spectrum of CdTe epi-layer specimen

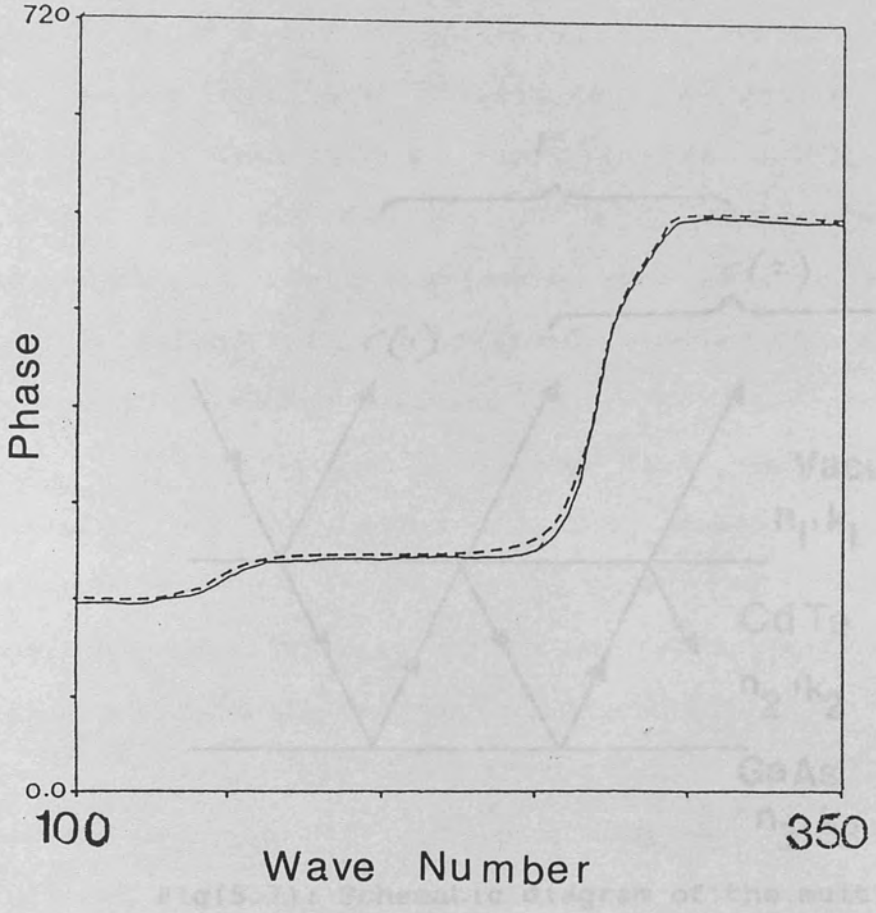

Fig (5.6): Diagram showing the comparison between the calculated and measured ϕ spectrum of CdTe epi-layer specimen

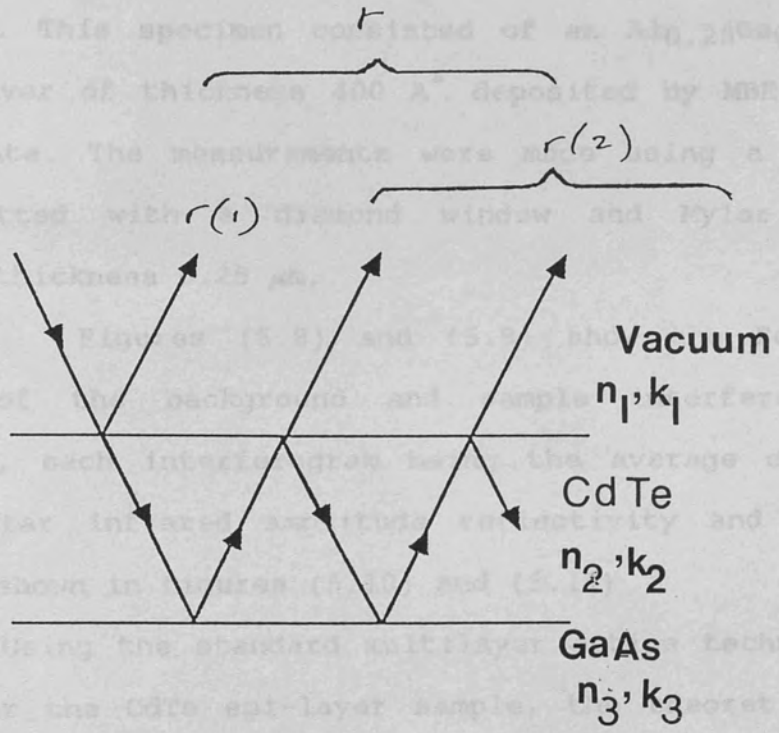

Fig(5.7): Schematic diagram of the multiply reflected beams in DFTS

5.3- DFTS MEASUREMENTS OF BULK MODES ON A $Al_{0.25}Ga_{0.75}As$ EPI-LAYER:

The amplitude and phase reflection spectra were measured by DFTS for an epitaxial layer of $Al_{0.25}Ga_{0.75}As$. This sample is made available by Philips Research Laboratories. This specimen consisted of an $Al_{0.25}Ga_{0.75}As$ epitaxial layer of thickness 400 A° deposited by MBE on a GaAs substrate. The measurements were made using a Golay detector fitted with a diamond window and Mylar beam splitter of thickness 6.25 μm.

Figures (5.8) and (5.9) show the Fourier transforms of the background and sample interferograms respectively, each interferogram being the average of 100 scans. The far infrared amplitude reflectivity and phase spectra are shown in figures (5.10) and (5.11)

Using the standard multilayer optics techniques described for the CdTe epi-layer sample, the theoretically calculated amplitude and phase reflectivity spectra shown in figure (5.12) have been obtained. Reststrahlen parameters for $Al_{0.25}Ga_{0.75}As$ were obtained by interpolating the data of Kim and Spitzer (1979). From figure (5.10), it can be seen that both the GaAs and AlAs reststrahlen bands, which lie in well separated spectral regions, are observed. Also figures (5.10), (5.11) and (5.12) show good agreement between measurement and calculation.

Figure (5.11) shows that below the reststrhalen band of GaAs both the epi-layer and substrate are transparent.

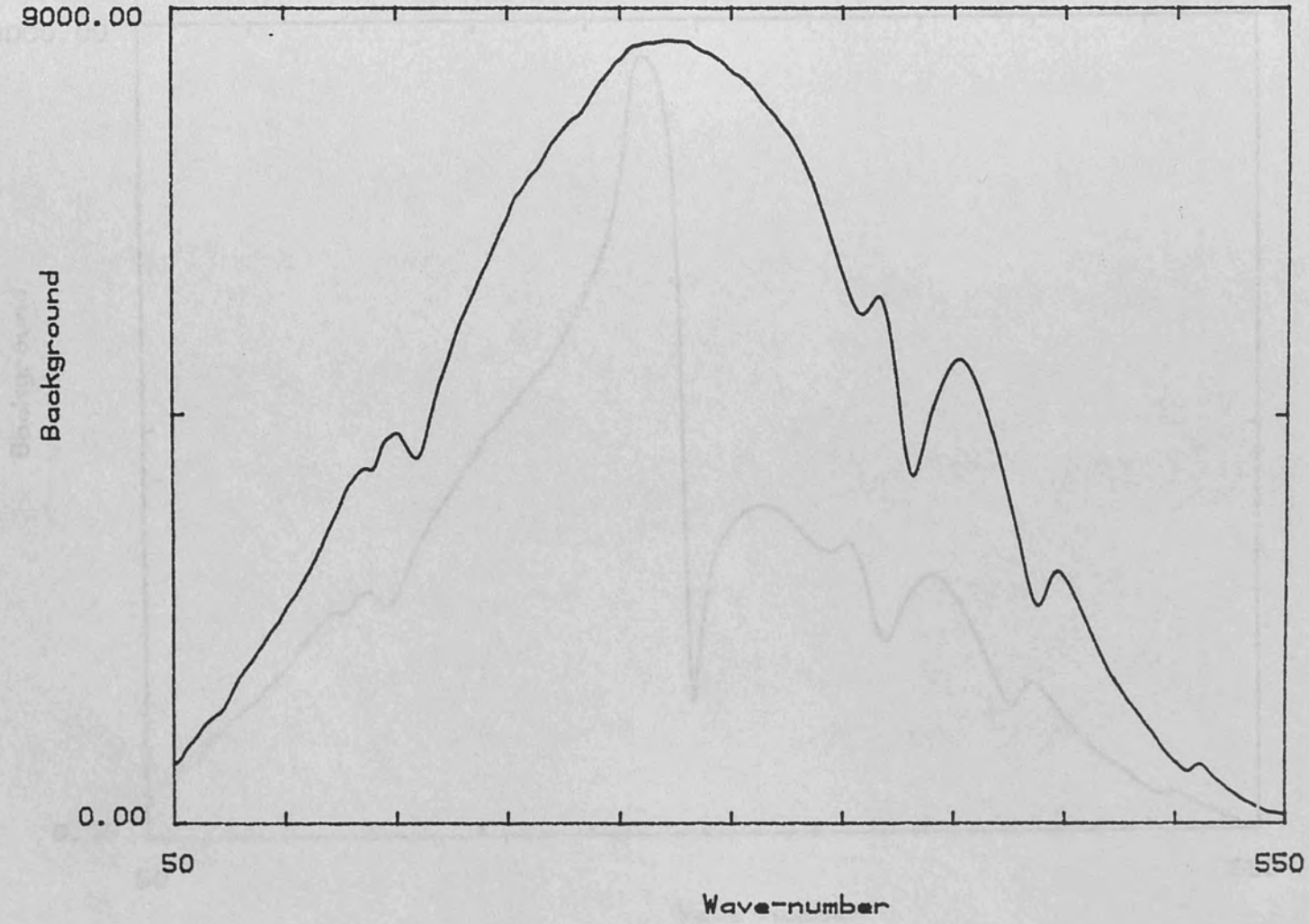

Fig(5.8): Fourier transform of reference interferogram obtained with two identical mirrors

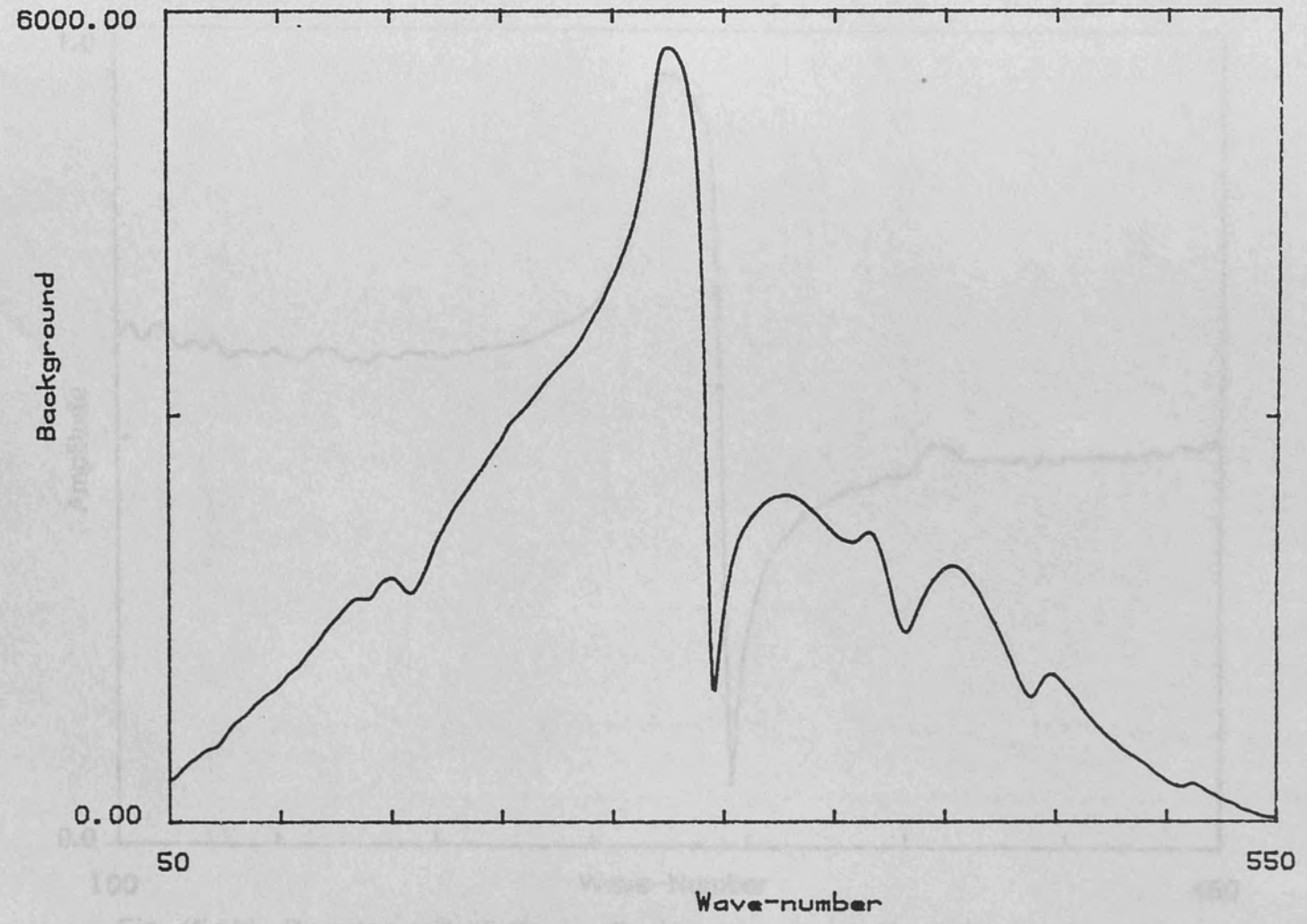

Fig(5.9): Fourier transform of $Al_{0.25}Ga_{0.75}As$ epi-layer interferogram

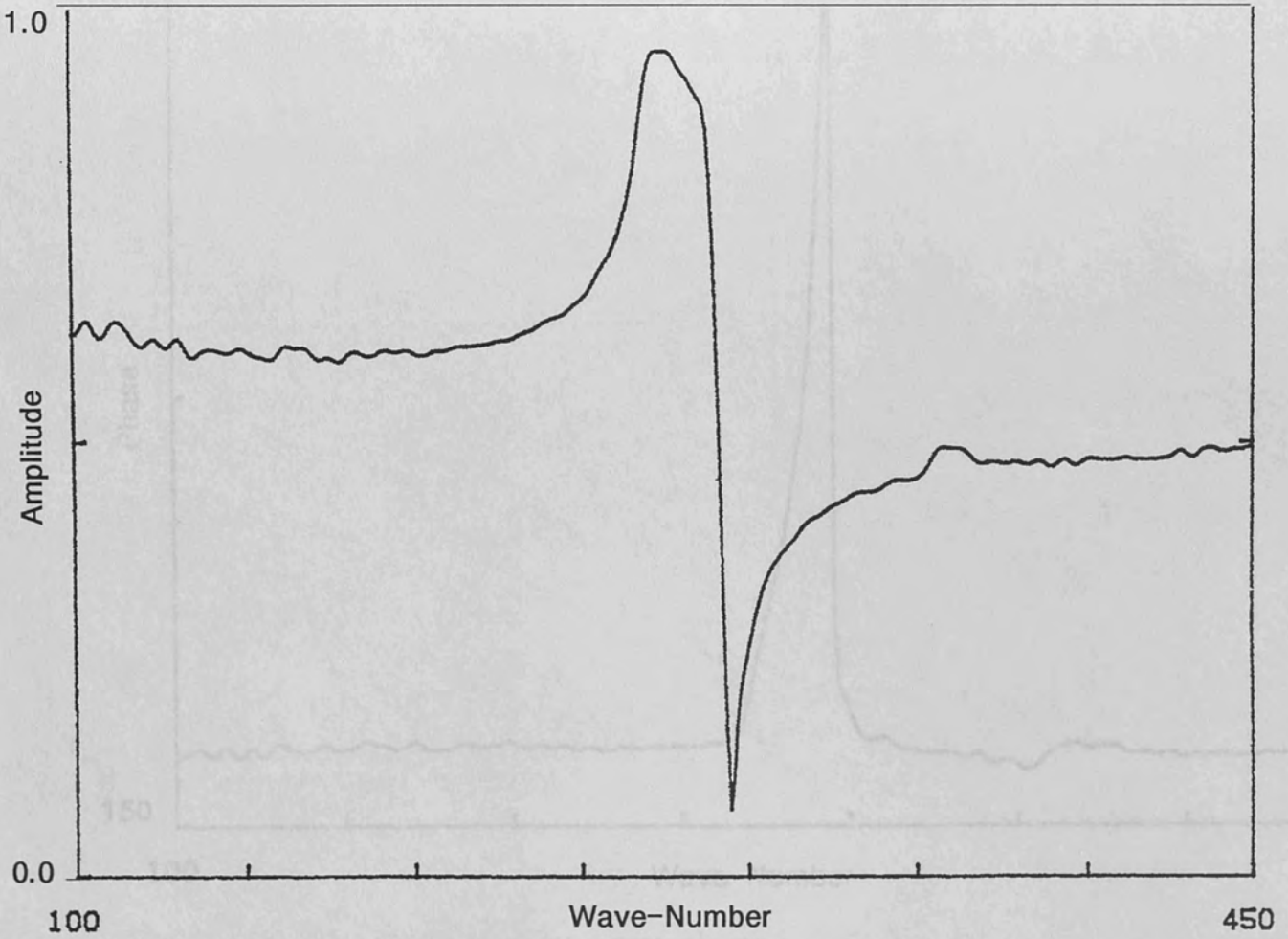

Fig. (5.10): Complex reflectivity amplitude spectrum of $Al_{0.25}Ga_{0.75}As$ epi-layer

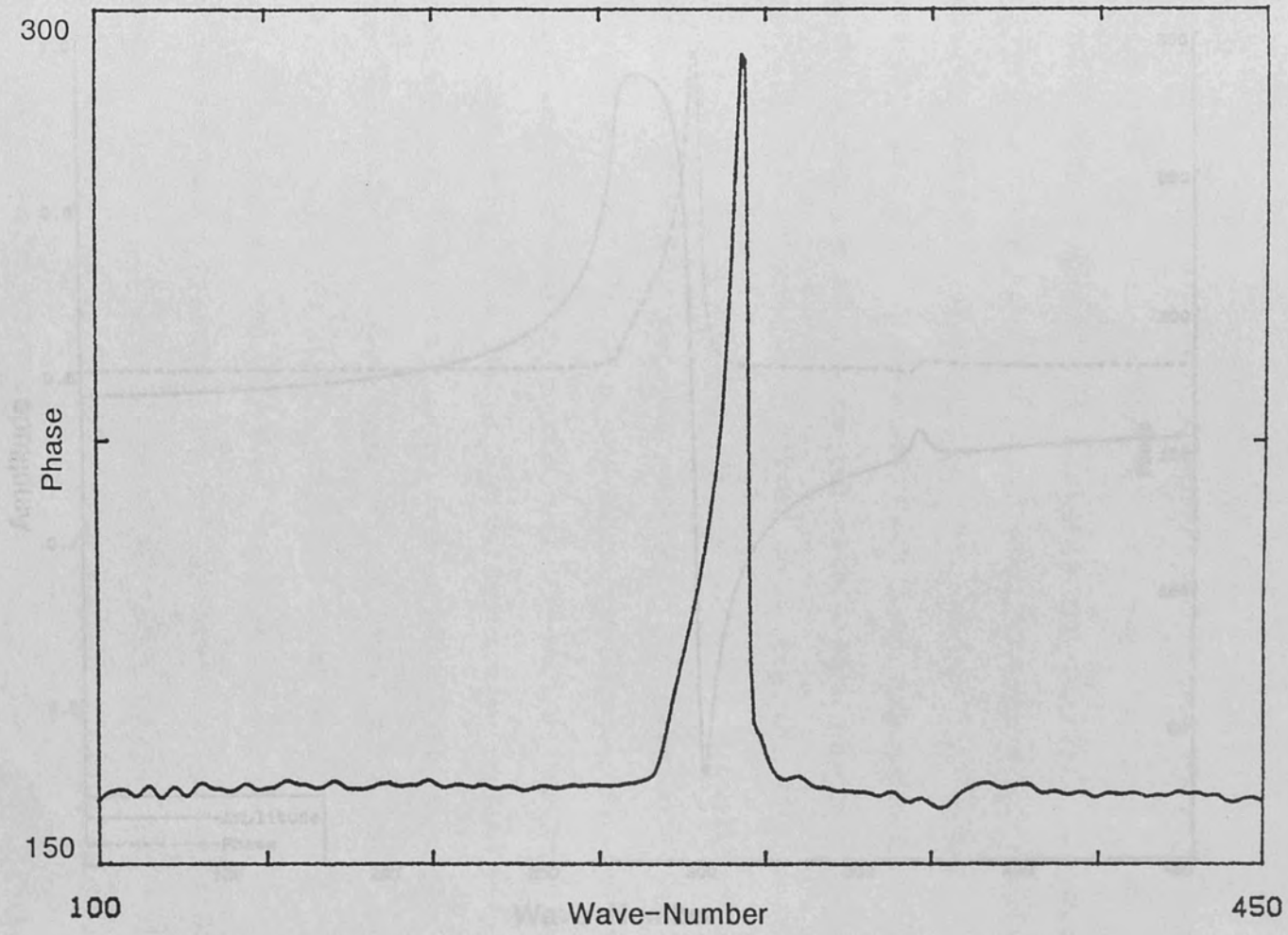

Fig. (5.11): Phase spectrum of $Al_{0.25}Ga_{0.75}As$ epi-layer

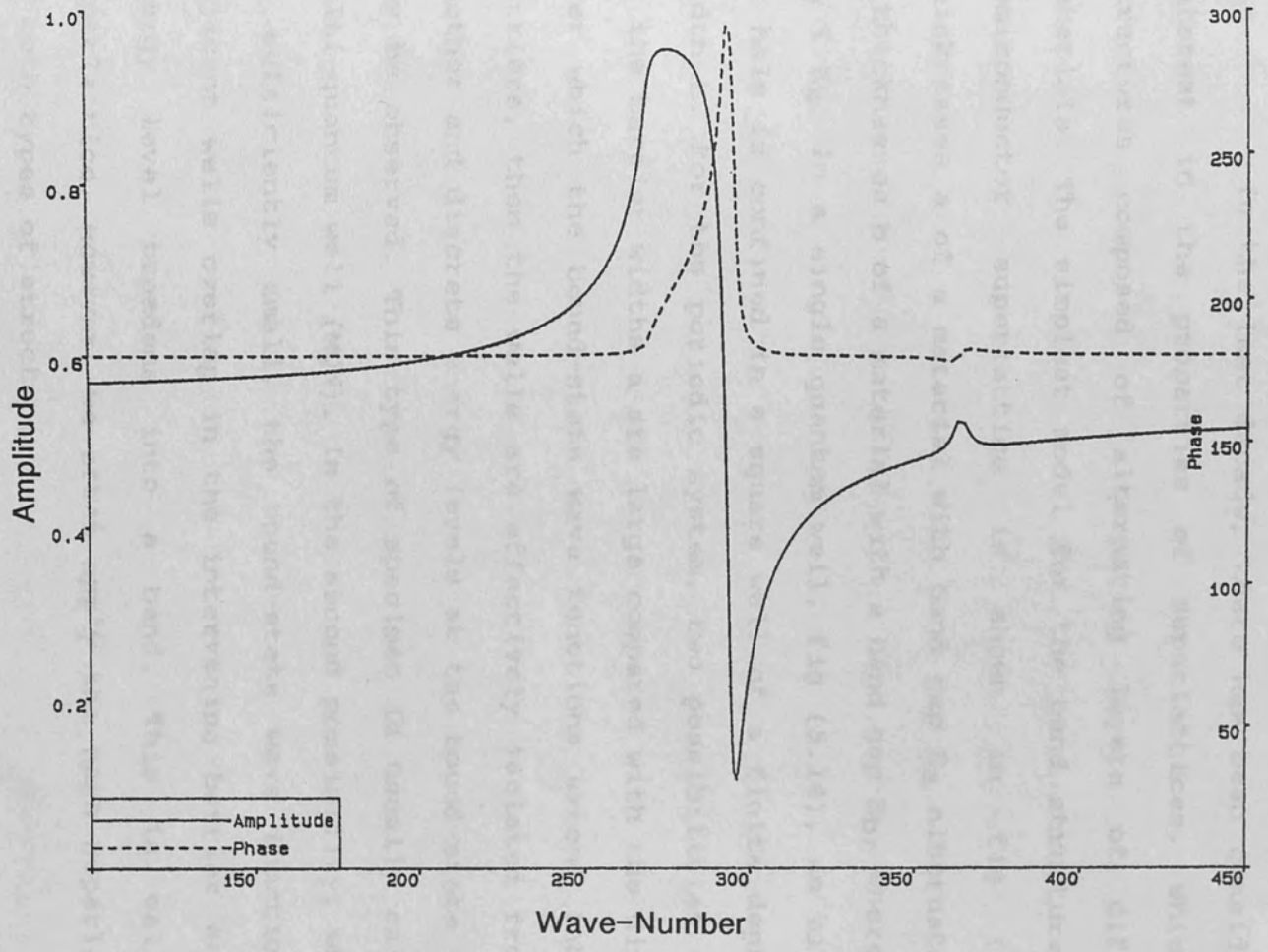

Fig. (5.12): Calculated amplitude and phase spectra of $Al_{0.25}Ga_{0.75}As$ epi-layer

5.4- DFTS MEASUREMENTS OF BULK MODES ON A SHORT PERIOD SUPERLATTICE:

In the last decade, there has been considerable interest in the properties of superlattices, which are structures composed of alternating layers of different materials. The simplest model for the band structure of a semiconductor superlattice is shown in fig (5.13). Thicknesses a of a material with band gap E_a alternate with a thicknesses b of a material with a band gap E_b, where $E_b < E_a$. In a single quantum well, fig (5.14), an electron or hole is confined in a square well of a finite depth and width b. For the periodic system, two possibilities arise. If the barrier widths a are large compared with the distance over which the bound-state wave functions extend into the barriers, then the wells are effectively isolated from one another and discrete energy levels at the bound-state values may be observed. This type of specimen is usually called a multi-quantum well (MQW). In the second possibility, where a is sufficiently small, the bound-state wave functions of adjacent wells overlap in the intervening barrier and the energy level broadens into a band. This is called a superlattice. However, we often apply the name superlattice to both types of structure.

In an MQW the far infrared optical properties are satisfactorily described by the bulk slab model, in which

each layer is assumed to have the dielectric function of the corresponding bulk material. This will be shown later in chapter (8). In this chapter we present the reflection amplitude and phase spectra of a short period superlattice specimen. This sample has been obtained from Philips Research Laboratories, and was grown by MBE. The sample is composed of 150 alternating layers of GaAs and AlAs, each 2 monolayers thick. Either side of the superlattice was a cladding layer 0.1 μm thick, composed of $Al_{0.7}Ga_{0.3}As$, and the complete structure was grown on a n-type GaAs substrate, with a carrier concentration of about 10^{18} cm^{-3}, approximately 400μm thick.

Using a Golay cell detector fitted with a diamond window and beam splitter of 6.25 μm thick Mylar, the amplitude and phase spectra are shown in figure (5.15). The measurements were made at a resolution of 4 cm^{-1}. Figure (5.16) shows the theoretical reflectivity spectrum obtained by Dumelow et al (1989) using data from the rigid ion model of Ren et al (1988). The relation between the reflectivity and amplitude is given by

$$R = |r|^2$$

From figures (5.15) and (5.16), it can be seen that the features observed in the far infrared amplitude spectrum are in reasonable agreement with those seen in the theoretical calculated reflectivity curve. In the measured amplitude spectrum feature 1 is due to a bulk plasmon in the

substrate. Features 2 and 3 arise from the reststrahlen bands of GaAs and AlAs respectively.

Below the plasmon frequency, the dielectric function of the substrate is negative which leads to high reflectivity. Measurements were made using a Golay cell detector fitted with a quartz window and a Mylar beam splitter of thickness 12.5μm. These measurements confirm the high reflectivity expected in this region, as shown in figure (5.17). More work is in progress on short period superlattices to improve the theoretical models.

5.5- REFERENCES:

J R Birch and T J Parker, Dispersive Fourier transform spectrometry, Chapter 3 in Infrared and Millimeter waves ,Ed. K J Button (Academic Press, New York, 1979).

L L Chang and K Ploog, Molecular Beam Epitaxy and Heterostructures (NATO/Martinus Nijhoff, Dordrecht) (1985)

T Dumelow, A R El-Gohary, K A Maslin, T J Parker, D R Tilley and S N Ershov, Semiconductor Science and Technology, in press, (1989).

B A Joyce Rep. Prog. Phys. 48, 1637, (1985).

E H C Parker ed., The Technology and Physics of Molecular Beam Epitaxy (Plenum, New York), (1985).

S F Ren, H Chu and Y C Chang, Phys. Rev., B 37, 8899 (1988).

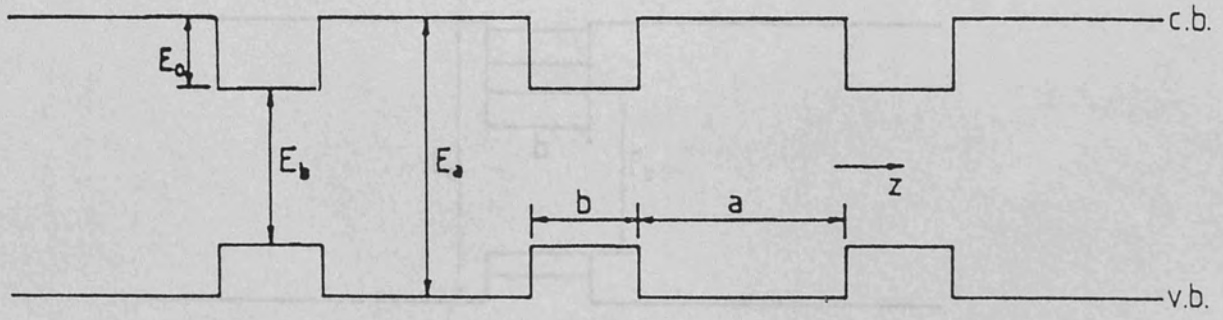

Fig(5.13): Diagram showing the simplest model for the band structure of a semiconductor superlattice

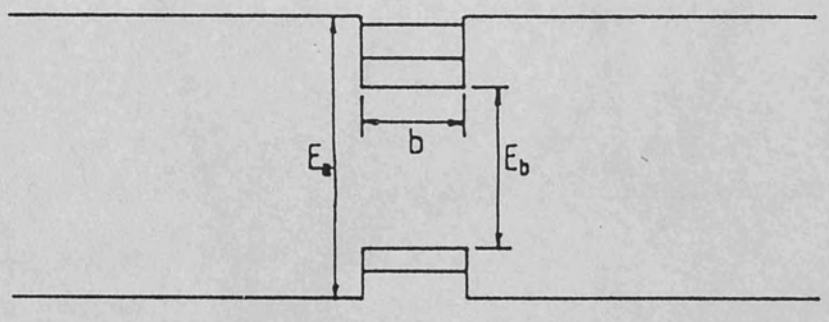

Fig (5.14): Diagram showing a single quantum well

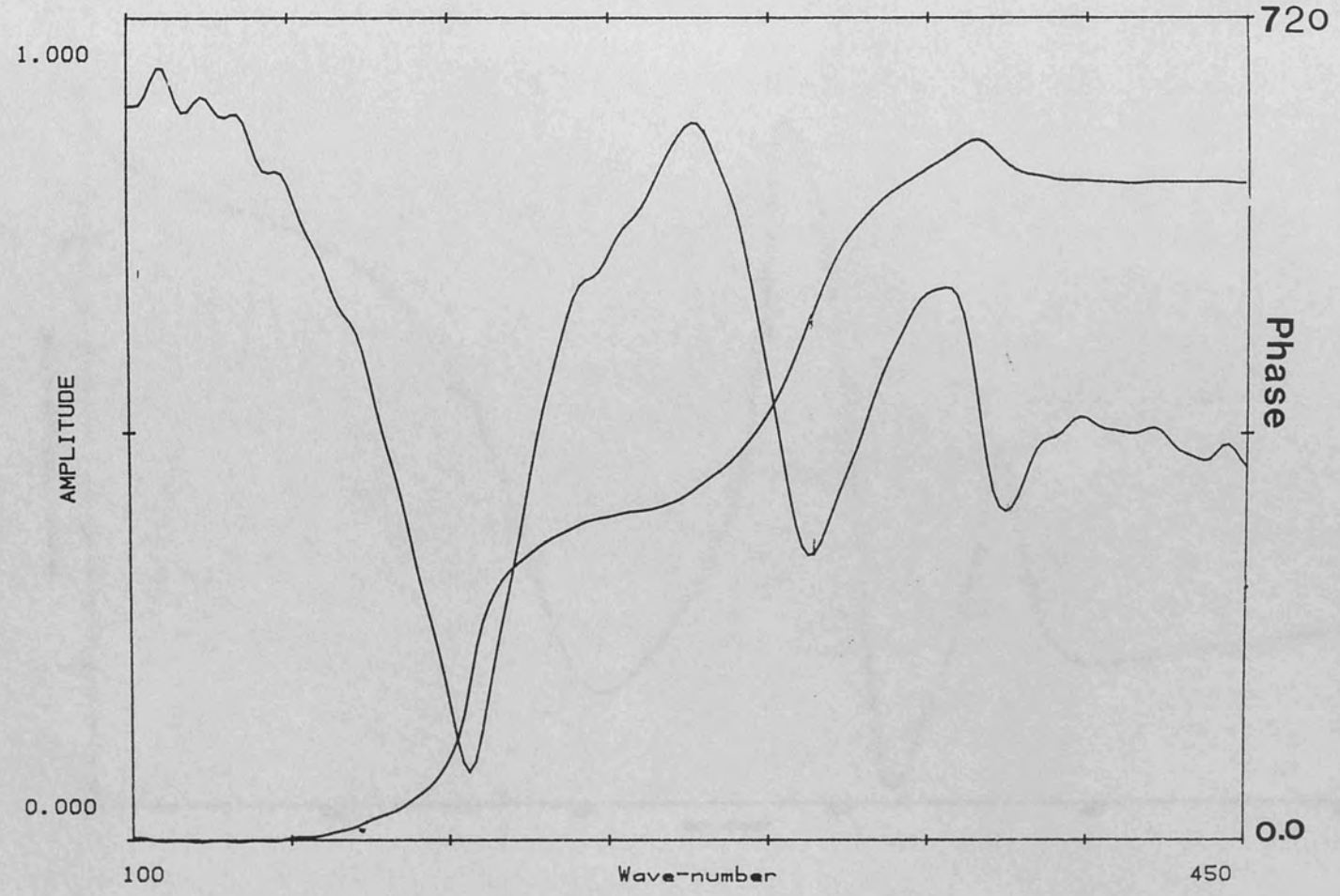

Fig (5.15): Far infrared amplitude and phase spectra of GaAs/AlAs superlattice

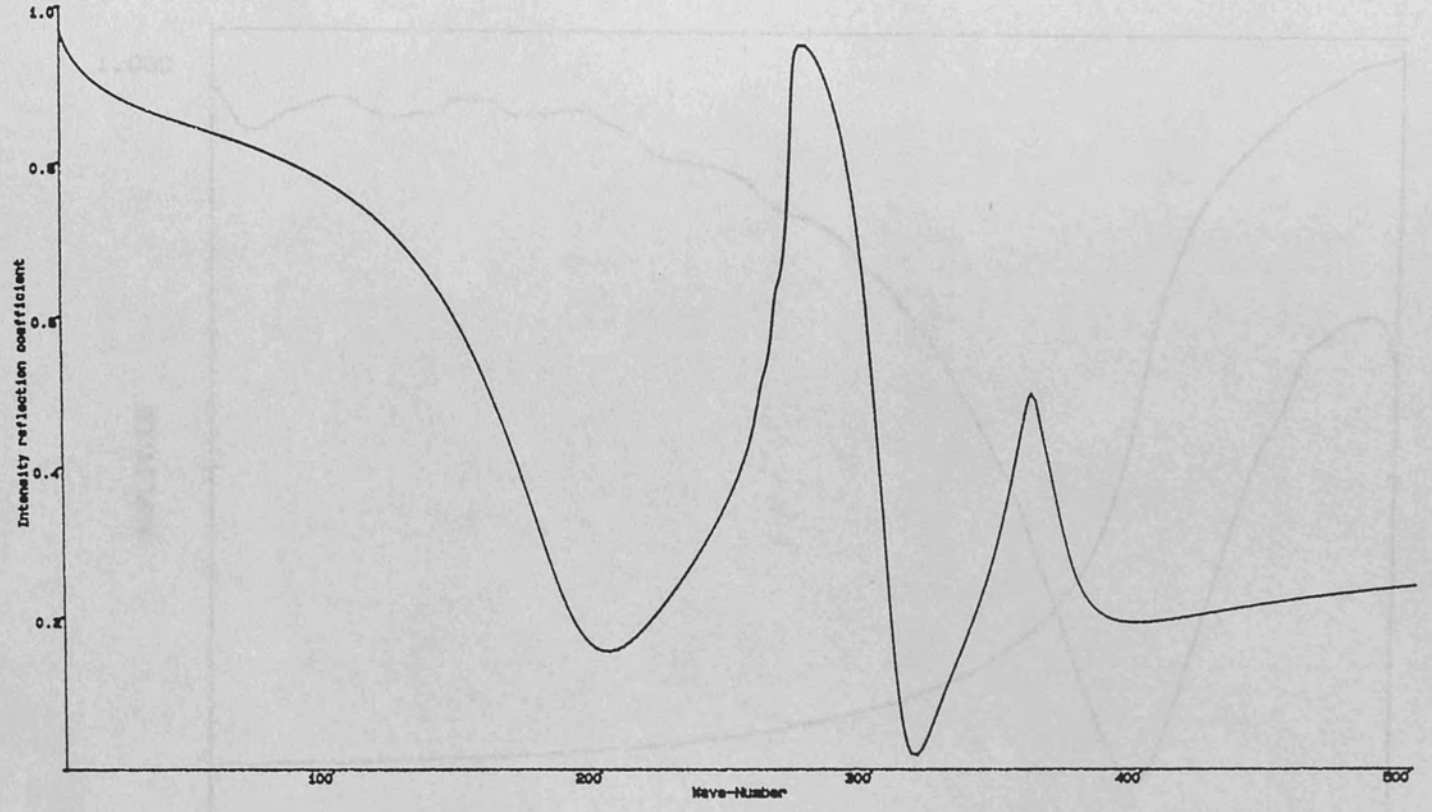

Fig. (5.16): The theoretical reflectivity spectrum of GaAs/AlAs superlattice

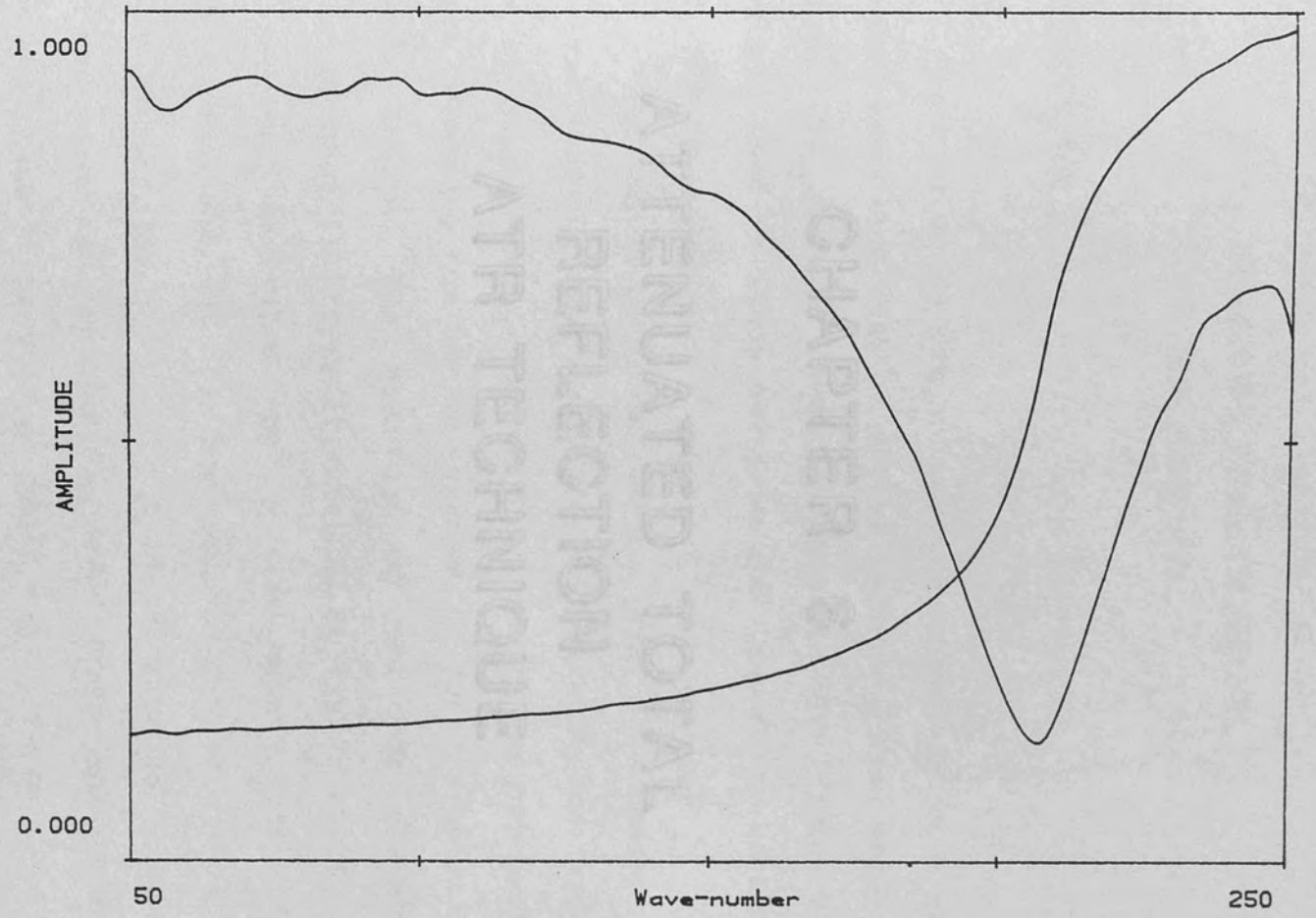

Fig(5.17): The amplitude and phase spectra of GaAs/AlAs superlattice using a Golay detector fitted with a quartz window

CHAPTER 6

ATTENUATED TOTAL REFLECTION ATR TECHNIQUE

CHAPTER (6)

ATTENUATED TOTAL REFLECTION

ATR TECHNIQUE

6.1- INTRODUCTION :

Fourier transform infrared spectroscopy is a well established technique that is widely used as a bulk analysis technique. In recent years, however, FTS has been increasingly used to study surfaces and thin films to solve surface related problems.

Attenuated total reflection (ATR) spectroscopy is a technique that is used to study surface characteristics. The ATR technique first used by Otto (1968) has become the principal technique for the measurement of surface polariton dispersion curves. The geometry of the ATR technique suggested by Otto (1968) is illustrated in figure (6.1). The upper medium, described by a frequency independent dielectric constant ϵ_1, is the prism, and medium 2 is typically an air gap with $\epsilon_2 = 1$ which acts as a spacer between the prism and the specimen under study. The incident beam in the prism propagates at angle θ with respect to the normal. If the refractive index of the prism is greater than the refractive index of the gap medium, $\epsilon_1 > \epsilon_2$, then for θ greater than the critical angle, when the incident beam

reaches the interface between the prism and the air gap it will normally be 100 % specularly reflected. In other words, the light wave incident from the prism onto the vacuum will be totally reflected at the bottom surface if

$$n_p \sin\theta > 1.$$

Thus, total internal reflection will occur if;

$$n_p^{-1} < \sin\theta < 1.$$

The wave vector K_χ of the incident light within the prism is

$$K_x = \omega n_p / c$$

and its component k_{xx} parallel to the lower surface of the prism is

$$k_{xx} = \omega n_p \sin\theta/c$$

In the vacuum below the lower prism surface, the electric field will decay as exp $(-\alpha d)$, with d measured perpendicular to the surface and

$$\alpha = \omega (n_p^2 \sin^2\theta - 1)^{1/2} / c$$

Thus we have an evanescent wave in the vacuum propagating parallel to the surface with $k_{xx} > \omega/c$. This evanescent wave can couple to nonradiative surface excitations. When the frequency and angle of incidence are such that a surface polariton is generated on the specimen, some of the energy

of the incident beam is transfered to the surface polariton, and the reflection coefficient drops strongly.

For the ATR curves the reflection coefficient may be investigated in two ways. First if we fix the frequency of the incident wave to be near the frequency for the surface polariton, we may adjust the parallel wave vector by changing the angle θ. Thus if one plots the reflection coefficient versus angle, and a sharp dip is found, this indicates the excitation of a surface polariton. Bulk polaritons may also be detected, although these usually appear as broad dips (Camley and Mills, 1982). Second, there is a frequency scan with a fixed angle. Previous theoretical and numerical work shows that it is necessary to perform this scan with θ not much greater than the critical angle θ_c of the prism because the optimum gap decreases as the angle of incidence increases. For angles much greater than θ_c the gap required for useful coupling is probably less than the surface irregularity on a typical specimen. Choice of the optimum gap is an important part of the experimental design. If the thickness of the air gap, d, is too small then the system is overcoupled and the properties of the isolated 2-3 interface will not be observed. If d is too large the system is undercoupled and the 2-3 interface mode is only weakly excited so that only a small reflectivity dip will be seen.

6.2- ANALYSIS OF ATR EXPERIMENTS :

Otto (1974) first writes the general expression for the reflectance R of P-polarised light incident within the prism. The dielectric function for the prism is taken to be the real quantity $\epsilon_1 = n_p^2$, with a gap of width d, and $\epsilon_2 = 1$. The dielectric function of the sample is given by the complex quantity

$$\epsilon(\omega) = \epsilon'(\omega) + i\,\epsilon''(\omega). \qquad (6.1)$$

The component of the wave vector parallel to the sample surface is

$$k_{xx} = n_p \left(\omega / c \right) \sin\theta \qquad (6.2)$$

and the reflectance is given by

$$R = | N r_{pv} / D |^2 \qquad (6.3)$$

where;

$$N = (\epsilon\alpha_v + \alpha) + r^{-1}_{pv}(\epsilon\alpha_v - \alpha) \exp(-2\alpha_v d) \qquad (6.4)$$

and;

$$D = (\epsilon\alpha_v + \alpha) - r^{-1}_{pv}(\epsilon\alpha_v - \alpha) \exp(-2\alpha_v d). \qquad (6.5)$$

r_{pv} is the reflection coefficient at the prism-vacuum interface and is given by

$$r_{pv}(\omega,k) = B_p - i\epsilon_p\alpha_v / B_p + i\epsilon_p\alpha_v \qquad (6.6)$$

while

$$\alpha_v = (k^2 - \omega^2/c^2)^{1/2} \qquad (6.7)$$

$$\alpha = (k^2 - \epsilon\omega^2/c^2)^{1/2} \qquad (6.8)$$

and;

$$\beta_p = (\epsilon_p\omega^2/c^2 - k^2)^{1/2}. \qquad (6.9)$$

This expression is valid if,

$$n_p \sin \theta > 1 \qquad (6.10)$$

that is, the prism-vacuum interface is totally reflecting (R=1) if the sample is absent.

The ratio of the electric field amplitude at the sample-vacuum interface to the electric field amplitude of the incident wave is found to contain the quantity D, given by (6.5). Setting D = 0 specifies the normal-mode condition which in this case is the dispersion relation of the surface optical wave including the perturbing effects of the prism. If the prism is removed by letting $d \to \infty$, one gets the expression

$$\epsilon \alpha_v + \alpha = 0 \qquad (6.11)$$

which yields the unperturbed surface optical wave dispersion relation. Equation (6.11) can also be written

$$k = (\omega/c) (\epsilon/\epsilon+1)^{1/2}. \qquad (6.12)$$

To treat the case in which θ is held fixed and ω (and k) is varied, the expression for R is expanded in terms of the quantity;

$$\delta\omega = \omega - \omega_o \tag{6.13}$$

noting that when ω is varied, the variation in k is given by

$$k = k_o + (k_o / \omega_o)\, \delta\omega \tag{6.14}$$

where k_o and ω_o are real quantities determined by the fixed angle θ:

$$k_o = (\omega_o / c)\, n_p \sin\theta. \tag{6.15}$$

By using equation (7.12) which gives the surface optical wave dispersion relation under the conditions that intrinsic damping and radiation damping are neglected

$$k_o = (\omega_o/c)\, [\epsilon'(\omega_o)/\epsilon'(\omega_o)+1]^{1/2} \tag{7.16}$$

the result is

$$R = 1 - \frac{4\, \omega_{ii}\, \omega_{ir}\, e^{-2\alpha_{od}}}{(\omega-\omega_{lo}-\omega_{rr}e^{-2\alpha v_o})^2+(\omega_{ii}+\omega_{ir}e^{-2\alpha v_o})^2} \tag{7.17}$$

where;

$$\omega_{rr} = h\mathrm{Re}\{r_{pv}(\omega_o, k_o)\}$$

$$\omega_{ir} = h\mathrm{Im}\{r_{pv}(\omega_o, k_o)\}$$

$$\omega_{ii} = -(\epsilon_{2o}/\epsilon'_{1o})$$

$$h = 4\epsilon_{1o} / (|\epsilon_{1o}| + 1)$$

$$\epsilon_{1o} = \epsilon'(\omega_o)$$

$$\epsilon'_{1o} = d\epsilon'/d\omega|_{\omega=\omega o}$$

and

$$\epsilon_{2o} = \epsilon'' (\omega_o).$$

The reflectance dip is centered at the shifted frequency

$$\omega = \omega_o + \omega_{rr} \exp [-2\alpha_{vo}d] \qquad (7.18)$$

and has the halfwidth

$$\omega_{ii} + \omega_{ir} \exp [-2\alpha_{vo}d] \qquad (7.19)$$

REFERENCES

R E Camley and D L Mills, Phys. Rev., B 26, 1280, 1982.

A Otto, Z. Phys. 216, 389, 1968.

A Otto, Festkorperprobleme (Advances in Solid State Phys) vol. XIV, ed. J Treush (Braunschweig: Vieweg), 1974.

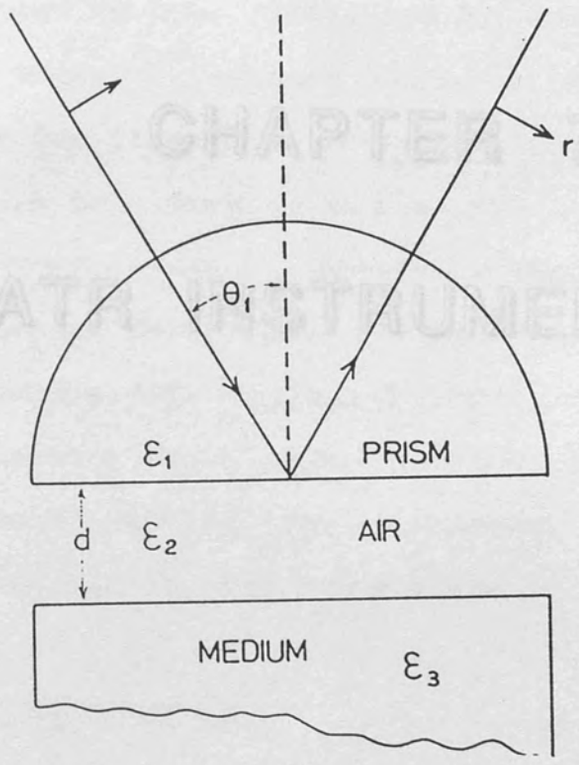

Fig (6.1): Diagram showing the geometry of the ATR technique suggested by Otto (1968)

CHAPTER 7

ATR INSTRUMENTATION

CHAPTER (7)

ATR INSTRUMENTATION

7.1- INTRODUCTION :

The technique of attenuated total reflection (ATR) was introduced by Otto (1968) and by Raether and Kretschmann (1971) to observe surface phonon-polaritons, and it was applied for the first time by Bryksin et al (1971).

In this work we use an FTS spectrometer together with ATR spectroscopy to observe surface phonon-polaritons in a long period GaAs/$Al_xGa_{1-x}As$ multiple quantum well (MQW) structure and a CdTe epitaxial layer on a GaAs substrate. The measurements have been done in both directions of polarisation (P and S). The instrument allows measurements to be carried out at room temperature.

7.2- ATR INTERFEROMETER :

The apparatus and the experimental technique are based on an NPL/Grubb Parsons cube interferometer fitted with an ATR stage in the collimated beam at the output port of the interferometer. The instrument is mainly a power FTS interferometer which has been described in chapter (3). An ATR stage is inserted into the collimated beam at the output

port of the interferometer. A diagram of the ATR system is shown in figure (7.1). The collimated beam coming from the FTS interferometer is sent through a slit (A) adjusted to lie at the centre of the beam for two reasons. Firstly it is desirable to maximise the intensity of the collimated beam. Secondly, this limits the collimated beam to fit the prism surface area and to stop any reflection from the sample holder or from the interferometer sides.

7.3- THE PRISM :

The prism used in our experiment has been cut from a single crystal of silicon. The prism angle is equal to 20^{o} so that the beam incident normally on the surface of the prism has an incident angle of 20^{o} on the base of the prism. The dimensions and geometry of the silicon prism are shown in figure (7.2). We chose silicon because of its high refractive index ($n=3.413$), low absorption coefficient ($\alpha=1.0cm^{-1}$) and lack of dispersion in the far infrared.

7.4- INCIDENT ANGLE ADJUSTMENT :

A movable plane mirror has been used to adjust the incident beam to be normal to the surface of the prism as shown in figure (7.3). If coupling with the sample is neglected, the energy throughput through the prism can be

calculated from

$$I_c \propto [\ (1-R)e^{-\alpha d} - R(1-R)e^{-\alpha d}\ ]\ I_o$$

$$= [\ (1-R)(e^{-\alpha d} - Re^{-\alpha d})\ ]\ I_o$$

$$= [\ (1-R)^2\ e^{-\alpha d}\ ]\ I_o$$

where, I_c is the output beam intensity

I_o is the incident beam intensity

α is the absorption coefficient

R is the power reflectivity of the Si prism .

d is the path length through the prism

For silicon $n = 3.413$ and $\alpha = 1.0\ cm^{-1}$ which lead to;

$$R = |r|^2 = |n-1/n+1|^2 \approx 0.3$$

$$I_c = 0.025\ I_o$$

We used plane mirrors to avoid having more than one incident angle at the prism. Theoretical calculations by Raj & Tilley (1989)* show that if there are many angles of incidence, the surface-mode dips would be broadened.

7.5- AIR GAP ADJUSTMENT :

In our experiments the samples were separated from the surface of the silicon prism by a thin air gap of

* Personal communication.

approximately 10 μm to obtain optimum coupling (as predicted by the theoretical calculation). To adjust the air gap we used two mylar strips between the prism and the sample holder. Also we used a system of four screws or the sensitive micrometer system shown in fig (7.3) to change the air gap until a good spectrum was obtained.

7.6- THE OUTPUT OPTICS :

A combination of a plane mirror and a concave mirror is used to focus the transmitted beam from the prism onto the detector. In this system, the collimated beam is reflected off the optically flat mirror to the spherical mirror which condenses the beam to a focus some 10 to 15 cm away at the detector. Just in front of the focus there is room to place various filters. A free-standing wire grid wound from 5μm diameter tungsten wire has been used in front of the detector to polarise the output radiation. The polariser is not 100% efficient and this leads to weak cross-talk between the P and S polarised spectra as will be seen later.

7.7- THE FILTERS :

Both optical and electrical filters are used to clean-up the wanted signal so that the signal to noise

ratio (S/N) will be high enough to give an acceptable spectrum when the interferogram is transformed. Low frequency noise due to the high sensitivity of the liquid He cooled Ge detector to mechanical vibrations of the optical components in the interferometer was removed by connecting an electronic filter between the detector and the amplifier [which has been described before in chapter (3)]. This filter is a high pass filter with a corner frequency of 600 Hz.

We used black polyethylene to block the unwanted higher wavenumber region. The black polyethlene filter was placed just in front of the detector.

7.8- THE DETECTOR :

We have used two detectors, a Golay cell detector fitted with a diamond window and a liquid He cooled Ge bolometer detector. For a Golay cell the intrinsic response time (the speed with which the detector responds to changes in the incoming signal) is about 50ms. The Golay cell is sensitive throughout the whole infrared region. On the other hand the response time of a liquid He cooled Ge detector ($\approx 1\mu s$) is much faster than the Golay cell. Simultaneously the noise in the cooled detector is considerably reduced. It was found that the radiation beam was greatly attenuated by the ATR system as discussed later, so that, in some cases,

the use of a liquid He cooled Ge detector was very important to get an acceptable signal to noise ratio.

REFERENCES :

V V Bryksin, Yu M Gerbsteien and D N Mirlin, Fiz Tverd Tela, 13, 2125, 1971 (Sov. Phys. Solid State, 13, 1779, 1972.

E Kretschmann, Z Physik, 241, 313, 1971.

A Otto, Z Phys. 216, 398, 1968.

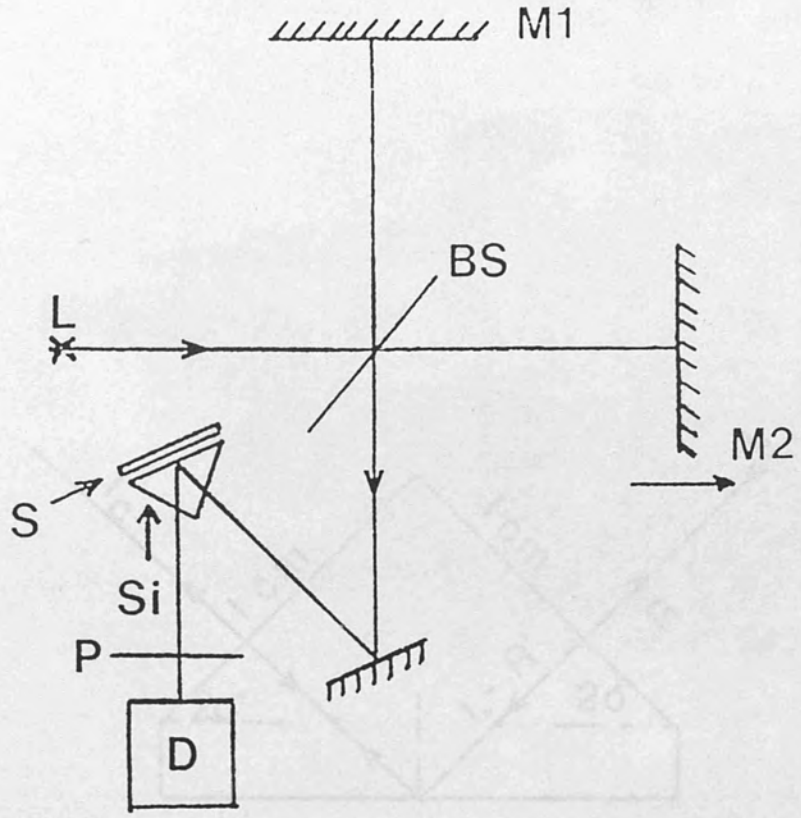

Fig (7.1): Schematic diagram showing the ATR stage used for this work.

M_1: fixed mirror, M_2: moving mirror,

L : Mercury lamp, P : polariser

SI: Silicon prism, D: detector

BS: Mylar beam splitter

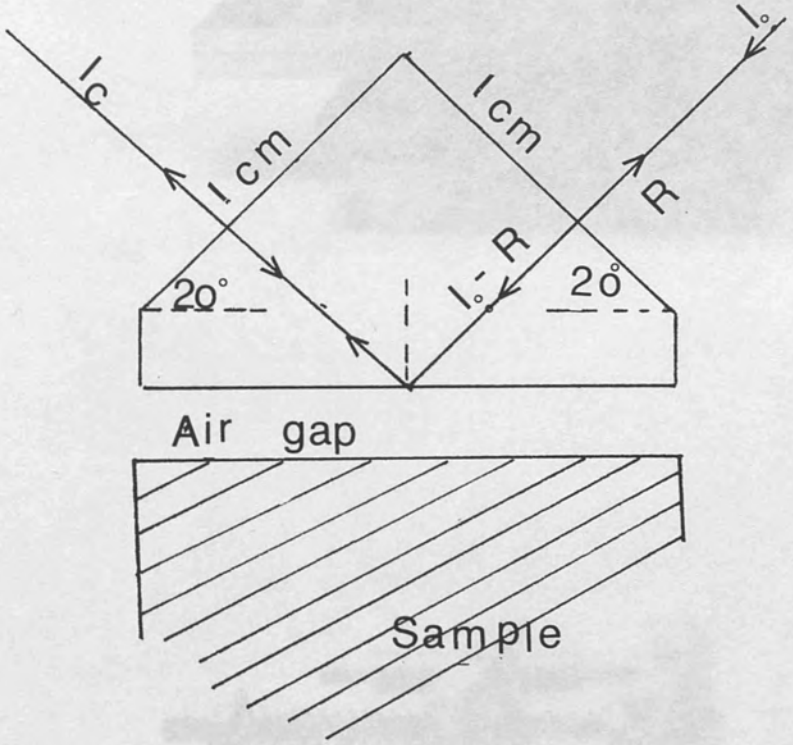

Fig. (7.2): Schematic diagram showing the dimensions and the geometry of the silicon prism used in the ATR stage.

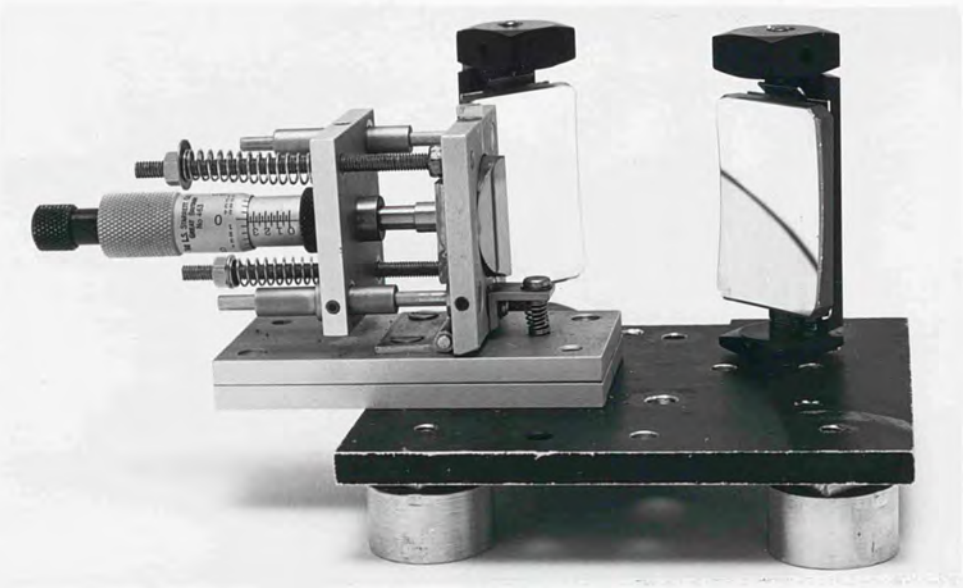

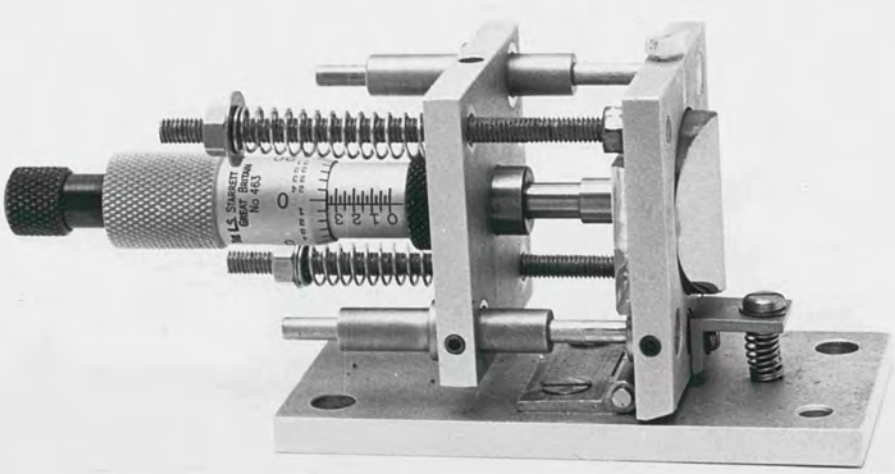
L.S. STARRETT
GREAT BRITAIN
No 463

CHAPTER 8

RESULTS AND DISCUSSION FOR ATR MEASUREMENTS

CHAPTER (8)

RESULTS AND DISCUSSION FOR ATR MEASUREMENTS

8-1 INTRODUCTION:

In recent years there have been many studies of the surface properties of superlattices which are structures composed of very thin alternating layers of different materials.

In the present work surface phonon-polaritons have been measured on two samples, a long period $GaAs/Al_xGa_{1-x}As$ multiple quantum well (MQW) and an epitaxial layer of CdTe, both on GaAs substrates. The measurements have been done in both P-polarisation (E in X-Z plane) and S-polarisation (E in the Y direction). A Golay detector fitted with a diamond window has been used to obtain the measurements of both the two samples. In the case of the MQW specimen, we also used a liquid He cooled Ge bolometer detector to measure the spectrum for P-polarised incident radiation near 280 cm^{-1} to ensure that all the features are real and reproducible. A Si prism has been used. The critical angle (θ_c) of the prism is given by

$$\sin \theta_c = 1 / n_p$$

$$= 1/\sqrt{\epsilon_p}$$

where $\epsilon_p = 11.65$

$$\theta_c = 17.04^\circ$$

Since the optimum air gap decreases as the angle of incidence increases, the angle of incidence θ should not be much greater than the critical angle. We have taken $\theta = 20^\circ$. The optimum air gap thickness with this angle is of the order of 10 μm (Raj and Tilley 1987). If the air gap is much smaller the system is overcoupled and the properties of the specimen surface polariton are highly perturbed by the proximity of the prism. Conversely, if it is larger, the coupling of the evanescent wave to the sample surface is weak and some dips are not brought out as clearly.

It was found that the radiation beam was greatly attenuated by the prism, because of the high reflectivity of silicon (refractive index of silicon is 3.413) and the long path length (≈3cm) in the prism. To minimise further energy losses, the radiation was polarised using a free_standing wire grid wound from 5 μm diameter tungsten wire which was placed in front of the detector. A black polyethylene filter together with the scan speed were used to filter out any high frequency components. It has been found that a scan speed of around 400 Hz for the laser fringes gives the best signal_to_noise ratio with a Golay detector. The corresponding frequency was found to be around 7000 Hz for

the bolometer detector.

Mylar was used as the beam splitter material, with different thicknesses used to suit different spectral ranges, as discussed in chapter(3).

The measurements were made at a resolution of $4cm^{-1}$ with the Golay detector, and a resolution of $1cm^{-1}$ with the bolometer detector.

8_2 ATR MEASUREMENTS FOR THE MQW :

In recent work Raj, Camley and Tilley (1987) describe the theoretical calculation of attenuated total reflection (ATR) spectra of semiconductor superlattices in the reststrahl frequency region. They derived the theoretical spectra by treating the multiple quantum well (MQW) structure as an effective uniaxial dielectric bulk medium. The parameters which have been used to calculate the theoretical ATR spectra were obtained from previous experimental measurements on the same sample (Maslin et al 1986).

The work described here includes the first observation of surface phonon_polaritons on an MQW. This sample is made available by Philips Research Laboratories. The dimensions of the MQW are shown in fig (8.1). The structure consists of 60 periods, each period composed of 55 A^{o} of GaAs and 170 A^{o} of $Al_{0.35}$ $Ga_{0.65}$ As, with 0.1 μm of $Al_{0.35}Ga_{0.65}As$ cladding on each side and a top layer of 200 A^{o} of GaAs. This is grown on a GaAs substrate of about 400 μm thickness. As can be seen, the total thickness of the multilayered structure is only about 1.4 μm, compared to over 400 μm for the bulk medium.

The far infrared ATR spectra for the geometry shown

in fig (8.2) have been calculated within the model described by Otto (1974), Agranovich et al (1982), and Boardman (1982). Because of the number of layers a matrix formulation has been used. We take the Z axis normal to the layers with interface positions at:

$$z_{12} = 0$$

$$z_{23} = -d_1$$

$$z_{34} = -(d_1+d_2)$$

$$z_{45} = -(d_1+d_2+d_3)$$

$$z_{56} = -(d_1+d_2+d_3+d_4)$$

The Y axis is taken transverse to the plane of incidence. Consider p-polarised light inside the prism incident at an angle. The non-vanishing components of the electromagnetic field are E_x, E_z and H_y. It is convenient to work with the Y-component of magnetic field H_{ny} because the other components are zero. H_{ny} in medium n can be written in two alternative forms;

$$H_{ny} = h_{nl} \exp [-ik_{nz}(z-z_{n,n+1})] + g_{nl} \exp [ik_{nz}(z-z_{n,n+1})] \qquad (8\text{-}1)$$

or

$$H_{ny} = h_{nu} \exp [-ik_{nz}(z-z_{n-1,n})] + g_{nu} \exp [ik_{nz}(z-z_{n-1,n})] \qquad (8\text{-}2)$$

for n=0 to n=5.

h_{n1} and h_{nu} are the complex amplitudes of the wave travelling in the negative Z-direction in medium n.

g_{n1} and g_{nu} are the complex amplitudes of the wave travelling in the positive Z-direction in medium n.

In equations (8-1) and (8-2) we have dropped explicit dependence on the common factor $\exp[i(k_x x - \omega t)$. The alternative amplitudes are related by:

$$\begin{Bmatrix} h_{nu} \\ g_{nu} \end{Bmatrix} = \begin{Bmatrix} \exp(-ik_{nz}d_z) & 0 \\ 0 & \exp(ik_{nz}d_z) \end{Bmatrix} \begin{Bmatrix} h_{n1} \\ g_{n1} \end{Bmatrix} = F_n \begin{Bmatrix} h_{n1} \\ g_{n1} \end{Bmatrix} \qquad (8\text{-}3)$$

The k_{nz}'s are defined as:

$$k_{nz} = [(\omega^2/c^2)\ \epsilon_n - k_x^2]^{1/2} \qquad n=3 \qquad (8\text{-}4)$$

and

$$k_{3z} = [(\omega^2/c^2)\epsilon_{xx} - (\epsilon_{xx}/\epsilon_{zz})k_x^2]^{1/2} \qquad (8\text{-}5)$$

where k_x in the prism is

$$k_x = (\omega/c)\ \epsilon_p^{1/2}\ \sin\theta \qquad (8\text{-}6)$$

Since the parallel component of the wavevector k_x must be continuous at an interface equation (8-6) applies in all media. $\epsilon_{nx} = \epsilon_{nz}$ for all media except the superlattice, in which case $\epsilon_{nx} = \epsilon_{xx}$, $\epsilon_{nz} = \epsilon_{zz}$ and also $\epsilon_{ox} = \epsilon_{oz} = \epsilon_p$.

The tangential component of the electric field is derived from Maxwell's equation and standard boundary conditions at each interface yield:

$$\begin{Bmatrix} h_{n1} \\ g_{n1} \end{Bmatrix} = \begin{Bmatrix} p_+ & p_- \\ p_- & p_+ \end{Bmatrix} \begin{Bmatrix} h_{(n+1)u} \\ g_{(n+1)u} \end{Bmatrix}$$

$$= M_{n,n+1} \begin{Bmatrix} h_{(n+1)u} \\ g_{(n+1)u} \end{Bmatrix} \qquad (8\text{-}7)$$

where

$$p_\pm = 1/2[1 \pm (\epsilon_n k_{(n+1)z} / \epsilon_{(n+1)} k_{nz})] \qquad (8\text{-}8)$$

and in equation (8-8) $\epsilon_3 = \epsilon_{xx}$

The amplitudes in the prism are now related to the downward amplitude in the prism by

$$\begin{Bmatrix} h_{o1} \\ g_{o1} \end{Bmatrix} = M_{o1} \prod_{i=1}^{4} F_i M_{i,i+1} \begin{Bmatrix} h_{5u} \\ 0 \end{Bmatrix} \qquad (8\text{-}9)$$

where $g_{5u} = 0$ since the condition of the experiment is that

there is no upward travelling wave in the substrate. Equation (8-9) could be written as :

$$\begin{bmatrix} h_{ol} \\ g_{ol} \end{bmatrix} = \begin{bmatrix} r_{11} & r_{12} \\ r_{21} & r_{22} \end{bmatrix} \begin{bmatrix} h_{5u} \\ 0 \end{bmatrix} \qquad (8\text{-}10)$$

and the ATR intensity reflection coefficient is:

$$R = | r_{21} / r_{11} |^2 \qquad (8\text{-}11)$$

The theoretical ATR spectrum for this sample in P-polarisation, using equation (8-11), is shown in fig (8.3). The dips labelled S_1 to S_4 identify the surface- mode features. The dip marked G_1 is the excitation of a bulk polariton.

The measured far infrared ATR spectrum obtained by averaging 100 scans using a diamond-window Golay cell detector is shown in figure (8.4). These measurements were made at a resolution of 4 cm^{-1}. It can be seen from figure (8.4) that this low resolution is not enough to resolve all the surface mode features. Also we cannot see the guided mode dip (bulk polaritons).

Changing the detector to a liquid He cooled Ge bolometer which is a fast detector with signal to noise ratio forty times better than the Golay cell detector, an average of

two hundred ATR scans (resolution 1 cm^{-1}) of the MQW sample together with the background spectrum of the interferometer is shown in figure (8.5). This shows that all the surface mode features are clearly resolved, and that the features are present in the ATR specimen scan and not in the background scan.

The two figures (8.4 and 8.5) give a good indication of the reproducibility of the measured spectrum with the two different detectors.

Figure (8.6) shows three sets of fifty ATR scans of the specimen which clearly shows the reproducibility of the all measured features.

A number of runs are co-added until an acceptable signal to noise ratio has been achieved. Figure (8.7) shows the measured ATR spectrum for P-polarisation with acceptable signal to noise ratio. All the four surface feature dips, simultaneously with the guided mode dip (bulk polariton) are clearly identified and have been labelled in the figure. The oscillatory structures in the regions 320-360 cm^{-1} and 220-250 cm^{-1} are due to signatures from the diamond window of the Golay cell detector. These structures could not be completely eliminated by ratioing the specimen spectra and the background spectra for the interferometer. The two figures (8.3 and 8.7) show the good qualitative agreement between the theoretical and the measured ATR spectra for P-polarisation.

A theoretical ATR spectrum for S-polarisation when the angle of incidence is 20^{o} and the air-gap is of the order of 10 μm is shown in figure (8.8). The dip of about 295 cm^{-1} is due to bulk-polariton modes and not a surface mode (Borstel and Flage 1977). The measured ATR spectrum for this polarisation direction is shown in figure (8.9). Although there is general agreement between the two ATR spectra, there are some discrepancies:

1- The position of the dip is around 300 cm^{-1} in the measured ATR spectrum.

2- The experimental curve has a lower reflection coefficient throughout most of the frequency range.

3- There is a weak minimum in the measured curve near 280 cm^{-1} which could arise from the strong doublet due to surface polaritons and it is observed here because the wire grid polariser used for these measurements is less than 100% efficient at this frequency.

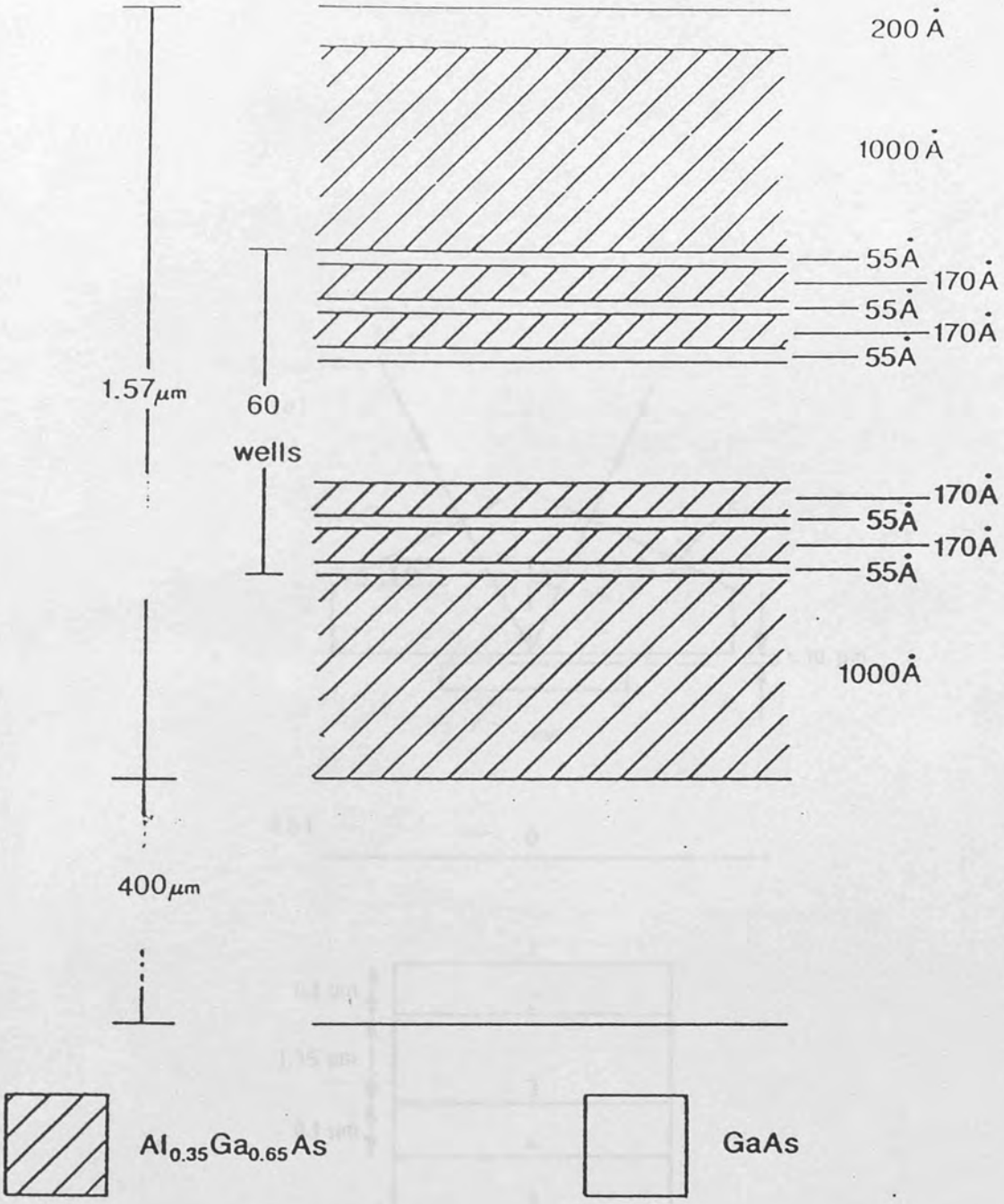

Fig (8.1): Schematic diagram of the MQW sample consisting of 60 layers of AlGaAs and GaAs, with AlGaAs cladding and a GaAs protection layer. This is deposited on a GaAs substrate.

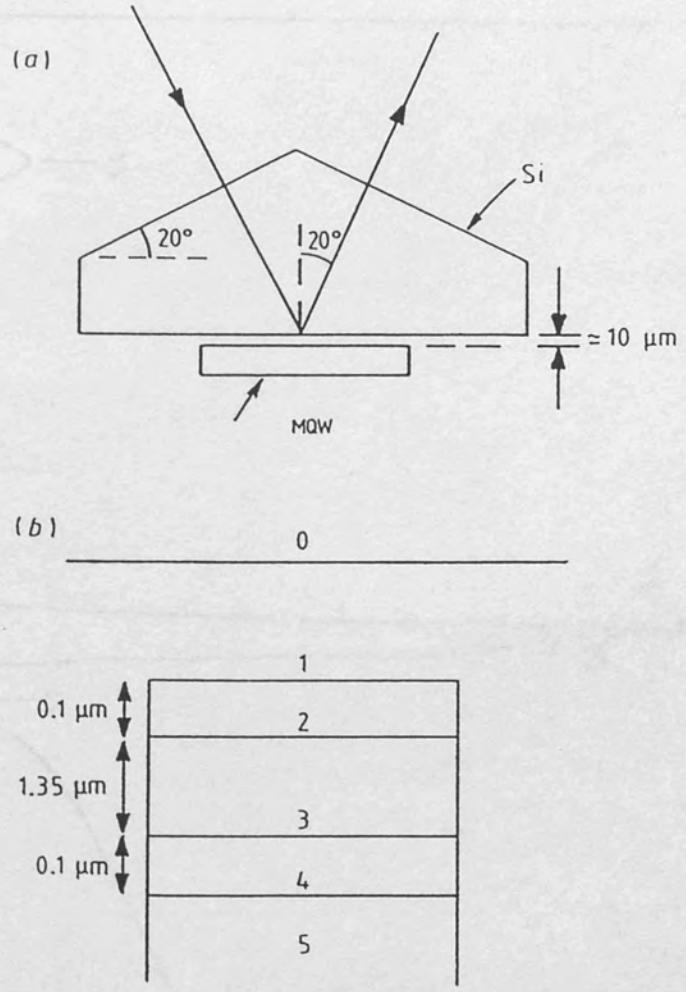

Fig (8.2): Schematic diagram of the geometry of the Si ATR prism and MQW sample

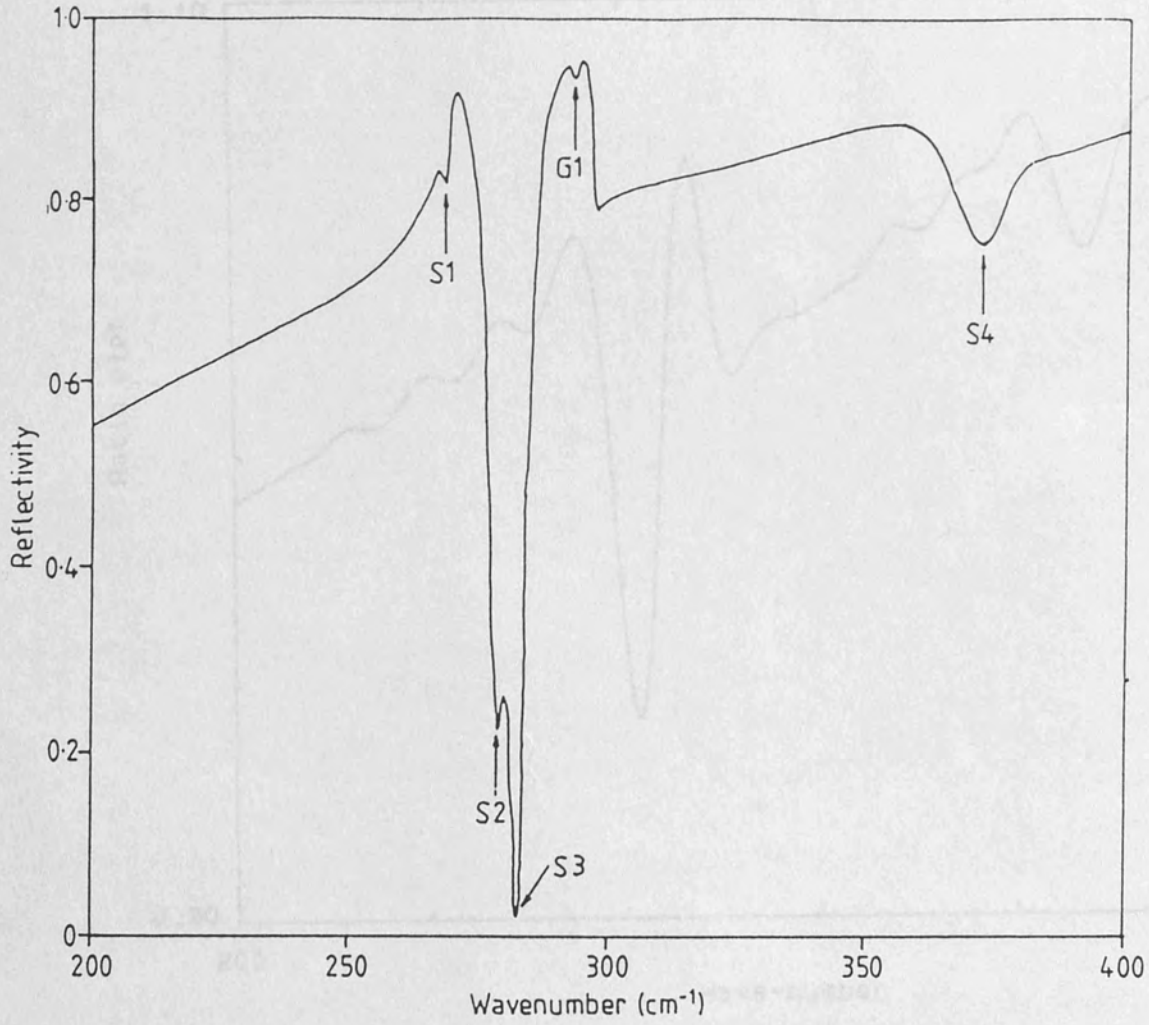

Fig (8.3): Theoretical ATR spectrum with p-polarised incident radiation for the MQW sample

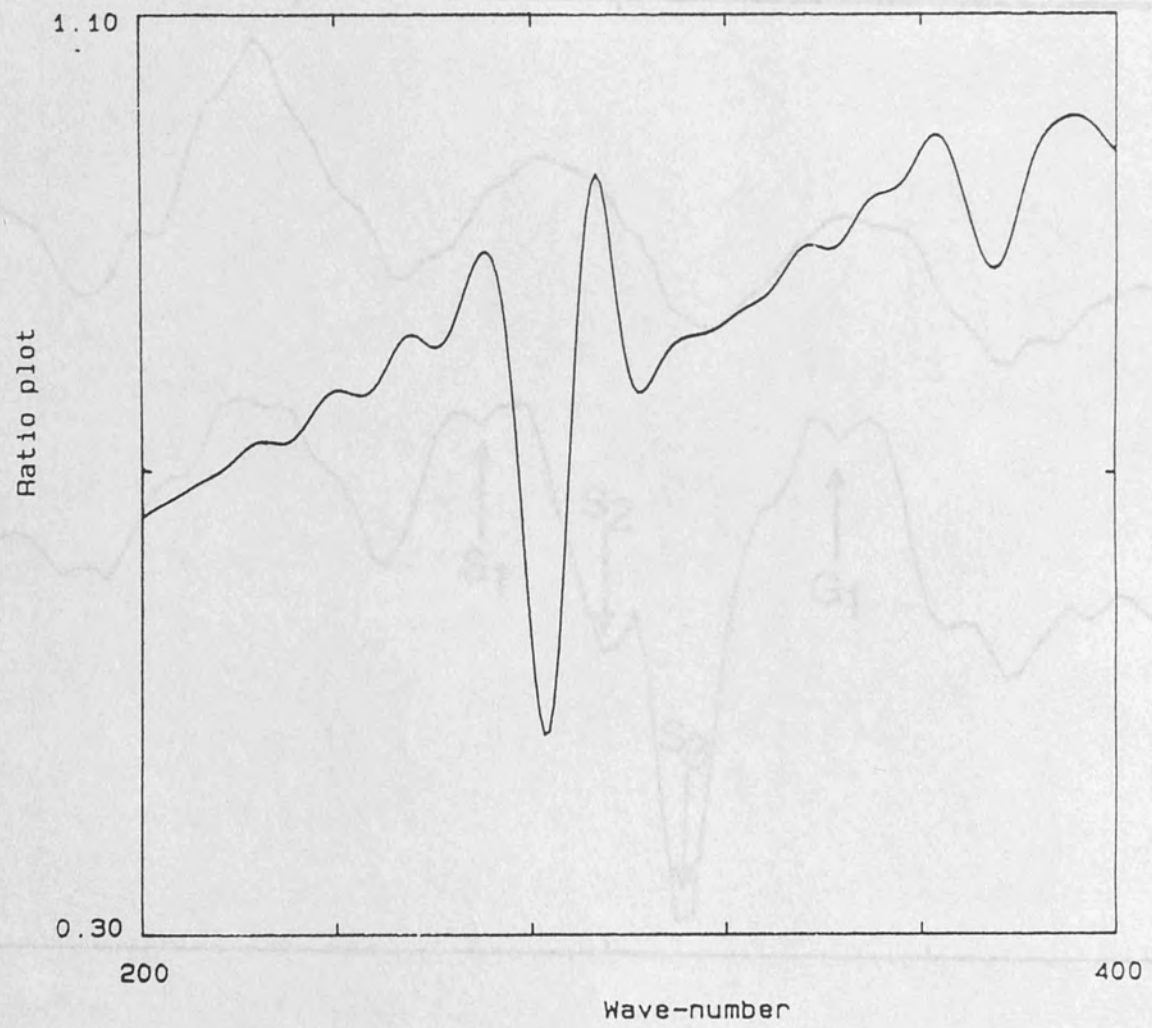

Fig (8.4): The measured ATR spectrum with p-polarised incident radiation for the MQW sample using a Golay detector

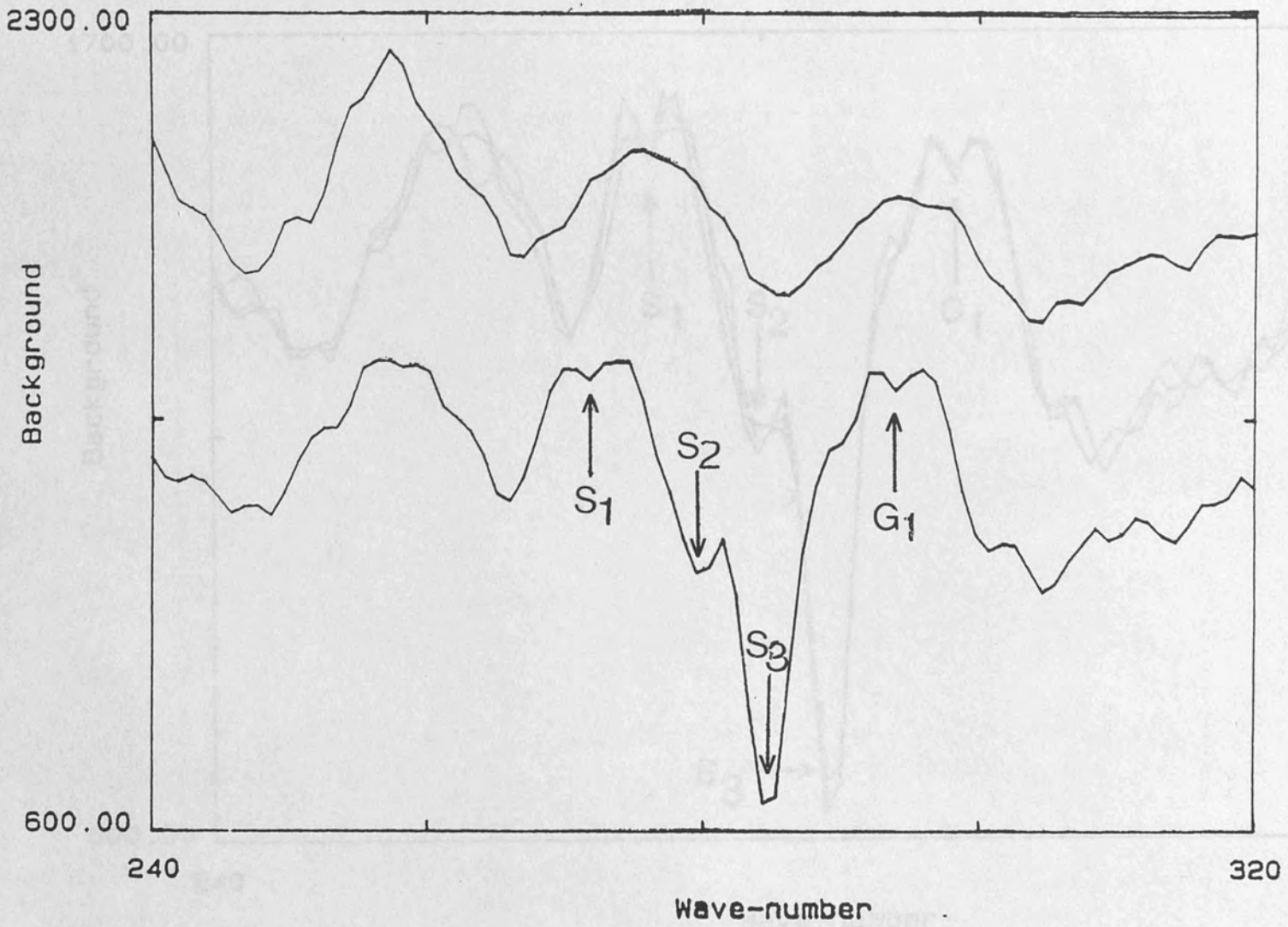

Fig (8.5): Fourier transform of background and MQW ATR interferogram

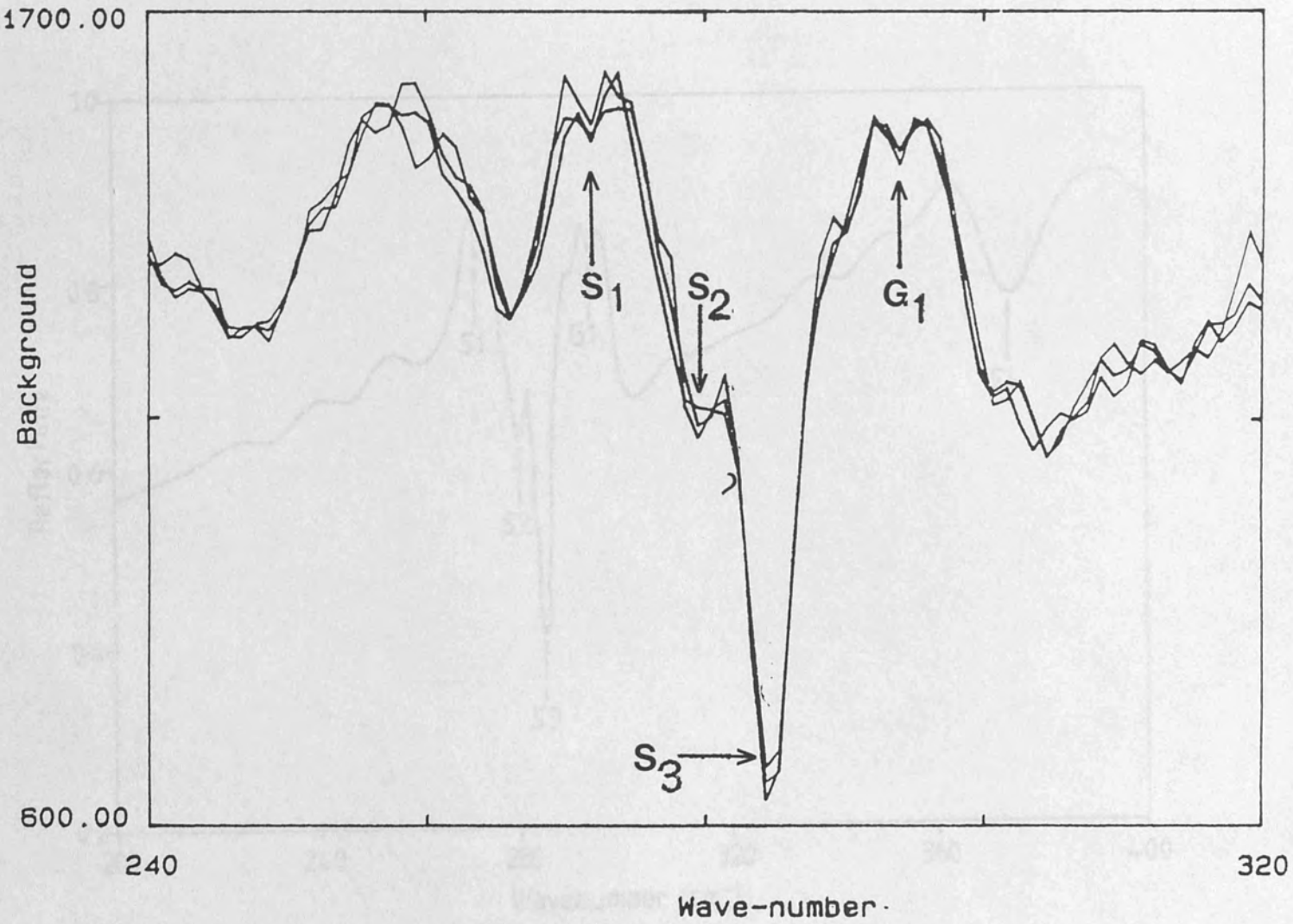

Fig (8.6): Fourier transform of three sets of fifty ATR scans of the MQW specimen

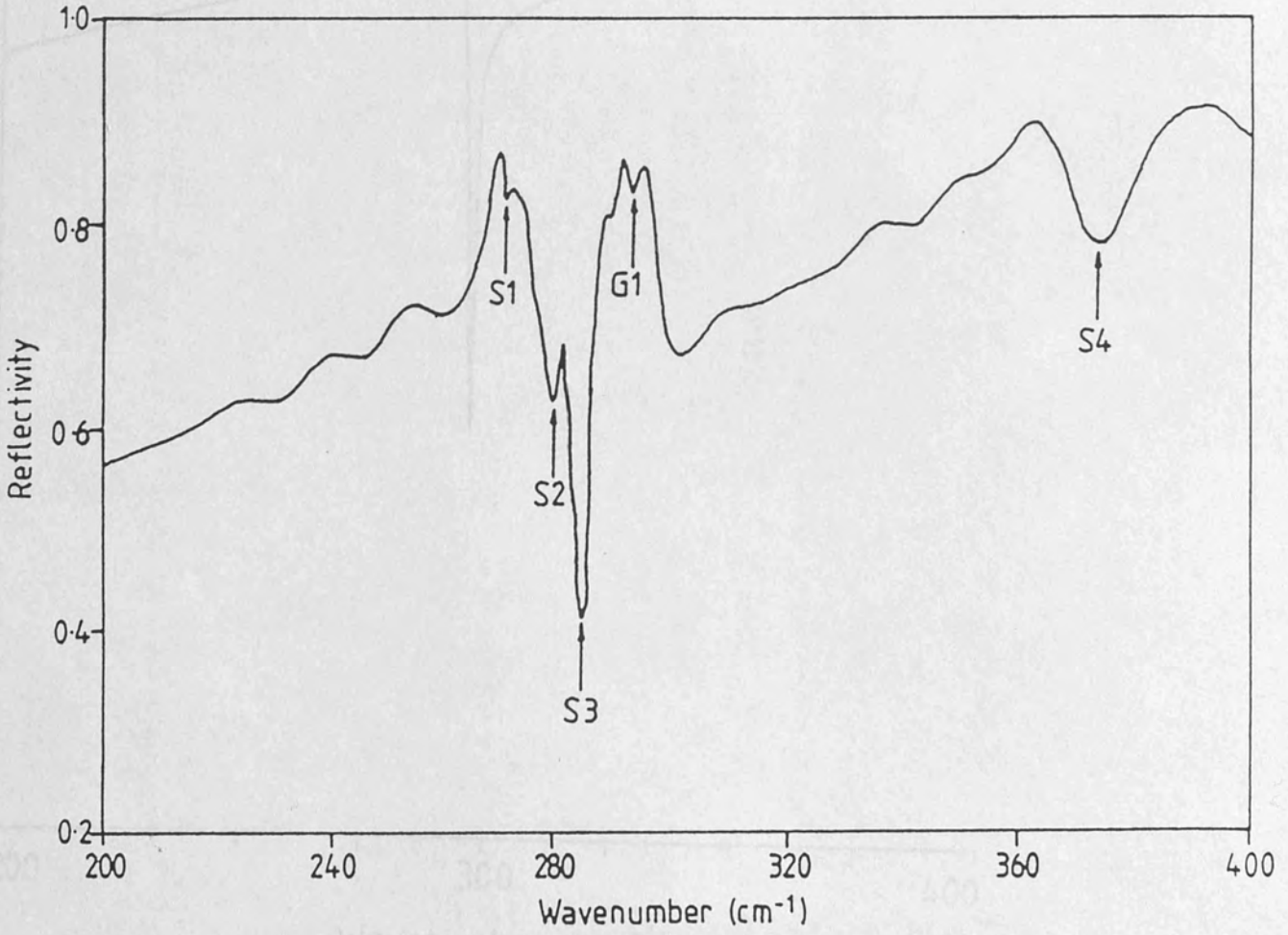

Fig (8.7): The measured ATR spectrum for p-polarised incident radiation with acceptable signal to noise ratio

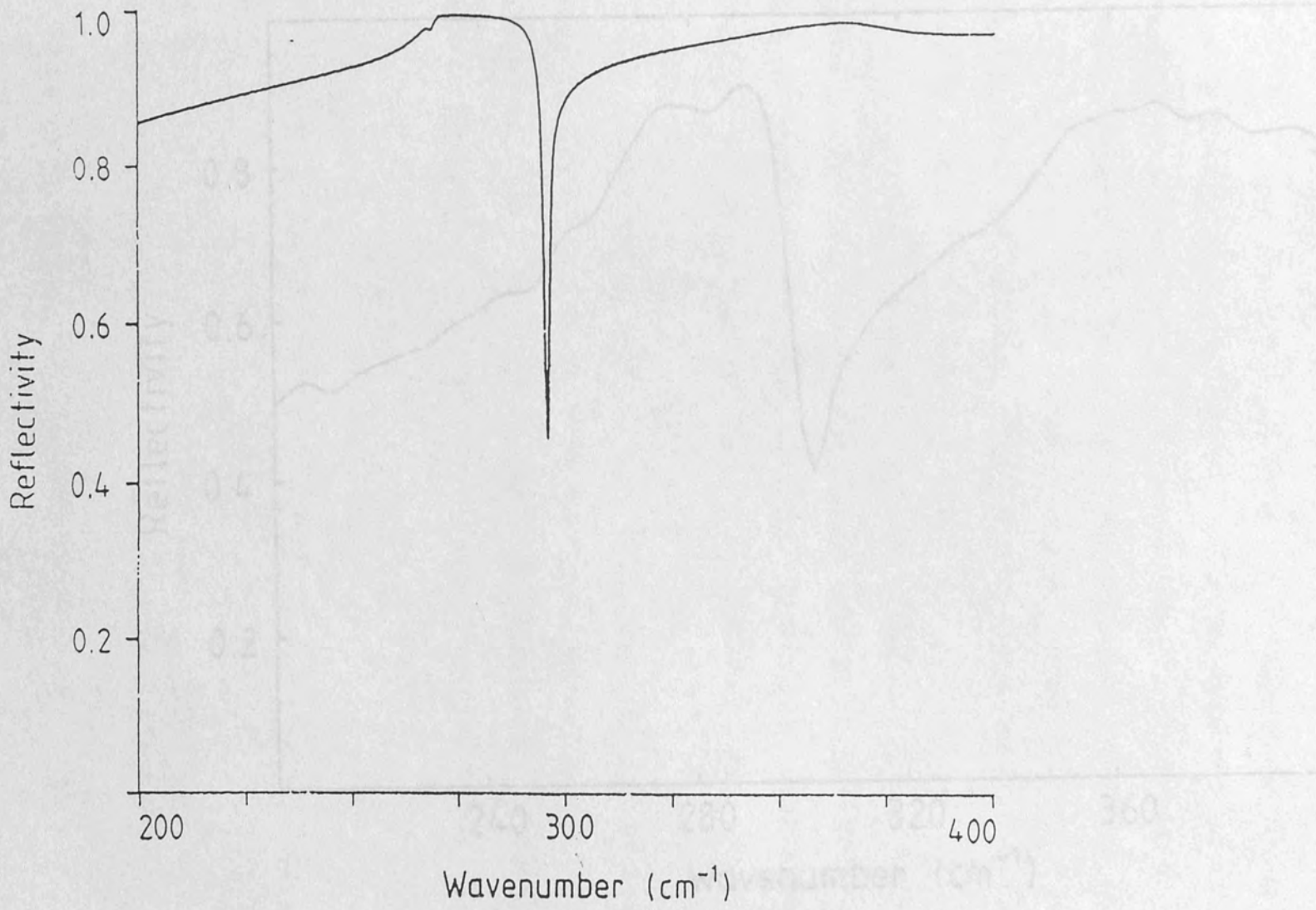

Fig (8.8): Theoretical ATR spectrum with s-polarised incident radiation for the MQW specimen

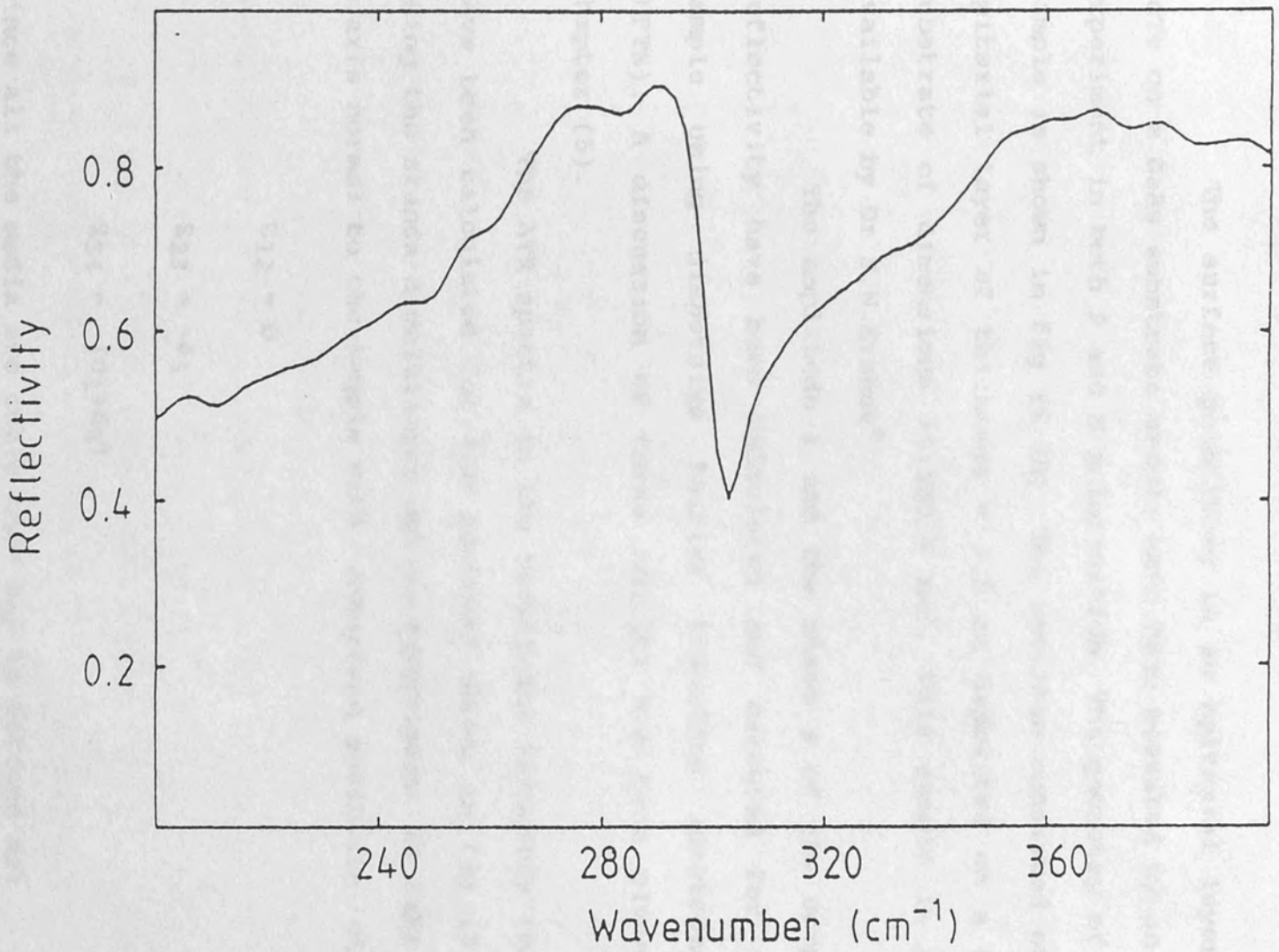

Fig (8.9): The measured ATR spectrum for s-polarised incident radiation for the MQW specimen

8-3 ATR MEASUREMENTS FOR CdTe ON A GaAs SUBSTRATE :

The surface polaritons in an epitaxial layer of CdTe on a GaAs substrate sample have been measured by an ATR experiment in both P and S polarisation. The geometry of the sample is shown in fig (8.10). The specimen consisted of an epitaxial layer of thickness $\simeq$ 3.5 μm deposited on a GaAs substrate of dimensions 15x5x0.5 mm^3. This sample is made available by Dr S.N.Ershov*.

The amplitude r and the phase ϕ of the complex reflectivity have been calculated and measured for this sample using dispersive Fourier transform spectrometry (DFTS). A discussion of these results has been given in chapter (5).

The ATR spectra in the reststrahl frequency region have been calculated for the geometry shown in fig (8.10) using the standard multilayer optics techniques. We take the Z axis normal to the sample with interface positions at;

$$z_{12} = 0$$

$$z_{23} = -d_1$$

$$z_{34} = -(d_1+d_2)$$

Since all the media are cubic then k_{nz} is defined as:

* Faculty of Physics, Gorky State University, USSR

$$k_{nz} = [\epsilon_n (\omega^2/c^2) - k_x^2]^{1/2}$$

$$n = 1,2,3,4$$

Following the procedure which we used to calculate the ATR spectra for the MQW sample, we obtain the following results

$$\begin{bmatrix} h_{11} \\ g_{11} \end{bmatrix} = M_{12} F_2 M_{23} F_3 M_{34} \begin{bmatrix} 1 \\ 0 \end{bmatrix}$$

$$\begin{bmatrix} h_{11} \\ g_{11} \end{bmatrix} = \begin{bmatrix} r_{11} & r12 \\ r_{21} & r_{22} \end{bmatrix} \begin{bmatrix} 1 \\ 0 \end{bmatrix}$$

$$R = | r_{21} / r_{11} |^2$$

The theoretical ATR spectrum for this sample in P-polarisation when the angle of incidence is 20° and the air-gap is 15 μm, is shown in fig (8.11).

Using a diamond-window Golay cell detector, a spectrum obtained by averaging 100 scans is shown in fig (8.12). We used a resolution of 4 cm^{-1} which is available with a Golay cell as discussed before. Surface phonon polaritons are observed as expected in the CdTe reststrahlen band.

The two figures (8.11 and 8.12) show the good qualitative agreement between the measured and the

theoretical ATR spectra for P-polarisation. The fringes observed in the measured spectra below the reststrahlen band of CdTe arise from interference between the beams reflected from the top of the specimen and the base of the substrate. At higher frequencies the second beam is heavily attenuated and the fringes are not observed. Similar fringes are not present in the calculated spectra, in which a semi-infinite substrate has been assumed.

For S polarisation the calculated ATR spectrum is shown in figure (8.13). A sharp guided wave mode is observed around 285 cm^{-1}. Using a diamond-window Golay cell detector, an ATR spectrum of 200 scans is shown in figure (8.14). It can be seen from the two figures (8.13 and 8.14) that the overall agreement between theory and experiment is generally quite good. However, the oscillatory structures in the experimental spectrum are due to signatures from the diamond window of the Golay cell detector. These signatures could not be completely eliminated by ratioing the specimen and the background spectra. Also, the polariser is not 100% efficient, and this leads to weak cross-talk between the p and s polarised spectra.

8-4 REFERENCES:

V M Agranovich and D L Mills "Surface Polaritons" (Amsterdam: North-Holland), 1982.

A D Boardman, "Electromagnetic Surface Modes", (Chichester: Wiley), (1982).

G Borstel and H J Falge, Phys. Status Solidi b 83, 11, (1977).

K A Maslin, T J Parker,N Raj, D R Tilley, P J Dobson, D Hilton and C T R Foxon, Solid State Commun., 60, 461 (1986).

A Otto Festkorperprobleme (Advances in Solid State Phys) vol. XIV, ed J Treush (Braunschweig: Vieweg), 1974.

N Raj and D R Tilley, Phys. Rev. B 36, 7003 (1987).

N Raj, R E Camley and D R Tilley, J. Phys. Solid State Phys. 20, 5203 (1987).

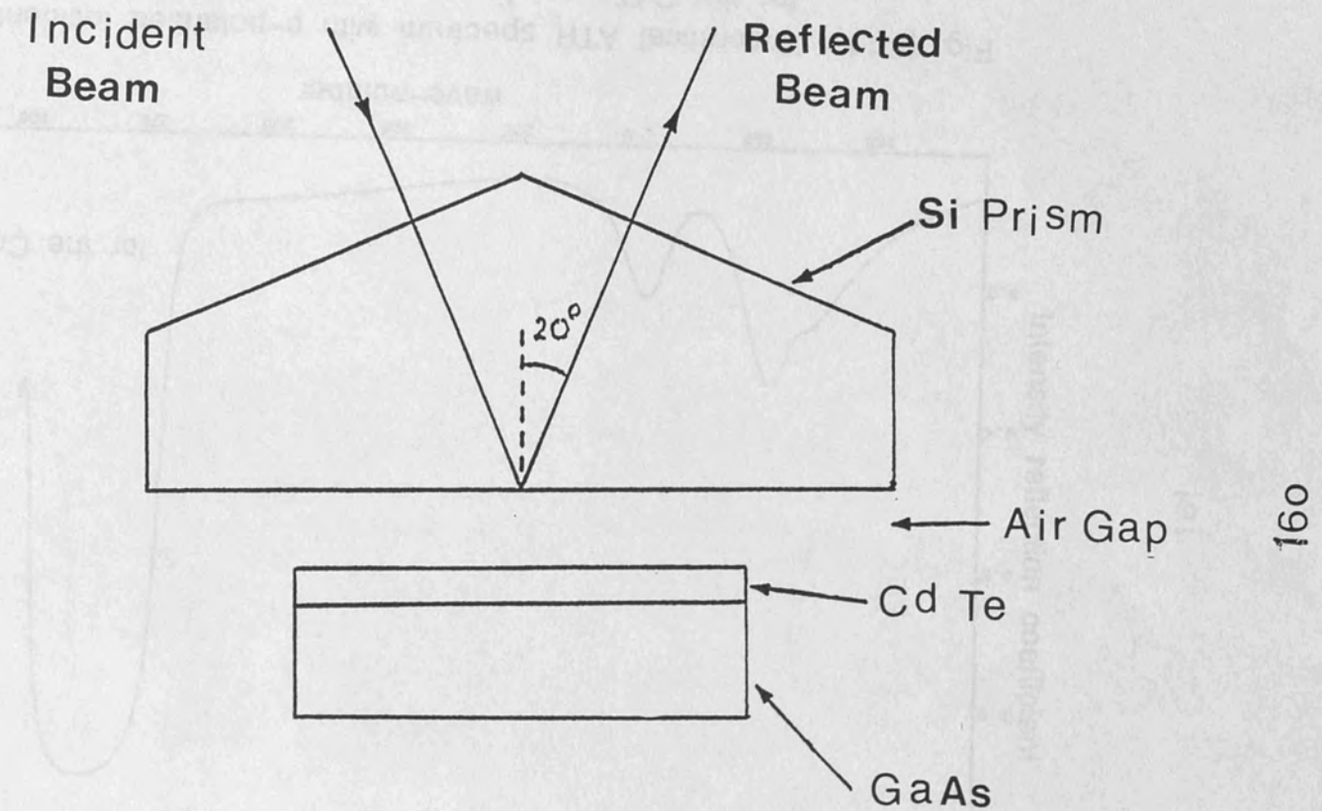

Fig (8.10): Schematic diagram showing the geometry of the CdTe epi-layer sample

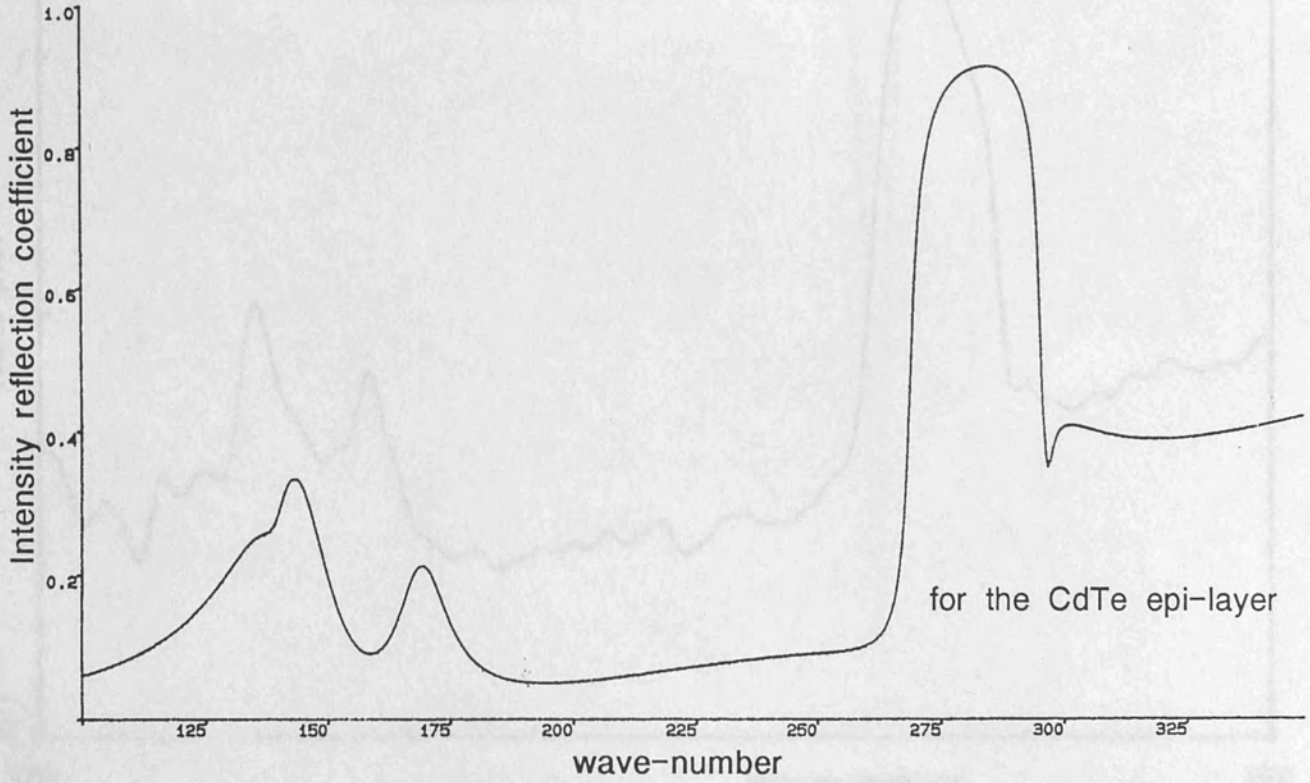

Fig. (8.11): Theoretical ATR spectrum with p-polarised incident radiation for the CdTe epi-layer sample

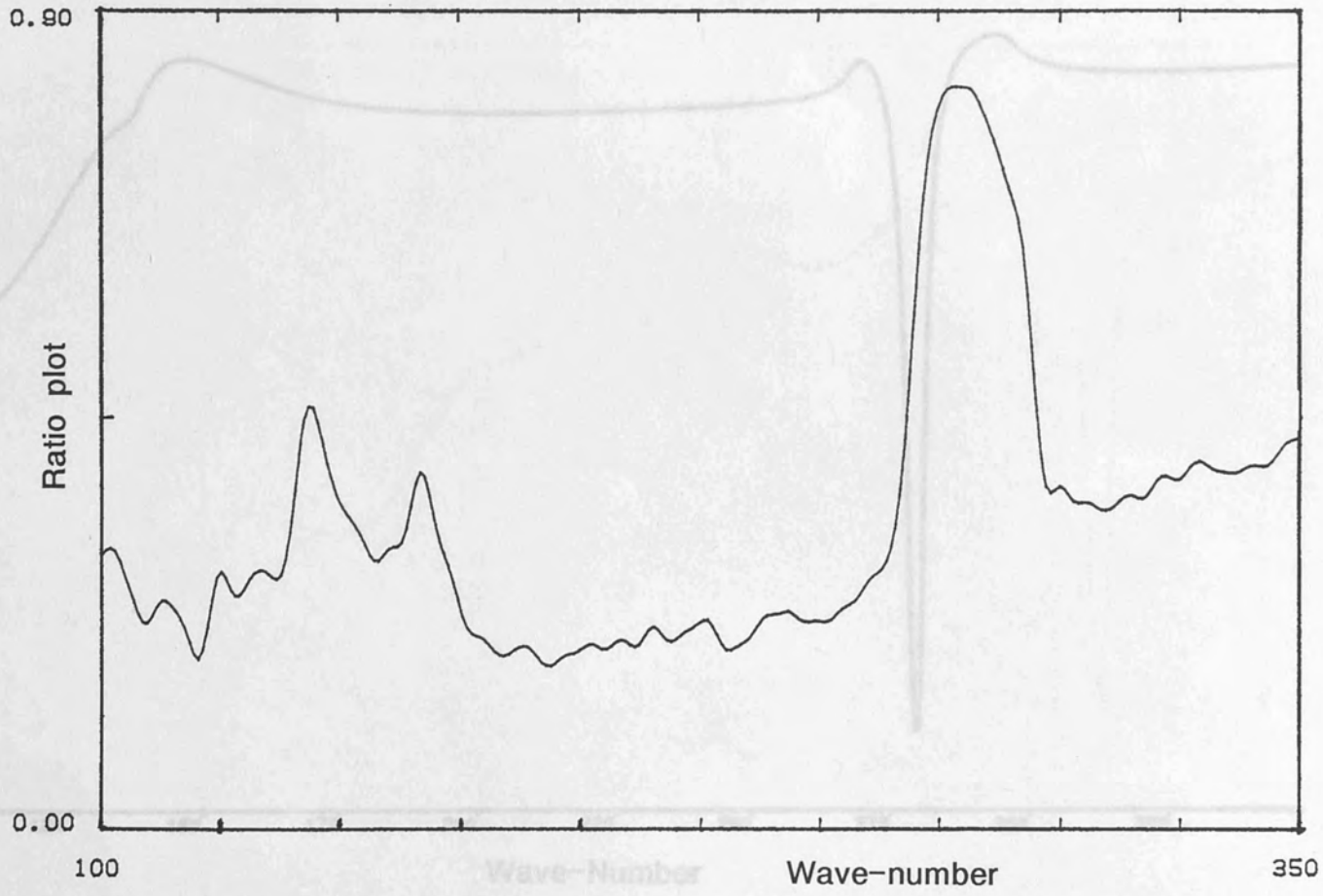

Fig. (8.12): The measured ATR spectrum with p-polarised incident radiation for the CdTe epi-layer sample

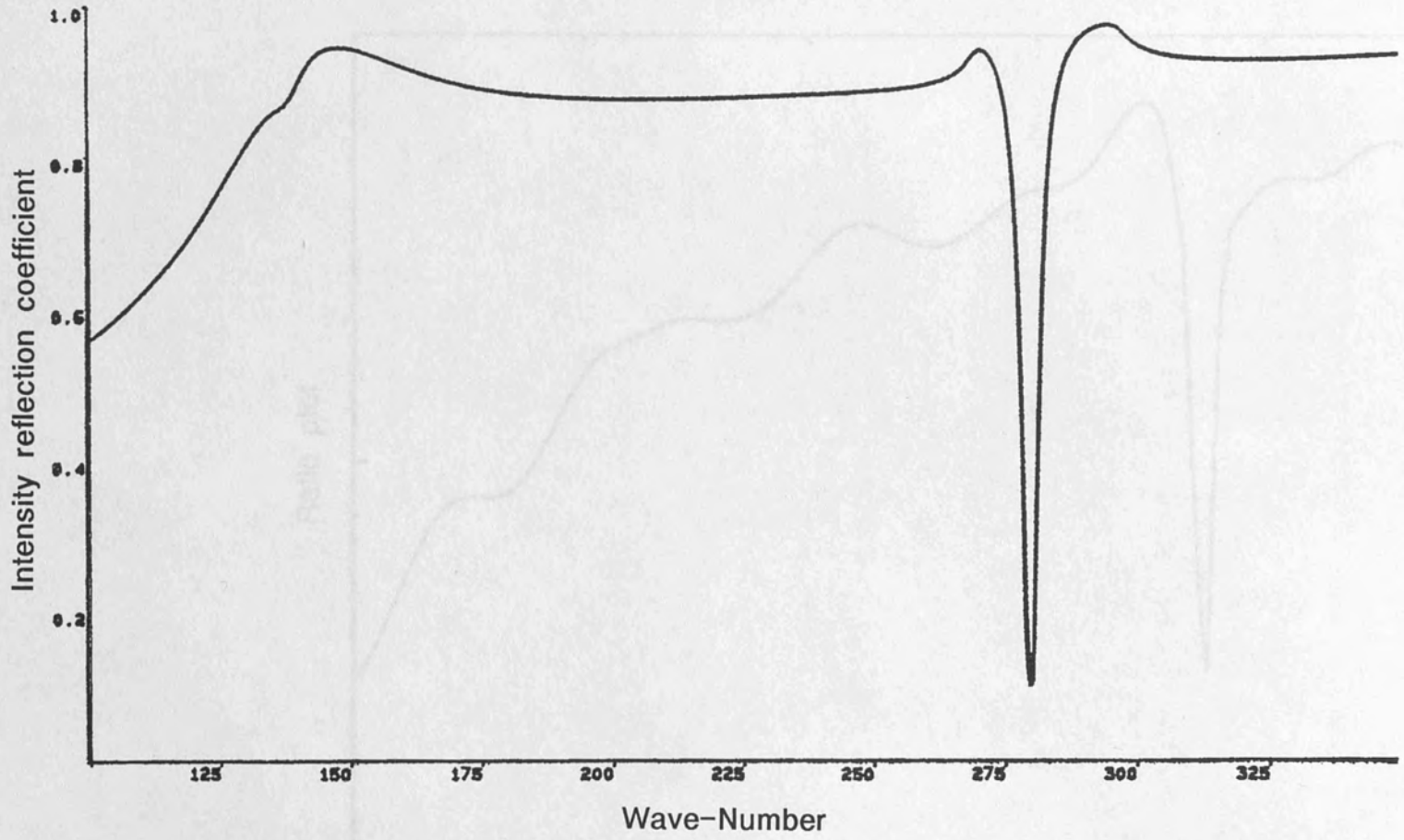

Fig. (8.13): Theoretical ATR spectrum with s-polarised incident radiation for the CdTe epi-layer sample

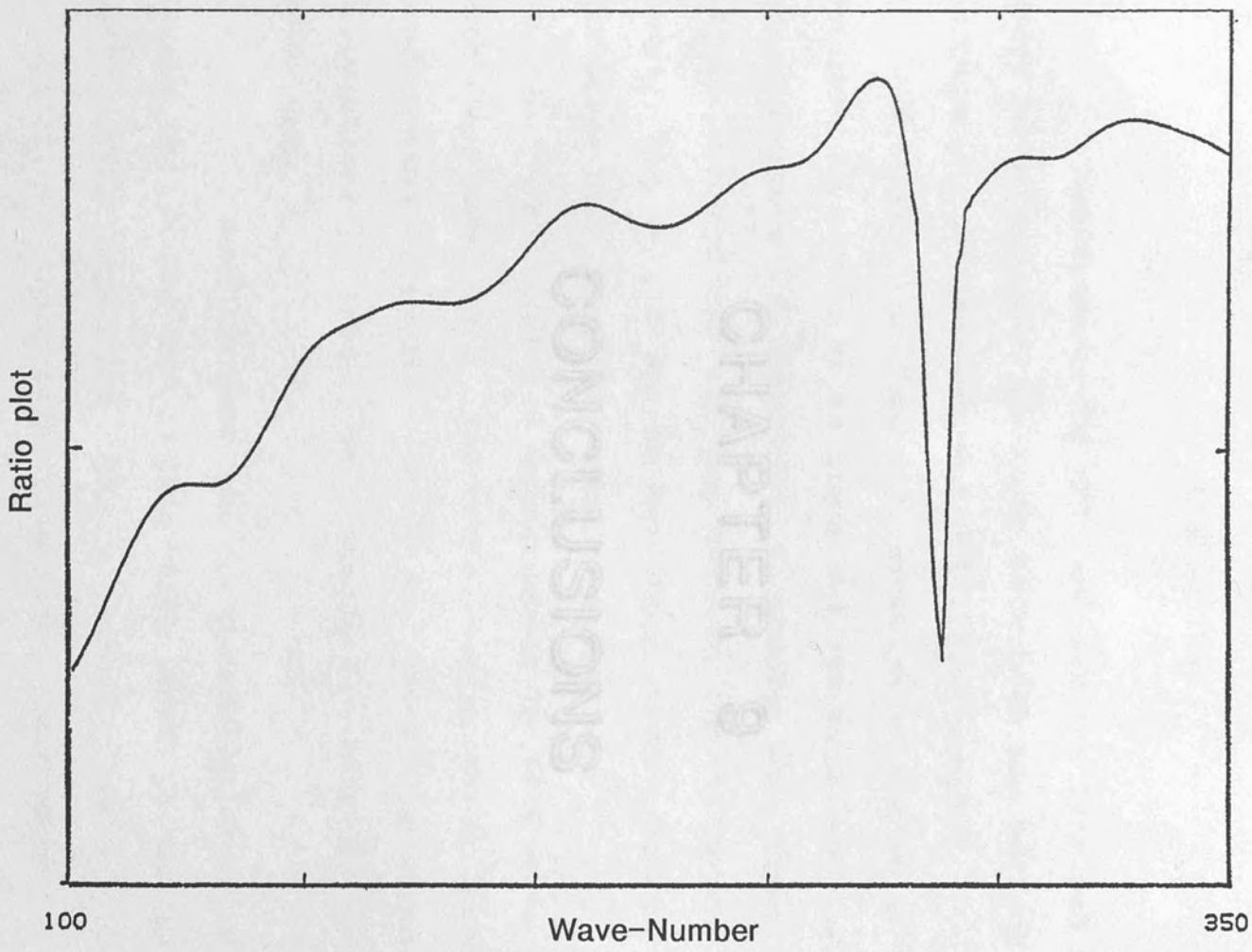

Fig. (8.14): The measured ATR spectrum with s-polarised incident radiation for the CdTe epi-layer sample

CHAPTER 9

CONCLUSIONS

CHAPTER (9)

CONCLUSIONS

Measurements by DFTS and ATR far infrared spectroscopy have been made to study both bulk and surface phonons propagating in semiconductor multilayer samples.

Using the Otto configuration an ATR stage has been designed to enable us to study surface polaritons in layered semiconductors. A sensitive micrometer has been used to adjust the optimum air gap between the Si prism and the sample. New output optics have been constructed to fit the ATR stage of a power FTS interferometer.

Far infrared measurements by DFTS have revealed both epi-layer and substrate reststrahlen bands. The experimental results are in good agreement with calculations based on standard multilayer optics techniques.

Results from the 11 parameter rigid ion model developed by Ren et al has been used to calculate the reflectivity spectrum of a short period GaAs/AlAs superlattice. This shows reasonable agreement with DFTS measurements. However the theoretical model needs more work to give explicit results. A bulk plasmon arising from the doped substrate was also observd in this sample.

In this work the observation of surface phonon

polaritons on a long period GaAs/$Al_xGa_{1-x}As$ multiple quantum well (MQW) has been reported for the first time. The measurements were made in both p- and s_polarisations. The experimental results are compared with the theoretical spectra derived by treating the MQW as an effective uniaxial dielectric bulk medium. The experimental and theoretical results are in excellent agreement both qualitatively and quantitatively. Four surface mode dips and one guided wave dip are observed in p-polarisation at frequencies which are in good agreement with theory and, as expected, no surface mode features are observed for s-polarisation.

ATR measurements were also made on a semiconductor sample consisting of an epitaxial layer of CdTe on GaAs substrate. The measurements have revealed a p-polarised surface polariton in the CdTe reststrahlen band as predicted by the theoretical calculations.

In this work we have shown how a combination of DFTS and ATR far infrared spectroscopy may be used to give very detailed information about bulk and surface phonon and guided waves propagating in a semiconductor epi-layer system.

In long period superlattice (MQW) the optical properties are satisfactorily described by the bulk slab model, in which each layer is assumed to have the dielectric function of the corresponding bulk material. A simple effictive medium aproximation to this model, describing the

superlattice as a single uniaxial medium, gives a good account of far infrared reflectivity and atr spectra.

This work has established the applicability of ATR spectroscopy to multilayer specimens. It has been suggested that ATR could be used to observe surface plasmon polaritons on superlattices, and we believe that such measurements could be carried out by the method described here.

publications

Publications based on the work described in this thesis:

A R El Gohary, T J Parker, N Raj, D R Tilley, P J Dobson, D Hilton and C T B Foxon.
"Observation of surface phonon-polaritons on a MQW specimen by attenuated total reflection spectroscopy."
Semicond. Sci. and Technol. , 4, 388, 1989

T Dumelow, A R El Gohary, K A Maslin, T J Parker, D R Tilley and S N Ershov.
"Bulk and surface phonon-polaritons and guided waves on an epitaxial layer of CdTe deposited by plasma MOCVD on a GaAs substrates ".
Semicond. Sci. and Technol. , in press (1989.)

T Dumelow, A R El Gohary, A Hamilton, K A maslin, T J Parker, N Raj, B Samson, S R P Smith, D R Tilley, P J Dobson, D Hilton, K Moore and C T B Foxon.
"Study of bulk and surface phonons and plasmons in GaAs/AlAs superlattices by far infrared and Raman spectroscopy".
J. Mat. Sci. and Eng. Section B: solid state Mats. for Adv. Tech. in press (1989.)

T Dumelow, A R El Gohary, K A Maslin, T J Parker, D R Tilley and S N Ershov.
"Far infrared spectroscopy of bulk and surface phonon polaritons on epitaxial layers of CdTe deposited by plasma MOCVD on GaAs substrates".
J. Mat. Sci. and Eng. Section B: solid state Mats. for Adv. Tech. in press (1989.).